A unified theoretical modeling framework for soft and hard magnetorheological elastomers

Kostas Danas

A unified theoretical modeling framework for soft and hard magnetorheological elastomers

K. Danas[a]

[a] *LMS, C.N.R.S., École Polytechnique, Institut Polytechnique de Paris, 91128 Palaiseau, France*

Abstract

These notes put together a number of theoretical and numerical models and results obtained for magnetically soft and hard magnetorheological elastomers, denoted as s-MREs and h-MREs, respectively over the last five years in our group. We present in a unified manner both s- and h-MREs. In particular, we regard MREs, in the general case, as magnetically dissipative nonlinear elastic composite materials comprising a mechanically-soft, non-magnetic elastomeric matrix in which mechanically-rigid, magnetically-dissipative particles are embedded isotropically and randomly. The proposed incremental variational frameworks are general enough to deal with more complex microstructures such as particle-chains or others that do not yet exist in the lab. More importantly, we propose homogenization-guided, analytical, explicit models that are consistent as one moves from the dissipative h-MREs to the purely energetic s-MREs. In parallel, we propose numerical frameworks allowing to simulate a very wide variety of microstructures and boundary value problems in magneto-mechanics.

Contents

Email address: konstantinos.danas@polytechnique.edu (K. Danas)

Published in CISM International Centre for Mechanical Sciences book series, vol. 610, 2024, (DOI)

1. Introduction

By now a large body of research exists in the literature on magneto-active solids. There are mainly two classes of magneto-active solids:

(i) mechanically-stiff magnetic materials made of permanents *hard* magnets (e.g., NdFeB in polycrystal or powder form embedded in a stiff polymer or at very large volume fractions) exhibiting significant magnetic dissipation or magnetically *soft* ferromagnets (e.g., Fe and compounds of it) with negligible magnetic dissipation.

(ii) mechanically-soft polymer-based composite materials (e.g. with shear modulus less than 1 MPa) comprising the former magnetic metals in powder or micron-sized particle form.

The main difference between those two classes of magneto-active materials is the ability of the latter soft polymeric ones to deform substantially under the application of a magnetic field. Usually in the first class of mechanically-stiff magneto-active solids, one may reach *magnetostrictive* strains ranging from a few to several thousands ppm (i.e., in the order of $10^{-6} - 10^{-3}$). By contrast, use of magneto-active polymers also known as "magnetorheological elastomers" or MREs[1] allows to obtain fairly large effective magnetostrictive strains even as large as $0.4 - 0.5$ (depending on the compliance of the polymer), which is several orders of magnitude larger than those of metals or stiff polymers.

In turn, the first class of magnetic materials exhibits superior magnetic properties (such as initial magnetic permeability or susceptibility, magnetic saturation, magnetic coercivity and so on) as compared to the corresponding soft polymer composites. The reason for this is fairly simple and is related to the actual quantity of particles that can be embedded in the polymer retaining at the same time its soft mechanical properties. In practice, most of mechanically-soft MREs contain volume fractions of magnetizable particles ranging between 0-30vol%. Any further addition of rigid particles in the polymer leads rapidly to significant material stiffening and thus to loss of its interesting magnetostrictive capabilities.

The deformation mechanisms in those two classes of materials are entirely different and require in general very different modeling approaches. While one can write down the same general concepts and equations relating magnetics with mechanics, the details required to describe adequately these two classes of materials are extremely different. The metallic materials deform under the application of an externally applied magnetic field due to a complex motion, interaction, nucleation, annihilation and reconfiguration of magnetic walls lying at the nanometer scale. Several nano-, micro- and macroscopic theories have been proposed to describe those deformation mechanisms over the last fifty years and will not be discussed in the present notes. In turn, MREs, which is the main topic of the present note, deform due to rearrangement and (static/dynamic) reconfiguration of the magnetic particles, which carry along with them the surrounding non-magnetic soft polymer matrix. In this sense, the word *magnetostriction* in MREs serves to describe this collective particle rearrangement leading to an effective (or average) deformation of the composite polymer. Evidently, the magnetic particles themselves also deform due to magnetic domain wall motions at

[1] In the literature, one may find a number of equivalent names such as MAEs (magneto-active elastomers), MAPs (magneto-active polymers), MREs (magnetorheological elastomers), MSEs (magneto-sensitive elastomers) and many others. The word MREs was the first one, perhaps because these materials were first synthesized by material scientists (Jolly et al., 1996; Ginder et al., 1999) that worked before on magnetorheological fluids, a close cousin to the present mechanically-soft MREs.

the lower nanometer scale. Nonetheless, those strains are orders of magnitude smaller than those occurring at the larger scale of the polymer composite (several tens of microns all the way up to millimeter scale) and thus are usually neglected to simplify the overall analysis.

While the above discussion focused on the material response, recent works, in the last decade, have used and synthesized MREs in simple or more complex macroscopic shapes, such as beams, films, spheres, cylinders, ellipsoids, trusses or even more fancier shapes mainly with the advent of 3D-printing capabilities. The literature is too vast to include in this introductory section, but interested readers may refer to numerous reviews on the subject in the literature (see for instance Bastola and Hossain (2020) and Lucarini et al. (2022b)). Precisely, this manufacturing capability to obtain complex geometrical, structural shapes made from MREs has led to their rapid development and more recent use in high end biomedical and sensing applications. By contrast, the original metallic magnetic materials are extremely difficult to shape (especially NdFeB or cobalt) since they are very brittle and thus their use is constrained to larger devices or engines (such as electric motors) where complex shaping is not needed at least up to now.

Having made this distinction, it is worth mentioning that in the literature, it is usually common to mix the notions of a material and a structure into the combined word of *meta-material*. Even so, whether those polymer composites are fabricated using magnetically soft particles, denoted henceforth as s-MREs, or magnetically hard particles, denoted as h-MREs, they exhibit extremely interesting coupled magneto-mechanical properties both at the material and structural level and for that reason they are still under extensive investigation.

In these notes, we focus on the modeling of MREs both at the material and the structural level. We present first the general finite strain theory on magnetically dissipative magneto-active solids and focus on the modeling of isotropic (quasi)-incompressible MREs. Subsequently, those material models are assessed by full three-dimensional representative volume element (RVE) finite element (FE) periodic simulations. A special augmented potential energy is developed for the results to be sensible. The developed models are based on homogenization theory and numerical data but also comprise phenomenological parts. This last choice is done in order to obtain simple, robust and above all explicit analytical material models for the MREs. These models may then be implemented in general purpose finite element codes (such as ABAQUS (2017) or FEniCS). Their simplicity allows to model complex two-dimensional and three-dimensional boundary value problems, including "meta-material" (or more correctly meta-structural) response of MRE-based structures, such as homogeneously or inhomogeneously magnetized beams or films.

2. Preliminary definitions in magneto-elasto-statics

In this section, we lay out some important definitions required for the development of general finite strain models for MREs. We state at this point that the subsequent presentation of the theory of MREs lies naturally at the domain of continuum mechanics and at scales that are that of the particles and larger. With this, we make clear that the goal of the following quantities and equations is to describe the response of MREs at a scale much larger (i.e., several micro-meters and above) than that of the so-called magnetic domain walls, which naturally occur at a scale of a few nano-meters. The reason for these approximations is two-fold. First, the main interest is to provide simple and explicit constitutive laws for composite MRE materials at the macroscale (i.e. millimeter and above) bringing from the lower scale the effect of magnetic particles embedded in a soft polymer matrix. Second, the nucleation and evolution of domain walls usually occurs rather fast and at the scale of the particles, which in turn strongly interact with each other. It is therefore

evident that it is extremely difficult (if not practically impossible) to resolve the domain-wall scale together with the particle interaction scale and at the same time recover a simple explicit model that can serve to analyze real boundary value problems (BVPs). For these reasons, we choose to describe the magnetic quantities in the particles in a rather continuum way, i.e., by assuming that pointwise (i.e. at $\mathbf{X}$) at each particle the magnetic quantities are described by continuum magnetic vector variables that follow simple constitutive laws (albeit nonlinear and dissipative ones) without however resorting to the resolution of the domain walls. It is noted that a gradient finite-strain variational phase-field framework following the early works of James and Kinderlehrer (1993) and DeSimone and James (2002) has been proposed recently by Keip and Sridhar (2018). In that work, the authors managed to resolve domain wall evolution at the level of the particles and then numerically resolve a small assembly of them in two-dimensions. They have shown qualitatively and quantitatively similar responses with those obtained by ignoring those domain walls and simply using local constitutive magnetic laws at the particle level. We thus follow the second option in the present note.

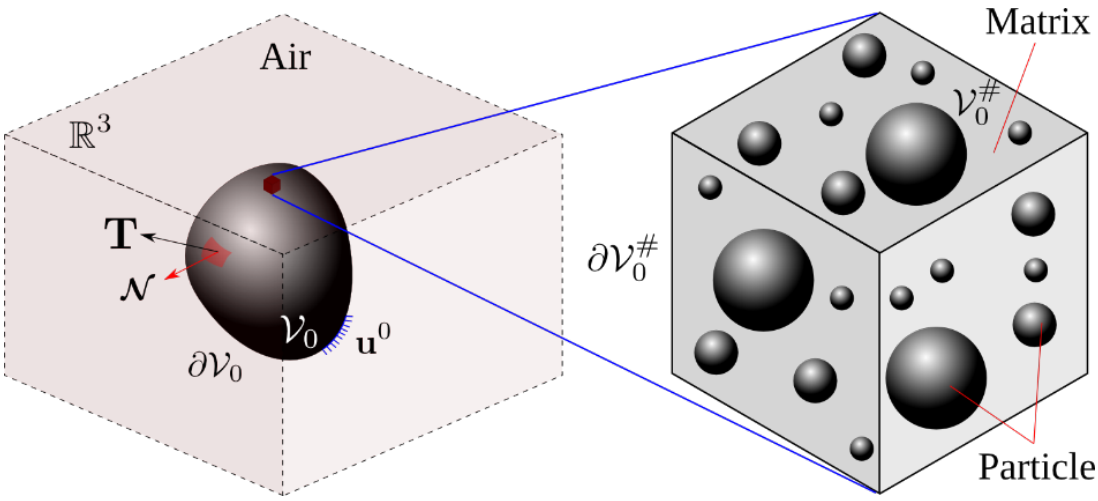

Figure 1: (Left) Typical sketch of the reference configuration of a magneto-active solid of volume $\mathcal{V}_0$ and boundary $\partial\mathcal{V}_0$ (usually in the order of several mm-cm) embedded in an air domain, occupying a volume $\mathbb{R}^3 \setminus \mathcal{V}_0$. (Right) Sketch of a representative material unit-cell comprising usually a non-magnetic polymer matrix phase and mechanically-stiff magnetizable particles with sizes ranging from $2 - 50\,\mu\text{m}$.

2.1. Finite strain kinematics

For simplicity, we consider at this stage a deformable, magneto-active solid with volume $\mathcal{V}_0$ ($\mathcal{V}$) in its reference (current) configuration that is embedded in $\mathbb{R}^3$. The domain $\mathbb{R}^3 \setminus \mathcal{V}_0$ is in general non-magnetizable and usually serves to denote the surrounding air (see Fig. 1). The magneto-active solid may not necessarily be a homogeneous body but could comprise several magnetic (e.g., particles) or non-magnetic phases (e.g. polymer matrix). For simplicity, at this introductory stage of the article, the reader could regard the body as homogeneous to avoid confusion for the various definitions.

The boundary of the solid is assumed to be smooth and is designated by $\partial\mathcal{V}_0$ ($\partial\mathcal{V}$), while $\boldsymbol{\mathcal{N}}$ ($\mathbf{n}$) denotes the unit normal on $\partial\mathcal{V}_0$ ($\partial\mathcal{V}$) in the reference (current) configuration (see Fig. 1). The

deformation of the solid from the reference to current configuration is defined to be a continuous, twice differentiable (except on the boundary/interfaces), one-to-one mapping $\mathbf{y}(\mathbf{X})$. Thus, the position of any point $\mathbf{X}$ in the reference configuration is given by $\mathbf{x} = \mathbf{y}(\mathbf{X})$ in the current configuration. In turn, the mechanical displacement field $\mathbf{u}(\mathbf{X})$ relates the current position vector to the reference so that $\mathbf{x} = \mathbf{X} + \mathbf{u}(\mathbf{X})$. The deformation gradient is then defined to be

$$\mathbf{F} = \mathrm{Grad}\,\mathbf{y}(\mathbf{X}) = \mathbf{I} + \mathrm{Grad}\,\mathbf{u}(\mathbf{X}), \qquad J = \det\mathbf{F} > 0, \tag{1}$$

where $\mathbf{I}$ is the second-order identity tensor, whereas $J > 0$ imposes the impenetrability condition, or simply positive volume condition. It is recalled that the $\mathrm{Grad} = \partial/\partial\mathbf{X}$ as well as that $\mathbf{F}$ is a compatible two-point tensor, i.e., satisfies $\mathrm{Curl}\mathbf{F} = \mathbf{0}$.

After introducing the conjugate quantity to the deformation $\mathbf{F}$, the first Piola-Kirchhoff stress $\mathbf{S}$, conservation and angular momentum lead to the pointwise equilibrium, symmetry and boundary conditions

$$\mathrm{Div}\ \mathbf{S} = \mathbf{0} \quad \text{in} \quad \mathbb{R}^3, \qquad \mathbf{S}\mathbf{F}^T = \mathbf{F}\mathbf{S}^T, \qquad [\![\mathbf{S}]\!]\cdot\boldsymbol{\mathcal{N}} - \mathbf{T} = \mathbf{0} \quad \text{on} \quad \partial\mathcal{V}_0 \setminus \partial\mathcal{V}_0^{\mathbf{u}}, \tag{2}$$

where $\partial\mathcal{V}_0^{\mathbf{u}}$ and $\mathbf{T}$ denote the displacement Dirichlet part of the solid boundary and the mechanical traction in the reference configuration. One may write the equivalent form of the equilibrium, symmetry and boundary conditions in the current configuration by introducing the Cauchy stress $\boldsymbol{\sigma}$, such that

$$\mathrm{div}\ \boldsymbol{\sigma} = \mathbf{0} \quad \text{in} \quad \mathbb{R}^3, \qquad \boldsymbol{\sigma} = \boldsymbol{\sigma}^T, \qquad [\![\boldsymbol{\sigma}]\!]\cdot\mathbf{n} - \mathbf{t} = \mathbf{0} \quad \text{on} \quad \partial\mathcal{V} \setminus \partial\mathcal{V}^{\mathbf{u}}. \tag{3}$$

Here, $\partial\mathcal{V}^{\mathbf{u}}$ and $\mathbf{t}$ denote the displacement Dirichlet part of the solid boundary and the mechanical traction in the current configuration, respectively. One may show using a push forward or pull-back transformation that (Ogden, 1997)

$$\boldsymbol{\sigma} = \frac{1}{J}\mathbf{S}\mathbf{F}^T, \qquad \text{or} \qquad \mathbf{S} = J\,\boldsymbol{\sigma}\,\mathbf{F}^{-T}. \tag{4}$$

The above definitions are standard in continuum mechanics and will not be further analyzed.

2.2. Magnetostatics

Following the seminal works of Maxwell (1861,1865,1873), a set of equivalent balance laws may be derived in the context of magnetism. For such derivations, one may refer to several textbooks or thesis documents, such as the recent thesis manuscript of Mukherjee (2020). We proceed by briefly recalling those laws and definitions. Traditionally, in the physics community and in the absence of electric currents and charges, one may use three quantities to describe the magnetic state of a solid in the *current* configuration:

- the magnetic field $\mathbf{b}$,
- the h-field $\mathbf{h}$,
- the magnetization $\mathbf{m}$ which is naturally zero in non-magnetic domains.

It is important to note, however, that those three quantities are not independent of each other. They are related by the *constitutive* relation

$$\mathbf{b} = \mu_0(\mathbf{h} + \mathbf{m}) \qquad \text{or} \qquad \mathbf{m} = \frac{1}{\mu_0}\mathbf{b} - \mathbf{h} \qquad \text{in} \quad \mathcal{V}, \tag{5}$$

where μ_0 is the magnetic permeability of vaccuum, air or non-magnetic solids.

Remark 1. In fact, the second expression in (5) is a *definition* of the magnetization vector in the current volume $\mathcal{V}$, which however is not defined on its boundary $\partial\mathcal{V}$. By definition $\mathbf{m} = \mathbf{0}$ in a non-magnetic body. This implies that as a quantity is insufficient to describe the presence of magnetic lines (in the sense of Maxwell) in the surrounding air or in a non-magnetic solid such as the polymer matrix which is also of interest here. In these two last cases, one is left with the relation $\mathbf{b} = \mu_0\mathbf{h}$, which implies–in the sense of a continuum medium–that $\mathbf{b}$ is linearly dependent on $\mathbf{h}$ and *vice versa* via the constitutive parameter μ_0. Henceforth, we will focus on the original Maxwell fields $\mathbf{b}$ and $\mathbf{h}$ as independent variables that are related via linear and/or nonlinear constitutive laws, while $\mathbf{m}$ will serve as a quantity that can be readily computed by equation (5), but instead will not be considered as an "independent" variable itself. In fact, in Section 7.1 we show by example that $\mathbf{m}$ may be regarded as an internal state variable in most of the cases.

2.2.1. Ampère's law

`Assumptions.` The present study pertains to magneto-mechanical problems ignoring all electrical effects. This suggests that, henceforth, we consider that any effects resulting from electric charges, electric fields and varying electric displacements are negligible. Moreover, this implies that any variations of magnetic fields should be sufficiently small such that $\partial\mathbf{b}/\partial t$ is negligible. Thus, we do not deal with high frequency effects in the present study. Moreover for further simplicity, we assume that there exist no surface currents $\mathbf{k}$ throughout this work and there are no relativistic effects in the matter.

`Current configuration.` In the general case of free volume currents, $\mathbf{j}$, running across a surface $\partial\mathcal{V}$ in the current configuration, but in the absence of electric charges and time varying electric displacements (i.e., $\partial\mathbf{d}/\partial t$) and surface currents (known as the Eddy current approximation), Ampère's law takes the following form (dropping for simplicity the explicit dependence on $\mathbf{x}$):

$$\oint_C \mathbf{h} \cdot \mathrm{d}\boldsymbol{\ell} = \int_{\partial\mathcal{V}} \mathbf{j} \cdot \mathbf{n}\, \mathrm{d}\mathcal{S}. \tag{6}$$

In this equation, C is a smooth arbitrary closed curve lying on the smooth closed surface $\partial\mathcal{V}$, $\mathrm{d}\boldsymbol{\ell}$ is an infinitesimal line element with direction tangent to the curve C, and $\mathbf{n}$ is the outward normal to $\partial\mathcal{V}$. By assuming sufficient smoothness of $\mathbf{h}$, use of the standard Stokes theorem leads to the differential form of (6), which reads

$$\int_{\partial\mathcal{V}} \operatorname{curl}\mathbf{h} \cdot \mathbf{n}\, \mathrm{d}\mathcal{S} = \int_{\partial\mathcal{V}} \mathbf{j} \cdot \mathbf{n}\, \mathrm{d}\mathcal{S}, \tag{7}$$

where the operator curl is defined with respect to the deformed position $\mathbf{x}$.

In order to retrieve seamlessly the boundary conditions along a given interface, one may generalize this last result to the case of a surface $\partial\mathcal{V}$ containing a hypothetical *line of discontinuity* (an argument that will be subsequently dropped) γ where the corresponding integrand $\operatorname{curl}\mathbf{h}$ is not defined. In that case, by use of the modified Stoke's theorem (Eringen, 1967; Eringen and Maugin, 1990), the last equation may be rewritten as

$$\int_{\partial\mathcal{V}\setminus\gamma} \operatorname{curl}\mathbf{h} \cdot \mathbf{n}\, \mathrm{d}\mathcal{S} + \oint_{\gamma} [\![\mathbf{h}]\!] \cdot \mathrm{d}\boldsymbol{\ell} = \int_{\partial\mathcal{V}\setminus\gamma} \mathbf{j} \cdot \mathbf{n}\, \mathrm{d}\mathcal{S}, \tag{8}$$

where continuity of $\mathbf{j}$ is considered along the surface $\partial\mathcal{V}$.

These last integrals together with the arbitrary nature of the surface S and the localization lemma lead readily to the pointwise differential equations and jump conditions (Eringen and Maugin, 1990)

$$\operatorname{curl}\mathbf{h}=\mathbf{j}\quad\text{in}\quad\mathcal{V},\qquad[\![\mathbf{h}]\!]\times\mathbf{n}=\mathbf{0}\quad\text{on}\quad\partial\mathcal{V}. \tag{9}$$

In the absence of free currents, i.e., $\mathbf{j}=\mathbf{0}$, Ampère's law (9) reads

$$\operatorname{curl}\mathbf{h}=\mathbf{0}\quad\text{in}\quad\mathcal{V},\qquad[\![\mathbf{h}]\!]\times\mathbf{n}=\mathbf{0}\quad\text{on}\quad\partial\mathcal{V}. \tag{10}$$

The last relation also holds in the air domain which may extend to $\mathbb{R}^3\setminus\mathcal{V}$ or in non-magnetic domains enclosed in $\mathcal{V}$. Moreover, this last form will be used in most of this study, while (9) has been used in the study of Dorn et al. (2021) but is not included in the present notes.

`Reference configuration.` In an exactly similar fashion, one may rewrite the above laws in the reference configuration. This is a necessary operation in the present work, since we deal with finite strains and it is natural to use Lagrangian measures. Thus, in the general case of free volume currents, $\mathbf{J}$, running across a surface $\partial\mathcal{V}_0$ in the reference configuration and in the absence of surface currents $\mathbf{K}$), electric charges and time varying electric displacements (i.e., $\partial\mathbf{D}/\partial t$), Ampère's law takes the following form (using also the standard Stoke's theorem):

$$\begin{aligned}&\oint_{C_0}\mathbf{h}(\mathbf{X})\cdot\mathbf{F}\mathrm{d}\boldsymbol{\ell}_0=\int_{\partial\mathcal{V}_0}\mathbf{j}\cdot J\mathbf{F}^{-T}\boldsymbol{\mathcal{N}}\,\mathrm{d}\mathcal{S}_0\qquad\text{or}\\&\int_{\partial\mathcal{V}_0}\operatorname{Curl}\mathbf{H}\cdot\boldsymbol{\mathcal{N}}\,\mathrm{d}\mathcal{S}_0=\int_{\partial\mathcal{V}_0}\mathbf{J}\cdot\boldsymbol{\mathcal{N}}\,\mathrm{d}\mathcal{S}.\end{aligned} \tag{11}$$

Here, C_0 is a smooth arbitrary closed curve lying on the smooth closed surface $\partial\mathcal{V}_0$, $\mathrm{d}\boldsymbol{\ell}_0$ is an infinitesimal line element with direction tangent to the curve C_0, $\boldsymbol{\mathcal{N}}$ is the outward normal to $\partial\mathcal{V}_0$ and the operator Curl is defined with respect to the undeformed position $\mathbf{X}$. Moreover, we have used the Lagrangian definitions

$$\mathbf{H}=\mathbf{F}^T\mathbf{h},\quad\mathbf{J}=J\,\mathbf{F}^{-1}\mathbf{j},\qquad\text{or}\qquad\mathbf{h}=\mathbf{F}^{-T}\mathbf{H},\quad\mathbf{j}=J^{-1}\,\mathbf{F}\mathbf{J}, \tag{12}$$

as well as the standard line and surface (i.e., Nahnson formula) transformations between the current and reference configuration

$$\mathrm{d}\boldsymbol{\ell}=\mathbf{F}\mathrm{d}\boldsymbol{\ell}_0,\qquad\mathbf{n}\mathrm{d}\mathcal{S}=J\mathbf{F}^{-T}\boldsymbol{\mathcal{N}}\mathrm{d}\mathcal{S}_0. \tag{13}$$

Again considering a hypothetical *line of discontinuity* (an argument that will be subsequently dropped) Γ where the integrand Curl$\mathbf{H}$ may not be defined, the second integral equation in (11) can be written as

$$\int_{\partial\mathcal{V}_0\setminus\Gamma}\operatorname{Curl}\mathbf{H}\cdot\boldsymbol{\mathcal{N}}\,\mathrm{d}\mathcal{S}_0+\oint_{C\setminus\Gamma}[\![\mathbf{H}]\!]\times\boldsymbol{\mathcal{N}}\,\mathrm{d}\boldsymbol{\ell}_0=\int_{\partial\mathcal{V}_0}\mathbf{J}\cdot\boldsymbol{\mathcal{N}}\,\mathrm{d}\mathcal{S}. \tag{14}$$

Given the arbitrariness of the surface $\partial\mathcal{V}_0$ and curves C_0 and Γ, the above operations readily lead by use of the localization lemma to the pointwise differential equations

$$\operatorname{Curl}\mathbf{H}=\mathbf{J}\quad\text{in}\quad\mathcal{V}_0,\qquad[\![\mathbf{H}]\!]\times\boldsymbol{\mathcal{N}}=\mathbf{0}\quad\text{on}\quad\partial\mathcal{V}_0. \tag{15}$$

In the absence of free currents, i.e., $\mathbf{J} = \mathbf{0}$, Ampère's law (9) reads

$$\mathrm{Curl}\,\mathbf{H} = \mathbf{0} \quad \text{in} \quad \mathcal{V}_0, \qquad [\![\mathbf{H}]\!] \times \boldsymbol{\mathcal{N}} = \mathbf{0} \quad \text{in} \quad \partial\mathcal{V}_0. \tag{16}$$

The last relation also holds in the air domain which may extend to $\mathbb{R}^3 \setminus \mathcal{V}_0$ or in non-magnetic domains enclosed in $\mathcal{V}_0$.

Definition 2 (Scalar potential)**.** In the absence of free currents, i.e., when $\mathbf{J} = \mathbf{0}$, one may define a scalar potential $\varphi(\mathbf{X})$ such that

$$\mathbf{H}(\mathbf{X}) = -\mathrm{Grad}\varphi(\mathbf{X}) \tag{17}$$

which implies

$$\mathrm{Curl}(\mathrm{Grad}\varphi) = \mathbf{0} \quad \text{in} \quad \mathcal{V}_0 \qquad [\![\varphi]\!] = 0 \quad \text{in} \quad \partial\mathcal{V}_0.$$

This definition allows to satisfy identically relation $(16)_1$, since the curl of a gradient of a scalar field is identically zero. This definition is extremely useful since it allows to satisfy one of the two Maxwell equations (see the second equation in the next section). This condition is similar to the one in mechanics, where the deformation gradient is given in terms of the gradient of a displacement vector field and in that case one satisfies identically the compatibility condition $\mathrm{Curl}\mathbf{F} = \mathbf{0}$.

It is noted here that one could define in a similar fashion a scalar potential in the current configuration. Nonetheless, in the present work, all variables will be defined in the reference configuration and thus such a definition is not of use. Furthermore, in a small strain setting the reference and current configurations coincide and again such a distinction becomes inconsequential.

2.2.2. Absence of magnetic monopole - Faraday's law

`Current configuration.` Under the same assumptions stated in the previous section and under the hypothesis of the absence of magnetic monopole, the normal component of a sufficiently smooth magnetic field $\mathbf{b}(\mathbf{x})$ integrated over a closed smooth surface $\partial\mathcal{V}$ vanishes identically, such that

$$\int_{\partial\mathcal{V}} \mathbf{b} \cdot \mathbf{n}\, \mathrm{d}\mathcal{S} = 0. \tag{18}$$

Use of the modified divergence theorem (Eringen, 1967) considering potential jumps across a discontinuous surface s leads to

$$\int_{\mathcal{V}\setminus s} \mathrm{div}\mathbf{b}\, \partial\mathcal{V} + \int_s [\![\mathbf{b}]\!] \cdot \mathbf{n}\, \mathrm{d}\mathcal{S} = 0. \tag{19}$$

Using the localization lemma and the arbitrariness of the volume $\mathcal{V}$ and the surfaces $\partial\mathcal{V}$ and s, we obtain the general pointwise balance equations and boundary conditions

$$\mathrm{div}\mathbf{b} = 0 \quad \text{in} \quad \mathcal{V}, \qquad [\![\mathbf{b}]\!] \cdot \mathbf{n} = 0 \quad \text{on} \quad \partial\mathcal{V}. \tag{20}$$

Again, this last relation also holds in the air domain which may extend to $\mathbb{R}^3 \setminus \mathcal{V}$ or in non-magnetic domains enclosed in $\mathcal{V}$.

`Reference configuration.` Similarly, one may obtain the corresponding balance laws in the reference configuration by using the transformations (13) in (18) and the modified divergence theorem to write

$$\int_{\partial\mathcal{V}_0} \mathbf{b}\cdot J\mathbf{F}^{-T}\boldsymbol{\mathcal{N}}\,\mathrm{d}\mathcal{S}_0 = 0 \quad \Rightarrow \quad \int_{\partial\mathcal{V}_0\setminus\Sigma} \mathrm{Div}\mathbf{B}\,\partial\mathcal{V}_0 + \int_{\Sigma} [\![\mathbf{B}]\!]\cdot\boldsymbol{\mathcal{N}}\,\mathrm{d}\mathcal{S}_0 = 0, \tag{21}$$

Here, again, $\partial\mathcal{V}_0$ is a closed surface in the undeformed configuration, Σ a discontinuous surface, while the operator Div is defined with respect to the undeformed position $\mathbf{X}$. Moreover, we have used the definitions

$$\mathbf{B} = J\,\mathbf{F}^{-1}\mathbf{b}, \qquad \text{or} \qquad \mathbf{b} = J^{-1}\,\mathbf{F}\mathbf{B}. \tag{22}$$

Using again the fundamental lemma of the variational calculus for the arbitrariness of the $\mathcal{V}_0$ and $\partial\mathcal{V}_0$, we obtain the pointwise balance equations and boundary conditions

$$\mathrm{Div}\mathbf{B} = 0 \quad \text{in} \quad \mathcal{V}_0, \qquad [\![\mathbf{B}]\!]\cdot\boldsymbol{\mathcal{N}} = 0 \quad \text{in} \quad \partial\mathcal{V}_0. \tag{23}$$

Again, this last relation also holds in the air domain which may extend to $\mathbb{R}^3\setminus\mathcal{V}_0$ or in non-magnetic domains enclosed in $\mathcal{V}_0$.

Definition 3 (Vector potential)**.** One may *always* define a vector potential $\mathbf{A}(\mathbf{X})$ such that

$$\mathbf{B}(\mathbf{X}) = \mathrm{Curl}\mathbf{A}(\mathbf{X}), \tag{24}$$

which implies

$$\mathrm{Div}(\mathrm{Curl}\mathbf{A}) = 0 \quad \text{in} \quad \mathcal{V}_0, \qquad [\![\mathbf{A}]\!]\times\boldsymbol{\mathcal{N}} = 0 \quad \text{in} \quad \partial\mathcal{V}_0.$$

This definition allows to satisfy identically relation $(23)_1$, since the divergence of a curl of a vector field is identically zero. This condition is similar to the one in mechanics, where the stress field may be written in terms of an Airy stress function thus allowing to satisfy identically the equilibrium equations $\mathrm{Div}\mathbf{S} = \mathbf{0}$ (in the absence of body forces and inertial terms).

Again, it is noted here that one could define in a similar fashion a vector potential in the current configuration. Nonetheless, in the present work, all variables will be defined in the reference configuration and thus such a definition is not of use. In turn, in a small strain setting the reference and current configurations coincide and such a distinction becomes inconsequential.

For simplicity, we can summarize the main transformation rules that will be extensively used in the following between Eulerian and Lagrangian quantities as

$$\boldsymbol{\sigma} = \frac{1}{J}\mathbf{S}\mathbf{F}^T, \qquad \mathbf{b} = \frac{1}{J}\mathbf{F}\mathbf{B} \qquad \text{and} \qquad \mathbf{h} = \mathbf{F}^{-T}\mathbf{H}. \tag{25}$$

3. Thermodynamics and general variational formulations

In this section, we present a general incremental thermodynamically consistent variational framework allowing to describe in a general manner dissipative and nonlinear magnetoelastic solids. The presentation that follows is carried out such that stationarity of the variational formulations leads to the previously defined balance laws and boundary conditions. Moreover, one of the pilars of the proposed framework is the Generalized Standard Materials (GSM) approach (Halphen and Son Nguyen, 1975). Therein, we assume that there exists an energy density W and a dissipation

potential D that depend respectively on the chosen independent variables and their rates. The subsequent formulations include therefore the balance laws and Maxwell equations, the boundary conditions and the magneto-mechanical constitutive material laws. This is, in our opinion, the most elegant and concise manner to describe the magneto-mechanical solids of interest here. On the contrary, they are not absolutely necessary in the sense that the set of derived equations are those used in practice to carry out the simulations. Note, however, that writing the problem in a minimum energy principle allows in some cases of interest to obtain rigorous results in the context of instabilities.

Remark 4. Henceforth, we propose two equivalent formulations the $\mathbf{F}-\mathbf{H}$ and the $\mathbf{F}-\mathbf{B}$ one, and as their name states clearly the first considers the magnetic scalar potential and the second the magnetic vector potential as independent magnetic variables, respectively. An alternative formulation may use an additional variable, $\mathbf{m}$ (Danas et al., 2012; Danas and Triantafyllidis, 2014). Such formulation still is equivalent to the first two (see for example the appendix in Danas (2017), or Bustamante et al. (2008) and more recently Sharma and Saxena (2020)). Nevertheless, $\mathbf{m}$ is not a sufficiently general variable but instead is defined via the equation (5). The main reason for this is that one cannot use only $\mathbf{m}$ and apply magnetic boundary conditions, since it is not defined at the boundary (or at interfaces) as opposed to $\mathbf{h}$ or $\mathbf{b}$ (see discussion in Section 3). Even so, in some problems involving magnetic domains and permanently magnetized solids that the state of magnetization is given in terms of a *known* amplitude and a direction locally, it might be advantageous to work directly with $\mathbf{m}$ to obtain analytical and numerical solutions (James and Kinderlehrer, 1993; DeSimone and James, 2002; Keip and Sridhar, 2018). In the present case, however, since we are interested in solving general boundary value problems, one must retain either φ or $\mathbf{A}$ to analyze the magnetic fields in non-magnetic domains (e.g., matrix or air), where the magnetization is null. Thus the addition of $\mathbf{m}$ does not offer any clear advantage, instead it requires additional numerical approximations (such as static condensation in order to deal with jumps across interfaces).

3.1. Scalar potential-based F-H formulation

In this formulation, we consider the mechanical deformation $\mathbf{u}$ and the scalar magnetic potential φ to be the independent primary variables along with a set of internal variables $\boldsymbol{\xi}$ [2]. For this to be valid, we need to assume also that we have no free currents, i.e., $\mathbf{J}=\mathbf{0}$. The case of free currents can only be considered in the $\mathbf{F}-\mathbf{B}$ setting presented in the following section.

Following the statements in Section 2.2, one may define the rate of the potential energy stored in the system, shown in Fig. 1, as

$$\dot{\mathscr{P}}^{\mathtt{H}} = \frac{\mathrm{d}}{\mathrm{d}t}\int_{\mathbb{R}^3} W^{\mathtt{H}}(\mathbb{C},\mathbf{H},\boldsymbol{\xi})\ \mathrm{d}\mathcal{V}_0 - \int_{\partial\mathcal{V}_0\setminus\partial\mathcal{V}_0^{\mathbf{u}}} \mathbf{T}\cdot\dot{\mathbf{u}}\ \mathrm{d}\mathcal{S}_0. \tag{26}$$

Here, $W^{\mathtt{H}}(\mathbb{C},\mathbf{H},\boldsymbol{\xi})$ is the local potential energy density, where $\mathbb{C}=\mathbf{F}^T\mathbf{F}$ is the right Cauchy-Green tensor and $\mathbf{T}$ is the mechanical traction. The operators $\dot{(\blacksquare)}$ and $\mathrm{d}/\mathrm{d}t$ in (26) denote the material time derivative. Notice that the local energy density $W^{\mathtt{H}}(\mathbf{F},\mathbf{H},\boldsymbol{\xi})$ is non-zero both inside and outside $\mathcal{V}_0$, which is typical in the magneto-mechanical formulation (Kankanala and Triantafyllidis,

[2] For the moment, we keep $\boldsymbol{\xi}$ general and a more precise choice will be done further below. This choice depends on the dissipative mechanisms that are modeled. For instance viscous strains and/or magnetic dissipation.

2004). Nonetheless, for (26) to be bounded, the energy $W^{\mathtt{H}}$ must vanish as $|\mathbf{X}| \to \infty$, which is a realistic condition. In practice, in realistic and numerical boundary value problems, we always analyze finite domains that are subsets of $\mathbb{R}^3$. Those domains are sufficiently large allowing for the magnetic fields to reach an approximately zero value at their external boundary. More discussion about this point will be carried out further below.

The dissipation potential $\mathscr{D}$ associated with the solid is also given in terms of the local dissipation potential D, such that

$$\mathscr{D} = \int_{\mathcal{V}_0} D(\dot{\boldsymbol{\xi}}; \mathbb{C}, \mathbf{H}, \boldsymbol{\xi}) \, \mathrm{d}\mathcal{V}_0. \tag{27}$$

Notice that the dissipation is only considered inside the solid domains, whereas it vanishes identically for all $\mathbf{X} \in \mathbb{R}^3 \setminus \mathcal{V}_0$. In addition, it is a principal function of the rate of the internal variable $\dot{\boldsymbol{\xi}}$, while the use of $\mathbb{C}$,$\mathbf{H}$ and $\boldsymbol{\xi}$ indicates mainly a history dependence.

With the above definitions in place, we propose an incremental variational principle following the seminal works of Onsager (1931a,b), such that

$$\dot{\Pi}^{\mathtt{H}} = \inf_{\dot{\mathbf{u}} \in \widetilde{\mathcal{U}}} \sup_{\dot{\varphi} \in \widetilde{\mathcal{G}}} \inf_{\dot{\boldsymbol{\xi}}} \Big[\dot{\mathscr{P}}^{\mathtt{H}} + \mathscr{D} \Big]. \tag{28}$$

The admissible sets for $\dot{\mathbf{u}}$ and $\dot{\varphi}$ are given by

$$\begin{aligned} \widetilde{\mathcal{U}} \equiv \Big\{ \dot{\mathbf{u}}(\mathbf{X}) : & \dot{\mathbf{F}}(\mathbf{X}) = \mathrm{Grad}\, \dot{\mathbf{u}}(\mathbf{X}) \ \ \forall\, \mathbf{X} \in \mathbb{R}^3, \\ & \pi(\dot{\mathbf{u}}(\mathbf{X})) = \pi(\dot{\bar{\mathbf{u}}}(\mathbf{X})) \ \ \forall\, \mathbf{X} \in \partial\mathcal{V}_0^{\mathbf{u}} \Big\} \end{aligned} \tag{29}$$

and

$$\begin{aligned} \widetilde{\mathcal{G}} \equiv \Big\{ \dot{\varphi}(\mathbf{X}) : & \dot{\mathbf{H}}(\mathbf{X}) = -\mathrm{Grad}\, \dot{\varphi}(\mathbf{X}) \ \ \forall\, \mathbf{X} \in \mathbb{R}^3, \\ & \dot{\varphi}(\mathbf{X}) = \dot{\bar{\varphi}}(\mathbf{X}) \ \ \forall\, \mathbf{X} \in \partial\mathcal{V}_\infty^{\varphi} \Big\}, \end{aligned} \tag{30}$$

respectively. The symbol π in (29) denotes a projection operator that enables applying the constraints only on certain components on $\dot{\mathbf{u}}$ for all $\mathbf{X}$ on the domain boundary $\partial\mathcal{V}_0^{\mathbf{u}}$, where the displacement is constrained to vary with a reference rate $\dot{\bar{\mathbf{u}}}$. Similarly, the boundary where the magnetic potential φ varies according to a given rate $\dot{\bar{\varphi}}$ is denoted as $\partial\mathcal{V}_\infty^{\varphi}$. Since the magnetic fields are typically applied at a distance (and usually far away) from the MRE sample, we consider $\partial\mathcal{V}_\infty^{\varphi}$ to be a boundary surface enclosing the solid's boundary $\partial\mathcal{V}_0$. This particular consideration, of course, does *not* affect the generality of the variational principle (28) and different boundary conditions on φ may be imposed.

The stationarity conditions for $\dot{\Pi}^{\mathtt{H}}$ along with the arbitrariness of the considered volume element in $\mathcal{V}_0$ leads to the local governing equations and the boundary conditions in this scalar potential formulation. Thus, straightforward algebraic manipulations (see Kankanala and Triantafyllidis

(2004) or Bustamante et al. (2008) for instance) leads to

$$\text{Div } \mathbf{S} = \mathbf{0} \text{ in } \mathbb{R}^3, \quad \mathbf{S} = 2\mathbf{F}\frac{\partial W^{\mathtt{H}}}{\partial \mathbb{C}}, \quad [\![\mathbf{S}]\!] \cdot \boldsymbol{\mathcal{N}} - \mathbf{T} = \mathbf{0} \text{ on } \partial\mathcal{V}_0 \setminus \partial\mathcal{V}_0^{\mathbf{u}}, \tag{31}$$

$$\text{Div } \mathbf{B} = 0 \text{ in } \mathbb{R}^3, \quad \mathbf{B} = -\frac{\partial W^{\mathtt{H}}}{\partial \mathbf{H}}, \quad [\![\mathbf{B}]\!] \cdot \boldsymbol{\mathcal{N}} = 0 \text{ on } \partial\mathcal{V}_0, \tag{32}$$

$$\frac{\partial W^{\mathtt{H}}}{\partial \boldsymbol{\xi}} + \frac{\partial D}{\partial \dot{\boldsymbol{\xi}}} = \mathbf{0} \quad \text{for all} \quad \mathbf{X} \in \mathcal{V}_0, \quad \text{with } \boldsymbol{\mathcal{B}}^r = \frac{\partial D}{\partial \dot{\boldsymbol{\xi}}} = -\frac{\partial W^{\mathtt{H}}}{\partial \boldsymbol{\xi}}. \tag{33}$$

Here, $\boldsymbol{\mathcal{B}}^r$ is the work conjugate to the corresponding internal variable $\boldsymbol{\xi}$. We see thus that the stationarity of $\dot{\Pi}^{\mathtt{H}}$ leads to the field balance equations and boundary conditions described in Section **??**. In addition, it provides via the definition of the energy density $W^{\mathtt{H}}$, the corresponding constitutive relations. Finally, the variational principle also leads to the GSM relation $(33)_1$, which provides, in fact, the local evolution equation for the internal variable $\boldsymbol{\xi}$. Notice that unlike the primary variables $\mathbf{u}$ and φ, the internal variable $\boldsymbol{\xi}$ *does not* need to satisfy any differential or boundary constraints. Moreover, the evolution equation $(33)_1$ only holds in the MRE domain, i.e., for all $\mathbf{X} \in \mathcal{V}_0$.

Entropy imbalance and constraint on $D(\dot{\boldsymbol{\xi}})$: The local form of the entropy imbalance equation, also known as the Clausius-Duhem inequality reads for the $\mathbf{F} - \mathbf{H}$ model

$$\mathbf{S} : \dot{\mathbf{F}} - \mathbf{B} \cdot \dot{\mathbf{H}} - \dot{W}^{\mathtt{H}}(\mathbb{C}, \mathbf{H}, \boldsymbol{\xi}) \geq 0. \tag{34}$$

Expanding the derivative $\dot{W}^{\mathtt{H}}$ followed by substitutions of the constitutive relations $(31)_1$, $(32)_1$ and $(33)_1$ into (34), we obtain

$$\frac{\partial D}{\partial \dot{\boldsymbol{\xi}}} \cdot \dot{\boldsymbol{\xi}} \geq 0, \tag{35}$$

which is typically referred as the dissipation inequality. Notably, any function $D(\dot{\boldsymbol{\xi}}; \mathbb{C}, \mathbf{H}, \boldsymbol{\xi})$ that is convex in $\dot{\boldsymbol{\xi}}$ satisfies automatically the dissipation inequality, thus ensuring positive dissipation during any loading/unloading operation.

3.2. Vector potential-based F-B formulation

In this section, we provide a dual formulation (under certain conditions) to the previous $\mathbf{F} - \mathbf{H}$ one. Specifically, we derive the local balance laws and constitutive relations for an equivalent *dual* $\mathbf{F} - \mathbf{B}$-based formulation. Notice that, the $\mathbf{B}$ field is divergence-free and hence is now expressed in terms of a vector potential $\mathbf{A}$, as defined in (24). In this formulation, we consider $\mathbf{u}$ and $\mathbf{A}$ to be the primary variables, whereas the internal variable remains the same, i.e., $\boldsymbol{\xi}$.

The rate of total potential energy is then given by

$$\dot{\mathscr{P}}^{\mathtt{B}} = \frac{\mathrm{d}}{\mathrm{d}t} \int_{\mathbb{R}^3} W^{\mathtt{B}}(\mathbb{C}, \mathbf{B}, \boldsymbol{\xi}) \, \mathrm{d}\mathcal{V}_0 - \int_{\partial\mathcal{V}_0} \mathbf{T} \cdot \dot{\mathbf{u}} \, \mathrm{d}\mathcal{S}_0 \tag{36}$$

with

$$W^{\mathtt{B}}(\mathbb{C}, \mathbf{B}, \boldsymbol{\xi}) = \sup_{\mathbf{H}} \Big[W^{\mathtt{H}}(\mathbb{C}, \mathbf{H}, \boldsymbol{\xi}) + \mathbf{H} \cdot \mathbf{B} \Big], \tag{37}$$

which is the partial Legendre-Fenchel transform of $W^{\mathtt{H}}(\mathbb{C}, \mathbf{H}, \boldsymbol{\xi})$ with respect to $\mathbf{H}$ (Bustamante et al., 2008). In turn, the dissipation potential, $\mathscr{D}$, is defined only in terms of the rate of the internal

variable $\dot{\boldsymbol{\xi}}$ from equation (27) and thus is identical to that introduced in the $\mathbf{F}-\mathbf{H}$ formulation. Thus, the minimization variational principle in terms of $\dot{\mathscr{P}}^{\mathtt{B}}$ and $\mathscr{D}$ now reads

$$\dot{\Pi}^{\mathtt{B}} \;=\; \inf_{\dot{\mathbf{u}}\in\widetilde{\mathcal{U}}} \;\inf_{\dot{\mathbf{A}}\in\widetilde{\mathcal{B}}} \;\inf_{\dot{\boldsymbol{\xi}}} \;\Big[\; \dot{\mathscr{P}}^{\mathtt{B}} + \mathscr{D} \;\Big], \tag{38}$$

where the admissible set $\widetilde{\mathcal{U}}$ for the rate $\dot{\mathbf{u}}$ is given by (29) and that for $\dot{\mathbf{A}}$ reads[3]

$$\widetilde{\mathcal{B}} \equiv \Big\{ \dot{\mathbf{A}}(\mathbf{X}) : \dot{\mathbf{B}}(\mathbf{X}) = \text{Curl}\; \dot{\mathbf{A}}(\mathbf{X}) \;\; \forall\, \mathbf{X}\in\mathbb{R}^3,\; \dot{\mathbf{A}}(\mathbf{X}) = \overline{\dot{\mathbf{A}}}(\mathbf{X}) \;\; \forall\, \mathbf{X}\in\partial\mathcal{V}_\infty^{\mathbf{A}} \Big\}, \tag{39}$$

where the specific rate $\overline{\dot{\mathbf{A}}}$ is considered on the boundary $\partial\mathcal{V}_\infty^{\mathbf{A}}$ that encloses the MRE solid boundary $\partial\mathcal{V}_0$. Note further that contrary to (26) which is a saddle point stationary principle, the $\mathbf{F}-\mathbf{B}$ potential (36) is a purely minimization principle.

In this regard, minimization of $\dot{\Pi}^{\mathtt{B}}$ with respect to the rates $\dot{\mathbf{u}}$, $\dot{\mathbf{A}}$ and $\dot{\boldsymbol{\xi}}$ leads to the local balance laws, constitutive relations along with the boundary conditions, so that

$$\text{Div}\; \mathbf{S} = \mathbf{0} \;\text{in}\; \mathbb{R}^3, \quad \mathbf{S} = 2\mathbf{F}\frac{\partial W^{\mathtt{B}}}{\partial \mathbb{C}}, \quad [\![\mathbf{S}]\!]\cdot\boldsymbol{\mathcal{N}} - \mathbf{T} = \mathbf{0}\,\text{on}\,\partial\mathcal{V}_0 \setminus \partial\mathcal{V}_0^{\mathbf{u}}, \tag{40}$$

$$\text{Curl}\; \mathbf{H} = \mathbf{0} \;\text{in}\; \mathbb{R}^3, \quad \mathbf{H} = \frac{\partial W^{\mathtt{B}}}{\partial \mathbf{B}}, \quad \boldsymbol{\mathcal{N}}\times[\![\mathbf{H}]\!] = \mathbf{0}\,\text{on}\,\partial\mathcal{V}_0, \tag{41}$$

$$\frac{\partial W^{\mathtt{B}}}{\partial \boldsymbol{\xi}} + \frac{\partial D}{\partial \dot{\boldsymbol{\xi}}} = \mathbf{0} \quad \text{for all} \;\; \mathbf{X}\in\mathcal{V}_0, \;\; \text{with}\; \boldsymbol{\mathcal{B}}^r = \frac{\partial D}{\partial \dot{\boldsymbol{\xi}}} = -\frac{\partial W^{\mathtt{B}}}{\partial \boldsymbol{\xi}}. \tag{42}$$

Notice that (40) and (42) remain identical to (31) and (33), respectively, with the only difference being the replacement of $W^{\mathtt{H}}$ with $W^{\mathtt{B}}$. The minimization of $\dot{\Pi}^{\mathtt{B}}$ with respect to $\dot{\mathbf{A}}$ yields the local balance law $(41)_1$, constitutive relation $(41)_2$ and the interface/boundary condition $(41)_3$ on $\partial\mathcal{V}_0$.

The $\mathbf{F}-\mathbf{B}$ version of the local Clausius-Duhem inequality can be readily obtained by substituting (37) into (34). In turn, the dissipation inequality can be derived *mutatis mutandis* from the $\mathbf{F}-\mathbf{H}$ case. In fact, the final form of the dissipation inequality remains identical to (35).

Remark 5. The above potential energy may be modified in a straighforward manner to include the Eddy current approximation and free volume currents $\mathbf{J}$, such that

$$\dot{\mathscr{P}}^{\mathtt{B}} = \frac{\mathrm{d}}{\mathrm{d}t}\int_{\mathbb{R}^3} W^{\mathtt{B}}(\mathbb{C},\mathbf{B},\boldsymbol{\xi})\;\mathrm{d}\mathcal{V}_0 - \int_{\partial\mathcal{V}_0}\mathbf{T}\cdot\dot{\mathbf{u}}\;\mathrm{d}\mathcal{S}_0 - \int_{\mathcal{V}_0}\mathbf{J}\cdot\dot{\mathbf{A}}\;\mathrm{d}\mathcal{V}_0. \tag{43}$$

Then the only equation changing in the local balance laws is $(41)_1$, which becomes $\text{Curl}\;\mathbf{H} = \mathbf{J}$ in $\mathcal{V}_0$. The free volume current is effectively a body force term in domains that the magnetic vector potential $\dot{\mathbf{A}} \neq \mathbf{0}$.

[3]The numerical solution for the three-dimensional vector potential-based BVPs requires an additional constraint on $\mathbf{A}$, namely, $\text{Div}\;\mathbf{A} = 0$, commonly referred as the Coulomb gauge. The latter is not necessary in a two-dimensional problem, whereas the three dimensional implementation is discussed further below.

4. Modeling of isotropic hard-MREs

In this section, we lay out the constitutive laws necessary to describe the response of isotropic incompressible h-MREs. The procedure is of course general, however, the choice of functions pertains *only* to the specific class of materials analyzed here.

Before we proceed to specific constitutive propositions, we discuss first the constraints that need to be imposed on the energetic and dissipation potentials, $W^{\mathtt{H}}$ or $W^{\mathtt{B}}$ and D, respectively, in order to ensure (a) an even magneto-mechanical coupling, (b) material frame indifference, (c) isotropic material symmetry and (d) positive dissipation. For conciseness, we will use the symbol

$$\mathbf{G} = \begin{cases} \mathbf{H}, & \text{if } \mathbf{F}-\mathbf{H} \text{ formulation} \\ \mathbf{B}, & \text{if } \mathbf{F}-\mathbf{B} \text{ formulation} \end{cases} \tag{44}$$

to denote compactly the two formulations, wherever that is possible.

4.1. Internal variable for magnetic dissipation

A thermodynamically consistent model for any dissipative material may be constructed through the definition of a finite number of internal variables, which reflect the irreversible processes the material undergoes under external loads. In this regard, one of the principal differences between h-MREs and s-MREs is the underlying magnetic dissipation of the filler particles (e.g. NdFeB) in the former. Due to the finite strains and the magneto-mechanical coupling, upon cyclic magnetic loading, the response of the h-MRE composite exhibits both magnetic and mechanical (due to magneto-mechanical coupling) hysteresis.

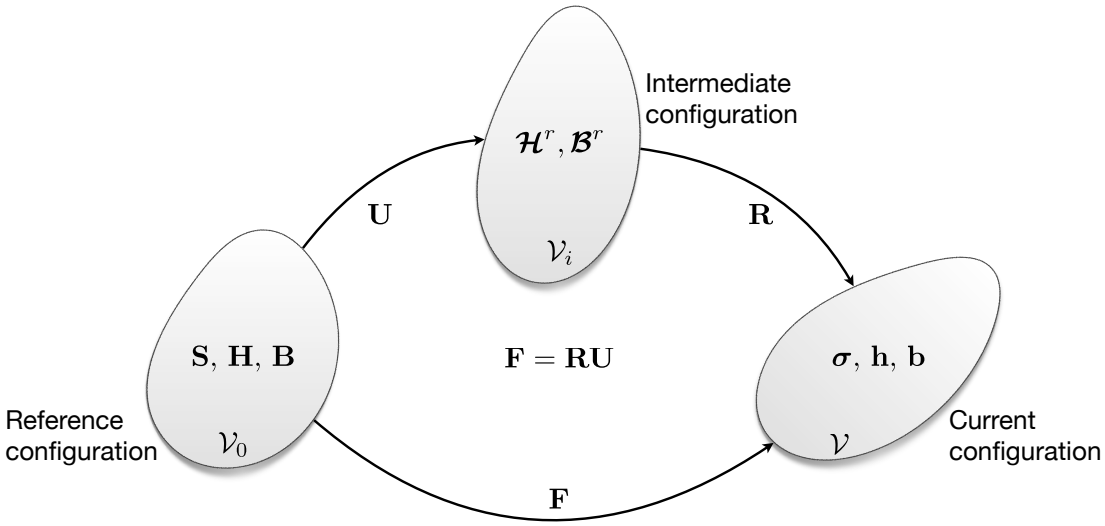

Figure 2: Definition of the reference, intermediate and current configurations of volume $\mathcal{V}_0$, $\mathcal{V}_i$ and $\mathcal{V}$, respectively, along with the different field variables defined therein.

In the work of Mukherjee et al. (2021), it was shown via extensive assessment with numerical RVE simulations that only one internal *magnetic* vectorial variable suffices to describe both the magnetic and the mechanical (due to coupling) dissipation in the h-MRE in the case of moderately

soft to hard polymer matrices. This is a mere *constitutive choice* and does not constitute a unique way to address this coupled dissipative effect[4].

Specifically, we consider that the internal variable is a vector,

$$\boldsymbol{\xi} \equiv \boldsymbol{\mathcal{H}}^r \in \mathbb{R}^3, \tag{45}$$

which lies in the *stretch-free*, *intermediate* configuration $\mathcal{V}_i$, as shown in Fig. 2. This internal variable is a remanent H-like vectorial quantity that will be shown in practice to be strongly linked to the magnetization of the MRE. The central assumption behind this "choice" is that the average magnetization of the composite and thus magnetic dissipation is affected by macroscopic rotations of the magnetization but is independent of macroscopic stretches in the specific case of *incompressible* MREs. A more detailed discussion of the consequences of this assumption will be carried out in Section 7 in parallel with the presentation of specific results.

The range of validity of this assumption depends mainly on the shear modulus of the matrix phase, given that the particles are almost mechanically rigid and thus do not deform but may rotate, whereas the bulk modulus of the matrix phase is very large giving rise to a quasi-incompressible macroscopic response of the h-MRE. In fact, the shear modulus of the matrix controls the capability of the magnetized particles to rotate upon application of a magnetic load that is non-aligned with their magnetization vector. In a soft polymeric matrix, the particles rotate mechanically but also evolve their magnetic state via dissipative mechanisms (such as domain wall motions) in order to align their magnetization with the externally applied magnetic field (Kalina et al., 2017). The softer the matrix the more the rotations prevail over the magnetic dissipation mechanisms. By contrast, when the shear modulus of the matrix has a moderate value (e.g. greater than $\sim 100\,\mathrm{kPa}$), local particle rotations are much less pronounced (provided that the particles are not very elongated either) and dissipative processes dominate the response of the h-MRE, while any rotations of the magnetized particles follow approximately the overall macroscopic rotation. This last case corresponds well to actual, fabricated h-MREs in the literature (see for instance Zhao et al. (2019), Ren et al. (2019), Garcia-Gonzalez et al. (2023)).

In view of this discussion, use of the standard polar decomposition $\mathbf{F} = \mathbf{RU}$ directly implies that the reference (in $\mathcal{V}_0$) and current (in $\mathcal{V}$) remanent fields, $\mathbf{H}^r$ and $\mathbf{h}^r$, respectively are functions of $\boldsymbol{\mathcal{H}}^r$ and are given by

$$\mathbf{h}^r = \mathbf{R}\boldsymbol{\mathcal{H}}^r, \qquad \mathbf{H}^r = \mathbf{U}\boldsymbol{\mathcal{H}}^r. \tag{46}$$

whereby the following standard decompositions also hold (Mukherjee and Danas, 2019)

$$\mathbf{h} = \mathbf{h}^e + \mathbf{h}^r, \qquad \mathbf{H} = \mathbf{H}^e + \mathbf{H}^r. \tag{47}$$

Here, $\mathbf{h}$ and $\mathbf{h}^e$ are the Eulerian total and energetic h-fields, while $\mathbf{H}$ and $\mathbf{H}^e$ are the corresponding Lagrangian ones. The introduction of $\boldsymbol{\mathcal{H}}^r$ in the *intermediate* configuration $\mathcal{V}_i$ further implies that the Eulerian $\mathbf{h}^r$ is stretch-free function of $\mathbf{R}$ and $\boldsymbol{\mathcal{H}}^r$, while the Lagrangian $\mathbf{H}^r$ is a function of $\mathbf{U}$ and $\boldsymbol{\mathcal{H}}^r$.

Obviously, the propositions (46) remain open to further refinements if required by the problem at hand. Nonetheless, we will show in the results presented in Section 7 that the single internal

[4]Works by McMeeking and Landis (2005); McMeeking et al. (2007); Rosato and Miehe (2014) in the context of ferroelectricity, a somewhat similar problem, use both mechanical and polarization internal variables that are eventually related via additional constitutive relations.

variable $\boldsymbol{\mathcal{H}}^r$ is sufficient to achieve very good agreement with the corresponding numerical periodic cell simulations under a wide range of cyclic and non-aligned loading conditions. Addition of compressibility in the matrix is expected to change this feature and in that case extensions of the aforementioned choices shall be necessary. Finally, with this observation, the standard materials relations (33) and (42) are also defined in $\mathcal{V}_i$ instead of $\mathcal{V}_0$. In this view, the conjugate variable to $\boldsymbol{\mathcal{H}}^r$ will be denoted for consistency with $\boldsymbol{\mathcal{B}}^r$ and is fairly similar to the backstress in purely mechanical elasto-plastic systems. The relevant GSM relations (33) and and (42) then become

$$\frac{\partial W^{\mathtt{G}}}{\partial \boldsymbol{\mathcal{H}}^r} + \frac{\partial D}{\partial \dot{\boldsymbol{\mathcal{H}}}^r} = \mathbf{0} \text{ for all } \mathbf{X} \in \mathcal{V}_0, \quad \text{with} \quad \boldsymbol{\mathcal{B}}^r = \frac{\partial D}{\partial \dot{\boldsymbol{\mathcal{H}}}^r} = -\frac{\partial W^{\mathtt{G}}}{\partial \boldsymbol{\mathcal{H}}^r}, \tag{48}$$

where again $\mathbf{G} = \{\mathbf{H}, \mathbf{B}\}$ has been introduced in (44).

Remark 6. The recent work of Mukherjee and Danas (2022) denotes the internal variable by $\boldsymbol{\xi} \equiv \boldsymbol{\mathcal{H}}^r$. Given the fact that the dissipation potential D is identical in both the $\mathbf{F}-\mathbf{H}$ and the $\mathbf{F}-\mathbf{B}$ formulations, a choice of a neutral notation was done there to avoid confusion. Nonetheless, we maintain in this manuscript the original $\boldsymbol{\mathcal{H}}^r$ one, since in future works $\boldsymbol{\xi}$ may be used to denote additional internal variables as is the case of viscoelasticity (Rambausek et al., 2022; Lucarini et al., 2022a).

4.2. General properties of the free energy density and the dissipation potential

We recall first that material objectivity and symmetry conditions are well-known for s-MREs (Kankanala and Triantafyllidis, 2004; Dorfmann and Ogden, 2004). However, as shown in Fig. 2, the present models for h-MREs introduce a remanent internal variable that is insensitive to the stretch $\mathbf{U}$, leading to non-familiar magneto-mechanical invariants and rates. Hence, this section focuses on stating explicitly all the aforementioned constraints in the context of isotropic h-MREs. The proposed invariants may then be simplified to attain those that remain also valid for s-MREs.

Even magneto-mechanical coupling. The magneto-mechanical energy density $W^{\mathtt{G}}$ and dissipation potential D must be exactly the same when both $\mathbf{G}$ and $\boldsymbol{\mathcal{H}}^r$ change simultaneously sign. This condition reads

$$W^{\mathtt{G}}(\mathbb{C}, -\mathbf{G}, -\boldsymbol{\mathcal{H}}^r) = W^{\mathtt{G}}(\mathbb{C}, \mathbf{G}, \boldsymbol{\mathcal{H}}^r), \qquad D(-\dot{\boldsymbol{\mathcal{H}}}^r) = D(\dot{\boldsymbol{\mathcal{H}}}^r), \tag{49}$$

and ensures a symmetric, butterfly-type magnetostriction response for the h-MRE, as will be discussed in the results Section 7.

Material frame indifference. This physical property imposes that W and D must remain invariant under a change of observer. A change of observer leads to the new current position vector $\mathbf{x}^* = \mathbf{c} + \mathbf{Q}\mathbf{x}$, where $\mathbf{c}$ is a rigid displacement field and $\mathbf{Q}$ is a proper rotation matrix (Gurtin, 1982, p. 139-142). Since the arguments of $W^{\mathtt{G}}$ and D, i.e. $\mathbb{C}, \mathbf{G}, \boldsymbol{\mathcal{H}}^r$ and $\dot{\boldsymbol{\mathcal{H}}}^r$ are unaffected by such a transform, the requirement of material frame indifference imposes no further restrictions on $W^{\mathtt{G}}$ and D. This observation is in agreement with the objectivity conditions used in mechanical viscoplasticity, where the intermediate strain-like variables remain unaffected by a change of observer (Dashner, 1993; Kumar and Lopez-Pamies, 2016).

Material symmetry. For isotropic MREs, $W^{\mathtt{G}}$ and D must remain invariant under a change in the reference configuration via a constant matrix $\mathbf{K} \in Orth^+$. The material symmetry conditions on the potentials thus read

$$\begin{aligned} &W^{\mathtt{G}}(\mathbf{K}^T\mathbb{C}\mathbf{K}, \mathbf{K}^T\mathbf{G}, \mathbf{K}^T\boldsymbol{\mathcal{H}}^r) = W(\mathbb{C}, \mathbf{G}, \boldsymbol{\mathcal{H}}^r), \\ &D(\mathbf{K}^T\dot{\boldsymbol{\mathcal{H}}}^r; \mathbf{K}^T\mathbb{C}\mathbf{K}, \mathbf{K}^T\mathbf{G}, \mathbf{K}^T\boldsymbol{\mathcal{H}}^r) = D(\dot{\boldsymbol{\mathcal{H}}}^r; \mathbb{C}, \mathbf{G}, \boldsymbol{\mathcal{H}}^r). \end{aligned} \tag{50}$$

Here, we note that the intermediate $\boldsymbol{\mathcal{H}}^r$ transforms as $\boldsymbol{\mathcal{H}}^r \to \mathbf{K}^T\boldsymbol{\mathcal{H}}^r$, which follows from (46) and the transformation $\mathbf{U} \to \mathbf{K}^T\mathbf{U}\mathbf{K}$ under a change in the reference configuration. We further remark that in mechanical visco-plasticity the change in the reference configuration also modifies the intermediate plastic internal variables (Dashner, 1993; Bennett et al., 2016).

4.3. The isotropic magneto-mechanical invariants for h-MREs

A straightforward and elegant way to satisfy the conditions of even magneto-mechanical coupling, isotropic material symmetry and frame indifference is to express the energy density and dissipation in terms of properly chosen *isotropic* invariants. First, we define the general set of available invariants given the corresponding arguments $\mathbb{C}$, $\mathbf{G}$ and $\boldsymbol{\mathcal{H}}^r$. Subsequently, a reduced number of them will be chosen to model the h-MREs. The choice is mainly motivated by corresponding numerical RVE simulations of two-phase h-MRE composites and does not constitute a rigorous result but merely an efficient homogenization-guided strategy that allows to maintain the number of invariants small and the model entirely explicit.

Mechanical invariants.

$$I_1 = \mathrm{tr}(\mathbb{C}), \qquad I_2 = \mathrm{tr}(\mathbb{C})^2 - \mathrm{tr}(\mathbb{C}^2), \qquad I_3 = J^2 = \det\mathbb{C} = 1, \tag{51}$$

Magneto-mechanical invariants in $\mathbf{F}-\mathbf{H}$ *formulation.*

$$\begin{aligned}
&I_4^{\mathtt{H}} = \mathbf{H}\cdot\mathbf{H}, && I_4^{\mathtt{HHr}} = \mathbf{H}\cdot\mathbb{C}^{1/2}\boldsymbol{\mathcal{H}}^r, && I_4^{\mathtt{Hr}} = \boldsymbol{\mathcal{H}}^r\cdot\mathbb{C}\boldsymbol{\mathcal{H}}^r\\
&I_5^{\mathtt{H}} = \mathbf{H}\cdot\mathbb{C}^{-1}\mathbf{H}, && I_5^{\mathtt{HHr}} = \mathbf{H}\cdot\mathbb{C}^{-1/2}\boldsymbol{\mathcal{H}}^r, && I_5^{\mathtt{Hr}} = \boldsymbol{\mathcal{H}}^r\cdot\boldsymbol{\mathcal{H}}^r.\\
&I_6^{\mathtt{H}} = \mathbf{H}\cdot\mathbb{C}\mathbf{H}, && I_6^{\mathtt{HHr}} = \mathbf{H}\cdot\mathbb{C}^{3/2}\boldsymbol{\mathcal{H}}^r, && I_6^{\mathtt{Hr}} = \boldsymbol{\mathcal{H}}^r\cdot\mathbb{C}^2\boldsymbol{\mathcal{H}}^r.
\end{aligned} \tag{52}$$

Magneto-mechanical invariants in $\mathbf{F}-\mathbf{B}$ *formulation.*

$$\begin{aligned}
&I_4^{\mathtt{B}} = \mathbf{B}\cdot\mathbf{B}, && I_4^{\mathtt{BHr}} = \mathbf{B}\cdot\mathbb{C}^{-1/2}\boldsymbol{\mathcal{H}}^r, && I_4^{\mathtt{Hr}} = \boldsymbol{\mathcal{H}}^r\cdot\mathbb{C}\boldsymbol{\mathcal{H}}^r\\
&I_5^{\mathtt{B}} = \mathbf{B}\cdot\mathbb{C}\mathbf{B}, && I_5^{\mathtt{BHr}} = \mathbf{B}\cdot\mathbb{C}^{1/2}\boldsymbol{\mathcal{H}}^r, && I_5^{\mathtt{Hr}} = \boldsymbol{\mathcal{H}}^r\cdot\boldsymbol{\mathcal{H}}^r.\\
&I_6^{\mathtt{B}} = \mathbf{B}\cdot\mathbb{C}^2\mathbf{B}, && I_6^{\mathtt{BHr}} = \mathbf{B}\cdot\mathbb{C}^{3/2}\boldsymbol{\mathcal{H}}^r && I_6^{\mathtt{Hr}} = \boldsymbol{\mathcal{H}}^r\cdot\mathbb{C}^2\boldsymbol{\mathcal{H}}^r.
\end{aligned} \tag{53}$$

The energetic invariants, i.e., those that do not involve $\boldsymbol{\mathcal{H}}^r$, are the standard ones employed usually in the context of s-MREs (Kankanala and Triantafyllidis, 2004; Ponte Castañeda and Galipeau, 2011; Danas et al., 2012; Danas, 2017; Mukherjee et al., 2020). The remaining invariants are mixed or purely remanent ones, and are necessary in the modeling of h-MREs. We note here that the use of the rational exponents in the mixed invariants are chosen in order to allow the proper amplitude of coupling. Moreover, it is emphasized that $\boldsymbol{\mathcal{H}}^r$ has the same units as the h-field and thus proper addition of μ_0 is required in the final energy expressions. Finally, in order to satisfy the invariance of the dissipation potential, we additionally employ the Euclidean norm $|\dot{\boldsymbol{\mathcal{H}}}^r| = \sqrt{\dot{\boldsymbol{\mathcal{H}}}^r\cdot\dot{\boldsymbol{\mathcal{H}}}^r}$ as an invariant of $\dot{\boldsymbol{\mathcal{H}}}^r$.

We further note that the "uncoupled" I_5-type invariants are unaffected by mechanical deformation when a certain Eulerian magnetic field is independently controlled whereas the I_4 do vary in this case (see relevant discussion in Danas (2017)).

4.4. Form of energy densities

We now express the energy densities associated with an incompressible h-MRE in terms of these invariants. In particular, both $W^{\mathtt{H}}$ and $W^{\mathtt{B}}$ are considered to be the sum of three distinct energy densities, namely, the purely mechanical, purely magnetic and coupling free energy density, such that

$$W^{\mathtt{H}}(\mathbb{C},\mathbf{H},\boldsymbol{\mathcal{H}}^r) = \rho_0\Psi_{\mathtt{mech}}(I_1) + \rho_0\Psi^{\mathtt{H}}_{\mathtt{mag}}(I^{\mathtt{H}}_5, I^{\mathtt{HHr}}_5, I^{\mathtt{Hr}}_5) + \\ + \rho_0\Psi^{\mathtt{H}}_{\mathtt{couple}}(I^{\mathtt{HHr}}_4, I^{\mathtt{Hr}}_4, I^{\mathtt{HHr}}_5, I^{\mathtt{Hr}}_5) - \frac{\mu_0}{2}I^{\mathtt{H}}_5 \tag{54}$$

and

$$W^{\mathtt{B}}(\mathbb{C},\mathbf{B},\boldsymbol{\mathcal{H}}^r) = \rho_0\Psi_{\mathtt{mech}}(I_1) + \rho_0\Psi^{\mathtt{B}}_{\mathtt{mag}}(I^{\mathtt{B}}_5, I^{\mathtt{BHr}}_5, I^{\mathtt{Hr}}_5) \\ + \rho_0\Psi^{\mathtt{B}}_{\mathtt{couple}}(I^{\mathtt{Hr}}_4, I^{\mathtt{BHr}}_5, I^{\mathtt{Hr}}_5, I^{\mathtt{BHr}}_6, I^{\mathtt{Hr}}_6) + \frac{1}{2\mu_0}I^{\mathtt{B}}_5. \tag{55}$$

We will show later in this section that $W^{\mathtt{B}}$ is an exact dual of $W^{\mathtt{H}}$ in the sense defined in $(36)_2$. For this to be possible, one should have fairly simple expressions that allow for an analytical Legendre-Fenchel transform. That will be the case here but it is not always possible, as we will show in the case of purely energetic s-MREs in Section 5.

In both expressions, ρ_0 is the reference density of the solid, while the last terms $\mu_0 I^{\mathtt{H}}_5/2$ in (54) and $I^{\mathtt{B}}_5/2\mu_0$ in (55) represent the energy associated with free space with μ_0 being the magnetic permeability in vacuum or in non-magnetic solids such as the polymer matrix phase.

Remark 7. In absence of any magnetic material, $\Psi^{\mathtt{G}}_{\mathtt{mag}} = \Psi^{\mathtt{G}}_{\mathtt{couple}} = 0$, however the energy density $W^{\mathtt{H}}$ or $W^{\mathtt{B}}$ does not vanish. Instead the presence of the last term in (54) or (55) allows the magnetic fields to exist in the vacuum or in non-magnetic materials, such as the matrix phase. These terms are in general necessary even if one works with a magnetization based formulation. In formulations that these terms are omitted, the effect of the surrounding space or neighboring non-magnetic materials are in general not taken into account. This, however, is primordial in the present case of the modeling of particle-filled MREs, since these terms allow to retain the long-range interactions between the particles. Such interactions in nonlinear materials are in general non-trivial and cannot be fully described by simpler particle-particle (nearest neighbors) dipole-bases models.

The introduction of such an incompressible material model necessitates the modification of the constitutive relations $(31)_2$ and $(40)_2$ for the total stress $\mathbf{S}$, such that

$$\mathbf{S} = 2\mathbf{F}\frac{\partial W^{\mathtt{G}}}{\partial \mathbb{C}} + p\mathbf{F}^{-T}, \tag{56}$$

where the superscript $\mathtt{G}$ refers the notation introduced in (44) and p is the Lagrange multiplier associated with the incompressibility constraint $J = 1$. In practice, p adds on to the local (point wise) number of unknowns to be solved after optimization of the variational principle.

Remark 8. We note that the *quasi-incompressible* equivalents of the proposed incompressible models are often useful in the numerical computations. Thus, we extend the proposed $\mathbf{F}-\mathbf{H}$ and $\mathbf{F}-\mathbf{B}$-based MRE models in a rather ad-hoc way so that the energy densities read

$$W^{\mathtt{H}}_{\mathtt{comp}}(\mathbb{C},\mathbf{H},\boldsymbol{\mathcal{H}}^r) = \rho_0\Psi^{\mathtt{comp}}_{\mathtt{mech}}(I_1, J) + \rho_0\Psi^{\mathtt{H}}_{\mathtt{mag}}(I^{\mathtt{H}}_5, I^{\mathtt{HHr}}_5, I^{\mathtt{Hr}}_5) \\ + \rho_0\Psi^{\mathtt{H}}_{\mathtt{couple}}(I^{\mathtt{HHr}}_4, I^{\mathtt{Hr}}_4, I^{\mathtt{HHr}}_5, I^{\mathtt{Hr}}_5) - \frac{\mu_0}{2}JI^{\mathtt{H}}_5 \tag{57}$$

and

$$W^{\mathtt{B}}_{\mathtt{comp}}(\mathbb{C},\mathbf{H},\boldsymbol{\mathcal{H}}^r)=\rho_0\Psi^{\mathtt{comp}}_{\mathtt{mech}}(I_1,J)+\rho_0\Psi^{\mathtt{B}}_{\mathtt{mag}}(I^{\mathtt{B}}_5,I^{\mathtt{BHr}}_5,I^{\mathtt{Hr}}_5)$$
$$+\rho_0\Psi^{\mathtt{B}}_{\mathtt{couple}}(I^{\mathtt{Hr}}_4,I^{\mathtt{BHr}}_5,I^{\mathtt{Hr}}_5,I^{\mathtt{BHr}}_6)+\frac{I^{\mathtt{B}}_5}{2\mu_0 J}, \tag{58}$$

respectively. Note that the proposed quasi-incompressible energy functions *are not meant to be used* for compressible MREs, since the proposed expressions do not take into account any coupling between volumetric deformations and magnetic fields. Such coupling requires an entirely independent analysis (Gebhart and Wallmersperger, 2022a,b) and more importantly should reflect a realizable compressible MRE. Currently, most MREs existing in literature are fairly incompressible except earlier and more recent studies on MRE foams (Diguet et al., 2021). Nonetheless, in those cases, taking into account the precise microstructure is of essence. Such studies are in progress and will be presented elsewhere in the future.

4.5. The mechanical energy density

The purely mechanical free energy density $\rho_0\Psi_{\mathtt{mech}}$ is the same for both formulations and corresponds to the analytical homogenization estimate by Lopez-Pamies et al. (2013) for a two-phase composite made of an incompressible nonlinear elastic matrix comprising isotropic distributions of rigid-particles, such that

$$\Psi_{\mathtt{mech}}(I_1;c)=(1-c)\Psi_{\mathtt{m,mech}}(\mathcal{I}_1),\qquad \mathcal{I}_1=\frac{I_1-3}{(1-c)^{7/2}}+3, \tag{59}$$

where c is the particle volume fraction and $\Psi_{\mathtt{m,mech}}$ is the free energy density of the matrix. Notably, the homogenization estimate (59) holds for any I_1-based incompressible rigid-particle–matrix composite. Thus, the choice for the matrix constitutive law remains versatile in the present modeling framework. Evidently, in the limit of $c=0$, the homogenized energy recovers that of the matrix phase, i.e., $\Psi_{\mathtt{mech}}(I_1,0)=\Psi_{\mathtt{m,mech}}(I_1)$. By contrast, $\Psi_{\mathtt{mech}}(I_1,1)=+\infty$ when $c=1$, hence, recovering the energy of a rigid material. This part may be replaced readily by any other mechanical estimate, homogenization-based or phenomenological, that may be required.

An ad-hoc modification of the above incompressible energy allows to obtain a quasi-incompressible counterpart that proves useful in numerical computations. In particular, the term $\Psi^{\mathtt{comp}}_{\mathtt{mech}}(I_1,J)$ in (57) and (58), may be written as

$$\rho_0\Psi^{\mathtt{comp}}_{\mathtt{mech}}(I_1,J)=(1-c)\rho_0\Psi_{\mathtt{m,mech}}(\mathcal{I}^{\mathtt{comp}}_1)+\frac{G'_{\mathtt{m}}}{2(1-c)^6}(J-1)^2,$$
$$\text{with}\qquad \mathcal{I}^{\mathtt{comp}}_1=\frac{I_1-3-2\ln J}{(1-c)^{7/2}}+3. \tag{60}$$

In this expression, we typically set the Lamé parameter $G'_{\mathtt{m}}\geq 200G_{\mathtt{m}}$, which ensures a quasi-incompressible response with $J\approx 1$.

4.6. The magnetic and coupled energy densities

Next, the magnetic and coupling free energy functions along with the dissipation potential are proposed. Special care is taken in proposing these functions so that the magnetization response yields several limiting cases, especially, in the limit of small primary and remanent magnetic fields. In the following, we provide these functions without elaborating on their individual significance.

Table 1: Inverse saturation function choices for the remanent potential

Function name	$f_{\mathtt{p}}(x)$
Inverse hypergeometric function	$-[\log(1-x)+x]$
Tangent function	$-\frac{4}{\pi^2}\log\left[\cos\left(\frac{\pi}{2}x\right)\right]$
Arctanh function	$-\left[(1-x)\tanh^{-1}(x)-\log(x+1)\right]$
Inverse Langevin function (approx.)	$\frac{1}{3}\Big(-\frac{x^3}{3}+x^2-\big(0.0571x^2-0.0093\big)\cos(3.5x)$ $-x-\log(1-x)+0.0327x\sin(3.5x)-0.0093\Big)$

4.6.1. F-H expressions for h-MREs.

The pure magnetic free energy is expressed in terms of the I_5-based invariants, so that

$$\rho_0\Psi^{\mathtt{H}}_{\mathtt{mag}}(I_5^{\mathtt{H}},I_5^{\mathtt{HHr}},I_5^{\mathtt{Hr}}) = -\frac{\mu_0}{2}\chi^e I_5^{\mathtt{H}}+\mu_0(1+\chi^e)I_5^{\mathtt{HHr}}+\frac{\mu_0}{2}\left(\frac{1-c}{3c}\right)I_5^{\mathtt{Hr}} + \frac{\mu_0}{c}\frac{(m^s)^2}{\chi^r_{\mathtt{p}}}f_{\mathtt{p}}\left(\frac{\sqrt{I_5^{\mathtt{Hr}}}}{m^s}\right). \tag{61}$$

Here $\chi^r_{\mathtt{p}}$ is the *remanent susceptibility* of the underlying magnetic particle, whereas the "effective" parameters χ^e and m^s for the composite are given in terms of the particle magnetic properties and its volume fraction c as

$$\chi^e=\frac{3c\chi^e_{\mathtt{p}}}{3+(1-c)\chi^e_{\mathtt{p}}}, \qquad m^s = c\, m^s_{\mathtt{p}}\left(\frac{1+\chi^e_{\mathtt{p}}}{1+\chi^e}\right), \tag{62}$$

where $\chi^e_{\mathtt{p}}$ and $m^s_{\mathtt{p}}$ are the particle *energetic susceptibility* and *saturation magnetization* (a graphic explanation of these parameters is provided later in the context of Fig. 3). Moreover, $f_{\mathtt{p}}(x)$ is a nonlinear function that leads to a saturation-type magnetization behavior. Additionally, $f_{\mathtt{p}}(x)$ must satisfy the properties such that (`i`) it is smooth and at least twice differentiable for all $0\le x<1$, (`ii`) $f'_{\mathtt{p}}(x)$ leading to an inverse saturation (sigmoid) function that tends to $+\infty$ in the limit of $x\to 1$ and (`iii`) the leading order Taylor series expansion of $f_{\mathtt{p}}(x)$ around $x=0$ goes as x^2. Of course, the specific choices for $f_{\mathtt{p}}(x)$ depends on the saturation response of the (hard/soft) magnetic particles. A set of representative choices for such hard magnetic particles are provided in Table 1.

Finally, the coupling free energy $\Psi^{\mathtt{H}}_{\mathtt{couple}}$ is proposed in terms of both, the I_4 and I_5-based invariants as defined in (52), so that

$$\rho_0\Psi^{\mathtt{H}}_{\mathtt{couple}}(I_4^{\mathtt{HHr}},I_4^{\mathtt{Hr}},I_5^{\mathtt{HHr}},I_5^{\mathtt{Hr}}) = c\,\beta(c)\mu_0\Big[\big(I_4^{\mathtt{Hr}}-I_5^{\mathtt{Hr}}\big)-2\chi^e\big(I_4^{\mathtt{HHr}}-I_5^{\mathtt{HHr}}\big)\Big] \tag{63}$$

with

$$\beta(c)=19.0c^2-10.4c+1.71. \tag{64}$$

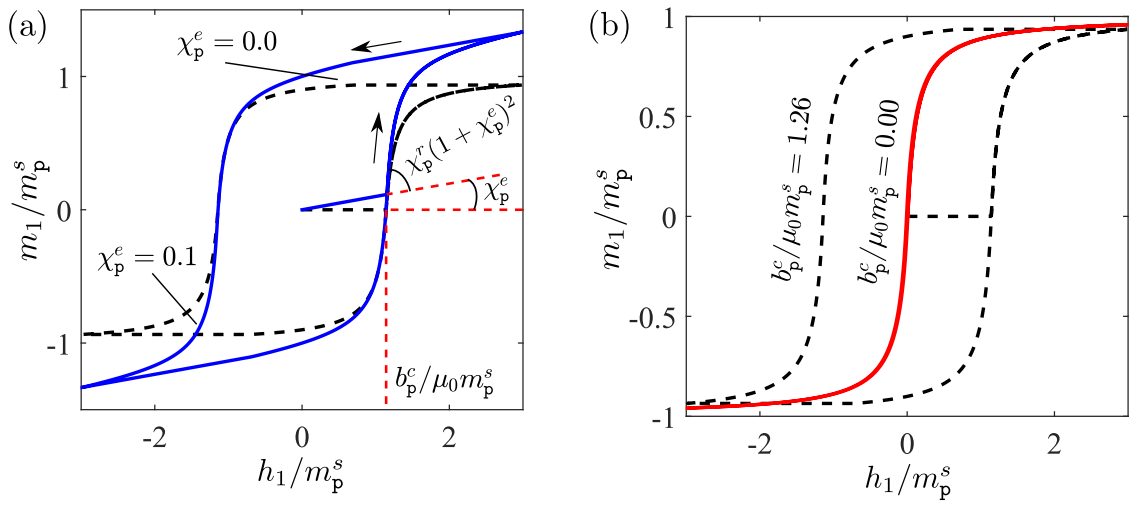

Figure 3: (a) Magnetization response under applied uniaxial cyclic h-field $\mathbf{h} = h_1\mathbf{e}_1$. Both, ideal ($\chi^e_{\rm p} = 0$) and actual ($\chi^e_{\rm p} > 0$) hysteresis loops are shown along with the slopes of the $m-h$ response before and after switching. (b) Magnetization responses for finite and zero coercivity leading to, respectively, hysteretic and energetic magnetization responses. (Taken partly from Mukherjee and Danas (2022)).

Notice that the I_4-type "coupling" invariants only appear in the coupling free energy $\Psi^{\mathtt{H}}_{\mathtt{couple}}$, whereas, the purely magnetic free energy (61) is only a function of the "pure magnetic" or "decoupled" I_5-type invariants. Moreover, the coupling parameter $\beta(c)$ in (63) may be further calibrated against experimental data or numerical homogenization estimates. In this study, we will use the expression (64) as obtained by direct calibration with corresponding FE simulations in Section 7.1, and thus it is valid for $c \leq 0.3$. We also note the simple linear dependence on the invariants of the coupled energy density in (63). This will prove extremely useful in obtaining a dual energy density for the $\mathbf{F}-\mathbf{B}$ model in the following.

4.6.2. F-B expressions for h-MREs.

The proposed $W^{\mathtt{H}}$ in (54) along with the invariants in (52) lead to a *strictly concave* energy density function in terms of $\mathbf{H}$, i.e., for a given $\mathbb{C}$ and $\boldsymbol{\mathcal{H}}^r$, $W^{\mathtt{H}}$ is a strictly concave function of $\mathbf{H}$. Note that the remaining invariants are functions of the internal variable $\boldsymbol{\mathcal{H}}^r$, which remain exactly the same for the dual $\mathbf{F}-\mathbf{B}$ version we describe here. Consequently, in order to obtain the equivalent, dual $\mathbf{F}-\mathbf{B}$ energy density, we seek for a closed form partial Legendre-Fenchel transform of $W^{\mathtt{H}}$ following $(36)_2$. Straightforward algebraic manipulations lead to the expression for $W^{\mathtt{B}}$ in (55).

More specifically, the mechanical free energy $\Psi_{\mathtt{mech}}$ in (55) remains identical to (59), whereas the transformed magnetic free energy $\Psi^{\mathtt{B}}_{\mathtt{mag}}(I^{\mathtt{B}}_5, I^{\mathtt{BHr}}_5, I^{\mathtt{Hr}}_5)$ becomes

$$\rho_0\Psi^{\mathtt{B}}_{\mathtt{mag}}(I^{\mathtt{B}}_5, I^{\mathtt{BHr}}_5, I^{\mathtt{Hr}}_5) = -\frac{1}{2\mu_0}\frac{\chi^e}{1+\chi^e}I^{\mathtt{B}}_5 + I^{\mathtt{BHr}}_5 + \frac{\mu_0}{2}\left(\chi^e + \frac{1+2c}{3c}\right)I^{\mathtt{Hr}}_5 + \frac{\mu_0}{c}\frac{(m^s)^2}{\chi^r_{\rm p}} f_{\rm p}\left(\frac{\sqrt{I^{\mathtt{Hr}}_5}}{m^s}\right), \tag{65}$$

where all the model parameters along with the function $f_{\mathtt{p}}(x)$ remain identical to their respective definitions for the $\mathbf{F}-\mathbf{H}$ model presented earlier. Finally, the coupling free energy reads

$$\rho_0\Psi^{\mathtt{B}}_{\mathtt{couple}}(I_4^{\mathtt{Hr}}, I_5^{\mathtt{BHr}}, I_5^{\mathtt{Hr}}, I_6^{\mathtt{BHr}}, I_6^{\mathtt{Hr}}) = c\beta\mu_0(1-2\chi^e)\Big\{I_4^{\mathtt{Hr}} - I_5^{\mathtt{Hr}}\Big\}$$
$$-\frac{2c\beta\chi^e}{1+\chi^e}\Big\{I_6^{\mathtt{BHr}} - I_5^{\mathtt{BHr}}\Big\} + 2\mu_0\frac{(c\beta\chi^e)^2}{1+\chi^e}\Big\{I_5^{\mathtt{Hr}} + I_6^{\mathtt{Hr}} - 2I_4^{\mathtt{Hr}}\Big\}. \tag{66}$$

Notice further that the particle volume fraction remains limited to $c \leq 0.3$ in all practical applications of h-MREs (Zhao et al., 2019; Alapan et al., 2020). Consequently, we obtain $0 < \chi^e \ll 1$ for the h-MREs comprising NdFeB particles. Thus, the last term in the expression for $\rho_0\Psi^{\mathtt{B}}_{\mathtt{couple}}$ in (66) turns out to be substantially smaller than the preceding ones and hence, can be dropped for all practical modeling purposes. Consequently, the coupling energy in the proposed $\mathbf{F}-\mathbf{B}$ model simplifies to

$$\rho_0\Psi^{\mathtt{B}}_{\mathtt{couple}}(I_4^{\mathtt{Hr}}, I_5^{\mathtt{BHr}}, I_5^{\mathtt{Hr}}, I_6^{\mathtt{BHr}}) =$$
$$c\beta\bigg[\mu_0(1-2\chi^e)\Big\{I_4^{\mathtt{Hr}} - I_5^{\mathtt{Hr}}\Big\} - \frac{2\chi^e}{1+\chi^e}\Big\{I_6^{\mathtt{BHr}} - I_5^{\mathtt{BHr}}\Big\}\bigg]. \tag{67}$$

With this, the definition of the $\mathbf{F}-\mathbf{B}$ based energy density becomes complete. Being the closed-form Legendre-Fenchel transform of the $\mathbf{F}-\mathbf{H}$ model, the derived $\mathbf{F}-\mathbf{B}$ model exhibits the *exact* same features as the corresponding $\mathbf{F}-\mathbf{H}$ model discussed previously. Consequently, no further calibration of $\beta(c)$ parameter, defined in (64), is needed in (67). Specific comparisons between the local responses of the $\mathbf{F}-\mathbf{H}$ and $\mathbf{F}-\mathbf{B}$ models will be shown later in Section 7.1.

4.7. The dissipation potential

It remains to define the dissipation potential D, which along with $W^{\mathtt{H}}$ and $W^{\mathtt{B}}$ completes the model constitutive relations. Given that we do not include viscoelastic effects in the present manuscript, we propose the rate-dependent dissipation potential to be a simple power law in terms of $\dot{\boldsymbol{\mathcal{H}}}^r$ only, such that (Mukherjee and Danas, 2019)

$$D(\dot{\boldsymbol{\mathcal{H}}}^r) = \frac{n\ b^c}{n+1}|\dot{\boldsymbol{\mathcal{H}}}^r|^{\frac{n+1}{n}}, \qquad \text{with} \quad 1 \leq n < +\infty. \tag{68}$$

Here, $|.|$ is the standard Eulerian norm and b^c is the effective *coercive field* of the composite (see graphical representation in Fig. 3) that is given in terms of the particle and effective energetic susceptibility via

$$b^c = b^c_{\mathtt{p}}\left(\frac{1+\chi^e}{1+\chi^e_{\mathtt{p}}}\right)^{4/5}. \tag{69}$$

Here, $b^c_{\mathtt{p}}$ is the particle ceorcivity. Typically, for a hard-magnetic composite the effective coercivity is given by $b^c = b^c_{\mathtt{p}}$ (Idiart et al., 2006b). Nonetheless, the term multiplying $b^c_{\mathtt{p}}$ in (69) essentially serves as a correction term for an actual magnet, whose saturation magnetization slope is *not* identically zero.

The dissipation potential $D(\dot{\boldsymbol{\mathcal{H}}}^r)$ in (68) is strictly convex (except for $n = +\infty$ that becomes simply convex), hence, satisfies automatically the dissipation inequality constraint. Moreover, the rate $|\dot{\boldsymbol{\mathcal{H}}}^r| = \sqrt{\dot{\boldsymbol{\mathcal{H}}}^r \cdot \dot{\boldsymbol{\mathcal{H}}}^r}$ satisfies the material frame indifference and material symmetry conditions.

By observing the experimental data on magnetic materials, we focus next on *rate-independent* ferromagnetic hysteresis responses. Thus, we consider the limiting case $n = +\infty$ at which, the dissipation potential (68) becomes $D(\dot{\boldsymbol{\mathcal{H}}}^r) = b^c|\dot{\boldsymbol{\mathcal{H}}}^r|$, whose derivarive with respect to $\dot{\boldsymbol{\mathcal{H}}}^r$ is non-unique at $|\dot{\boldsymbol{\mathcal{H}}}^r| = 0$. Hence, we start from the Legendre-Fenchel transform of D, i.e., D^* such that

$$D^*(\boldsymbol{\mathcal{B}}^r) = \inf_{\dot{\boldsymbol{\mathcal{H}}}^r} \left[\boldsymbol{\mathcal{B}}^r \cdot \dot{\boldsymbol{\mathcal{H}}}^r - b^c|\dot{\boldsymbol{\mathcal{H}}}^r|\right] \tag{70}$$

in the rate-independent limit. The minimization condition of the last expression leads to a criterion known as *ferromagnetic switching surface*

$$\Phi(\boldsymbol{\mathcal{B}}^r) := |\boldsymbol{\mathcal{B}}^r|^2 - (b^c)^2 = 0, \tag{71}$$

which must be satisfied during the energy dissipation in a magnetic loading/unloading cycle. With (71), we rephrase the dissipation potential $D(\dot{\boldsymbol{\xi}})$ by introducing a (non-negative) Lagrange multiplier $\dot{\Lambda}$, so that

$$D(\dot{\boldsymbol{\mathcal{H}}}^r) = \sup_{\boldsymbol{\mathcal{B}}^r} \inf_{\dot{\Lambda}\geq 0} \left[\boldsymbol{\mathcal{B}}^r \cdot \dot{\boldsymbol{\mathcal{H}}}^r - \dot{\Lambda}\Phi(\boldsymbol{\mathcal{B}}^r)\right]. \tag{72}$$

In fact, substituting $\boldsymbol{\mathcal{B}}^r = b^c\dot{\boldsymbol{\mathcal{H}}}^r/|\dot{\boldsymbol{\mathcal{H}}}^r|$ (the minimization condition of (70)) yields exactly $D(\dot{\boldsymbol{\mathcal{H}}}^r) = b^c|\dot{\boldsymbol{\mathcal{H}}}^r|$ but now with a constraint (71), which must be satisfied to make the term $\dot{\Lambda}\Phi(\boldsymbol{\mathcal{B}}^r)$ in (72) to vanish.

The constrained dissipation potential in (72) thus needs to be employed in the variational principle (28) to obtain a set of equations necessary to obtain the evolution of $\boldsymbol{\mathcal{B}}^r$. These stationarity conditions of (72) are

$$\dot{\boldsymbol{\mathcal{H}}}^r = \dot{\Lambda}\frac{\partial\Phi}{\partial\boldsymbol{\mathcal{B}}^r}, \qquad \Phi(\boldsymbol{\mathcal{B}}^r) \leq 0, \qquad \dot{\Lambda} \geq 0 \qquad \text{and} \qquad \dot{\Lambda}\Phi = 0, \tag{73}$$

where the latter three is commonly referred to be the Kraush-Kuhn-Tucker (KKT) conditions. With (73), the evolution equation for the internal variable $\boldsymbol{\mathcal{H}}^r$ is now fully defined.

Remark 9. The limiting case of $c = 0$ leads to the energy densities associated with the non-magnetic elastomer for both, $\mathbf{F}-\mathbf{H}$ and $\mathbf{F}-\mathbf{B}$ models. Specifically, the condition $c = 0$ leads to the magnetic free energies (for both the models) so that

$$\rho_0\Psi^{\mathtt{H/B}}_{\mathtt{mag}} = \begin{cases} +\infty & \text{if} \quad \boldsymbol{\mathcal{H}}^r \neq \mathbf{0}, \\ 0 & \text{if} \quad \boldsymbol{\mathcal{H}}^r = \mathbf{0}. \end{cases} \tag{74}$$

This condition essentially constraints $\boldsymbol{\mathcal{H}}^r$ to remain $\mathbf{0}$ for $c = 0$. Thus, the dissipation potential (68) vanishes and the energy densities for the $\mathbf{F}-\mathbf{H}$ and $\mathbf{F}-\mathbf{B}$ models read, respectively, $W^{\mathtt{H}}_{c=0} = \rho_0\Psi_{\mathtt{mech}}(I_1) - (\mu_0/2)I^{\mathtt{H}}_5$ and $W^{\mathtt{B}}_{c=0} = \rho_0\Psi_{\mathtt{mech}}(I_1) + (1/2\mu_0)I^{\mathtt{B}}_5$. The limit of $c \to 1$, on the other hand, leads to the mechanically rigid hard-magnetic particle response, essentially yielding the pure magnetic switching surface model. Note, however, that in this important special case of $c \to 1$, one should replace the mechanical energy in (59) (or (60)) with one that is not infinite but instead with a large modulus in order to allow a numerical resolution of the problem.

4.8. Total Cauchy stress in h-MREs

Although the constitutive model definitions are complete so far, the expression for the total Cauchy stress in terms of the current magnetic and mechanical variables are often sought after to gain more insight to the different stress contributions. Thus, the expressions for $\boldsymbol{\sigma}$ in terms of $\mathbb{B}$, $\mathbf{h}$, $\mathbf{b}$ and $\mathbf{h}^r$, where $\mathbb{B} = \mathbf{F}\mathbf{F}^T$ is the left Cauchy-Green tensor, in the $\mathbf{F}-\mathbf{H}$ and $\mathbf{F}-\mathbf{B}$ settings are provided in the following.

4.8.1. Cauchy stress in the F-H model

We first express $W^{\mathtt{H}}$ in terms of $\mathbf{F}$, $\mathbf{H}$ and $\boldsymbol{\mathcal{H}}^r$ and subsequently express it to be $W^{\mathtt{H}}(\mathbf{F},\mathbf{H},\mathbf{h}^r) \equiv \mathrm{w}^{\mathtt{h}}(\mathbb{B},\mathbf{h},\mathbf{h}^r) = \rho_o\psi^{\mathtt{h}}(\mathbb{B},\mathbf{h},\mathbf{h}^r) - (\mu_0/2)J\mathbf{h}\cdot\mathbf{h}$, where $\psi^{\mathtt{h}}$ is the Helmholtz free energy density associated with the h-MRE. Moreover, we treat the Eulerian fields to be functions of $\mathbf{F}$ (or $\mathbf{R}$) and their referential (or intermediate) counterparts, such tha $\mathbf{h} = \mathbf{h}(\mathbf{F},\mathbf{H})$ and $\mathbf{h}^r = \mathbf{h}^r(\mathbf{R},\boldsymbol{\mathcal{H}}^r)$. With these, a straightforward algebraic exercise starting from the variational statement (28) and utilizing (25), (46) leads to (see Appendix A of Mukherjee et al. (2021) for details)

$$\boldsymbol{\sigma} = \underbrace{\frac{2\rho_0}{J}\left[\frac{\partial\psi^{\mathtt{h}}}{\partial\mathbb{B}}\right]_{\mathbf{h},\mathbf{h}^r}\mathbb{B}}_{\boldsymbol{\sigma}^{\mathtt{e}}} + \underbrace{\frac{2}{J\det\mathbf{Z}}\left[\mathbf{Z}\ \mathrm{skw}\big(\mathbf{h}^r\otimes\mathbf{b}^r\big)\mathbf{V}\mathbf{Z}\right]}_{\boldsymbol{\sigma}^{\mathtt{r}}} + \underbrace{\left[\mathbf{h}\otimes\mathbf{b} - \frac{\mu_0}{2}|\mathbf{h}|^2\mathbf{I}\right]}_{\boldsymbol{\sigma}^{\mathtt{maxw}}}, \tag{75}$$

where three distinct components of the total $\boldsymbol{\sigma}$, namely the elastic $\boldsymbol{\sigma}^{\mathtt{e}}$, remanent $\boldsymbol{\sigma}^{\mathtt{r}}$ and Maxwell $\boldsymbol{\sigma}^{\mathtt{maxw}}$ stress parts are obtained. In this last expression, we introduce the Eulerian counterpart of $\boldsymbol{\mathcal{B}}^r$ to be $\mathbf{b}^r = -\rho_0[\partial\psi^{\mathtt{h}}/\partial\mathbf{h}^r]_{\mathbb{B},\mathbf{h}}$, such that, $\mathbf{b}^r = \mathbf{R}\boldsymbol{\mathcal{B}}^r$. Moreover, in (75) we use the explicit fourth order tensor expression for $\partial\mathbf{R}/\partial\mathbf{F}$ from (Chen and Wheeler, 1993), which, in turn, introduces the tensors $\mathbf{V}$ and $\mathbf{Z}$ defined as

$$\mathbf{V} = \mathbf{F}\mathbf{R}^T \qquad \text{and} \qquad \mathbf{Z} = \mathrm{tr}[\mathbf{V}]\mathbf{I} - \mathbf{V}. \tag{76}$$

By its very definition from $(25)_1$, where $\mathbf{S}$ is given by $(31)_2$, the total $\boldsymbol{\sigma}$ is symmetric. However, its components $\boldsymbol{\sigma}^{\mathtt{e}}$, $\boldsymbol{\sigma}^{\mathtt{r}}$ and $\boldsymbol{\sigma}^{\mathtt{maxw}}$ are not, in general, symmetric.

4.8.2. Cauchy stress in the F-B model

Similarly, the expression for total $\boldsymbol{\sigma}$ in the $\mathbf{F}-\mathbf{B}$ model can be obtained by first expressing $W^{\mathtt{B}}(\mathbf{F},\mathbf{B},\boldsymbol{\mathcal{H}}^r) \equiv \mathrm{w}^{\mathtt{b}}(\mathbb{B},\mathbf{b},\mathbf{h}^r) = \psi^{\mathtt{b}}(\mathbb{B},\mathbf{b},\mathbf{h}^r) - (1/2\mu_0)J\mathbf{b}\cdot\mathbf{b}$ with the Helmholtz free energy density now expressed in terms of $\mathbb{B}$, $\mathbf{b} = \mathbf{b}(\mathbf{F},\mathbf{B})$ and $\mathbf{h}^r = \mathbf{h}^r(\mathbf{R},\boldsymbol{\mathcal{H}}^r)$. The expression for $\boldsymbol{\sigma}$ from the variational statement (38) and (25), (46) becomes

$$\boldsymbol{\sigma} = \underbrace{\frac{2\rho_0}{J}\left[\frac{\partial\psi^{\mathtt{b}}}{\partial\mathbb{B}}\right]_{\mathbf{b},\mathbf{h}^r}\mathbb{B}}_{\boldsymbol{\sigma}^{\mathtt{e}}} + \underbrace{\frac{2}{J\det\mathbf{Z}}\left[\mathbf{Z}\ \mathrm{skw}\big(\mathbf{h}^r\otimes\mathbf{b}^r\big)\mathbf{V}\mathbf{Z}\right]}_{\boldsymbol{\sigma}^{\mathtt{r}}} + \underbrace{\left[\mathbf{h}\otimes\mathbf{b} - \frac{\mu_0}{2}\Big(|\mathbf{h}|^2 - |\mathbf{m}|^2\Big)\mathbf{I}\right]}_{\boldsymbol{\sigma}^{\mathtt{maxw}}}, \tag{77}$$

where $\mathbf{b}^r = -\rho_0[\partial\psi^{\mathtt{b}}/\partial\mathbf{h}^r]_{\mathbb{B},\mathbf{b}}$. Thus, the expressions for the elastic and remanent Cauchy stresses remain the same in the $\mathbf{F}-\mathbf{H}$ and $\mathbf{F}-\mathbf{B}$ models, of course, the latter has a free energy density $\psi^{\mathtt{b}}$, while the former has $\psi^{\mathtt{h}}$ in their constitutive relations. Moreover, the hydrostatic part of the Maxwell stress gets modified in the case of the $\mathbf{F}-\mathbf{B}$ model, which is in agreement with the existing s-MRE constitutive models (Kankanala and Triantafyllidis, 2004; Dorfmann and Ogden, 2004; Danas, 2017).

Next, with a relative abuse in the notations[5], we express the non-Maxwell part of $\boldsymbol{\sigma}$ to be simply the mechanical Cauchy stress contribution, so that $\boldsymbol{\sigma}^{\mathtt{mech}} = \boldsymbol{\sigma}^{\mathtt{e}} + \boldsymbol{\sigma}^{\mathtt{r}}$. Of course, not only the mechanical strains, but also the magnetic remanent fields in the h-MRE contribute to $\boldsymbol{\sigma}^{\mathtt{mech}}$. In fact, the expressions of $\boldsymbol{\sigma}^{\mathtt{r}}$ in (75) and (77) show that the remanent stress arises whenever the currnet remanent magnetization $\mathbf{h}^r$ and its dual $\mathbf{b}^r$ cease to be parallel. This particular scenario arises during the non-aligned loading of the h-MREs, leading to a "magnetic torque"-like contribution to the total $\boldsymbol{\sigma}$.

The Maxwell stress $\boldsymbol{\sigma}^{\mathtt{maxw}}$, on the other hand, remains independent of the material properties, while only depending on the local $\mathbf{h}$ and $\mathbf{b}$ fields at any point in the continuum. The mechanical and Maxwell parts of the first Piola-Kirchhoff stress can then be obtained directly via $\mathbf{S}^{\mathtt{mech}} = J\boldsymbol{\sigma}^{\mathtt{mech}}\mathbf{F}^{-T}$ and $\mathbf{S}^{\mathtt{maxw}} = J\boldsymbol{\sigma}^{\mathtt{maxw}}\mathbf{F}^{-T}$, such that $\mathbf{S} = \mathbf{S}^{\mathtt{mech}} + \mathbf{S}^{\mathtt{maxw}}$.

5. Modeling of isotropic soft-MREs

In this section, we propose fully explicit, homogenization-guided phenomenological models for the s-MRE using both $\mathbf{F}-\mathbf{H}$ and $\mathbf{F}-\mathbf{B}$ formulations. These models have been developed independently of the previous h-MRE models and as we will show in the following are not exact duals. Instead, they are explicit and fully energetic exhibiting no dissipation. They are meant to be simpler but robust alternatives to the previous dissipative models when no (or very weak) magnetic dissipation is present.

The present phenomenological models are proposed in terms of two additional modeling parameters, which are subsequently obtained by calibration with the h-MRE models since the latter have been already calibrated with available RVE simulations. First, we propose models for incompressible MREs and then extend in an ad-hoc manner those models for quasi-incompressible ones. This extension serves only practical purposes since it allows for a simpler numerical implementation but should not be considered as an extension for arbitrarily compressible responses. In the following, we directly report the final expressions, while the reader is referred to the original work of Mukherjee et al. (2020) to find details on their derivations.

In this section, we will use only the energetic invariants, $I^{\mathtt{H}}_{\mathtt{i}}$ and $I^{\mathtt{B}}_{\mathtt{i}}$ (with $\mathtt{i} = 4, 5, 6$) defined in (52) and (53). The rest of the invariants involving the internal variable $\boldsymbol{\mathcal{H}}^r$ are not relevant in the context of s-MREs.

5.1. F-H expressions for s-MREs

We propose a phenomenological energy function for *incompressible* s-MREs in terms of three distinct energy contributions, namely, a fully decoupled mechanical and magnetic energy and an additional coupling energy, which reads

$$W^{\mathtt{H}}(\mathbf{F},\mathbf{H}) = \rho_0\Psi_{\mathtt{mech}}(I_1) + \rho_0\Psi^{\mathtt{H}}_{\mathtt{mag}}(I^{\mathtt{H}}_5) + \rho_0\Psi^{\mathtt{H}}_{\mathtt{couple}}(I^{\mathtt{H}}_4, I^{\mathtt{H}}_5) - \frac{\mu_0}{2}I^{\mathtt{H}}_5, \tag{78}$$

valid for all isochoric deformations states, i.e., $J = 1$. The effective mechanical energy $\Psi_{\mathtt{mech}}$ is given by (59), while the invariants $I^{\mathtt{H}}_4$ and $I^{\mathtt{H}}_5$ are those defined in (52).

[5] Perhaps the best word for this term would have been the stress in the material, i.e., $\boldsymbol{\sigma}^{\mathtt{mat}}$ to distinguish it from the Maxwell part that is present even when there is no material. Nevertheless, for historical reasons we keep here the earlier notations.

Magnetic energy. The *purely* magnetic part $\Psi^H_{\mathtt{mag}}$ is given in terms of a Gaussian Hypergeometric function, denoted by ${}_2\mathcal{F}_1$, as

$$\rho_0 \Psi^{\mathtt{H}}_{\mathtt{mag}}(I^{\mathtt{H}}_5) = -\frac{\mu_0\,\chi}{2} I^{\mathtt{H}}_5 {}_2\mathcal{F}_1 \left[\frac{1}{k^{\mathtt{H}}}, \frac{2}{k^{\mathtt{H}}}, 1+\frac{2}{k^{\mathtt{H}}}, -\left(\frac{\chi\sqrt{I^{\mathtt{H}}_5}}{m^s} \right)^{k^{\mathtt{H}}} \right]. \tag{79}$$

In this expression, $k^{\mathtt{H}}$ is a positive integer that will be calibrated against numerical data. Furthermore, m^s denotes the effective saturation magnetization and $\chi \equiv \mu/\mu_0 - 1$ is the effective magnetic susceptibility (and μ the effective permeability) given by

$$m^s = c\, m^s_{\mathtt{p}}, \qquad \chi = \frac{3\,c\,\chi_{\mathtt{p}}}{3+(1-c)\chi_{\mathtt{p}}}. \tag{80}$$

Here, $\chi_{\mathtt{p}}$ is the magnetic susceptibility of the particles. Usually, values between $10-100$ are representative of iron particles, while a value of $\chi_{\mathtt{p}} = 30$ was shown to correspond well to the commercially available carbon iron particles (CIP). This value is four times larger than that for hard magnetic NdFeB particles discussed in the previous section. The estimate for χ in (80) corresponds to the Maxwell-Garnett (or equivalently Hashin-Shtrikman) bound and was shown to be particularly accurate for isotropic s-MRE by comparison with corresponding experiments in Psarra et al. (2017) up to volume fractions of $c = 0.3$. Note further that the estimate for m^s is an exact homogenization result and has been verified by experiments in Danas et al. (2012) and numerical simulations Danas (2017) as well as shown via the approximate homoegenization estimates of Galipeau and Ponte Castañeda (2013). It implies that the effective saturation magnetization of the s-MRE composite is independent of its microstructure (e.g. whether particles are distributed isotropically or in particle-chains or have arbitrary shapes such as ellipsoids etc) and is only a function of the volume fraction of particles c and of their individual saturation magnetization $m^s_{\mathtt{p}}$. In particular, CIP have saturation magnetization much higher than that for NdFeB that attains values of $\mu_0 m^s_{\mathtt{p}} = 2.5\mathrm{T}$.

In turn, the function ${}_2\mathcal{F}_1$ is typically expressed in terms of a series given by,

$${}_2\mathcal{F}_1[a,b,c;z] = \sum_{n=0}^{\infty} \frac{(a)_n (b)_n}{(c)_n} \frac{z^n}{n!}, \tag{81}$$

with

$$(x)_0 = 1 \qquad \text{and} \qquad (x)_n = x(x+1)\cdots(x+n-1).$$

It can be shown via rigorous convergence tests that the infinite series in (81) converge for all $z < 0$ and non-negative a, b and c (Abramowitz and Stegun, 1972, p. 81-86). Hence, (81) can be evaluated numerically in a straightforward manner (Perger et al., 1993; Hankin, 2015). Of interest, however, are the first and second derivatives of $\Psi^H_{\mathtt{mag}}$ with respect to $\mathbf{h}$, which, as shown in the following, take very simple algebraic forms. The derivative of the Gaussian Hypergeometric function ${}_2\mathcal{F}_1$ with respect to its argument has a very simple form, which reads

$$\mathbf{m} = -\frac{\rho_0}{\mu_0}\frac{\partial \Psi^{\mathtt{H}}_{\mathtt{mag}}}{\partial \mathbf{H}}\mathbf{F}^T = \frac{\chi \mathbf{h}}{\left[1+(\chi)^{k^{\mathtt{H}}}\left(|\mathbf{h}|/m^s\right)^{k^{\mathtt{H}}}\right]^{1/k^{\mathtt{H}}}}. \tag{82}$$

Here, the initial susceptibility is always χ irrespective of the value of $k^{\mathtt{H}}$ thus leading to the same initial effective magnetization response of the s-MRE. The same is true for the saturation response,

which gives $|\mathbf{m}| = m^s = c\, m^s_{\mathrm{p}}$ as required by the homogenization, experimental and numerical results. On the other hand, the rate of magnetization at moderate fields depends on the power coefficient $k^{\mathtt{H}}$, which may be calibrated to follow closely available numerical or experimental data. Specifically, by direct calibration, we find in Section 7.1 that a value

$$k^{\mathtt{H}} = 4 \tag{83}$$

leads to a good fit for the magnetization response for all volume fractions $c \in [0, 0.3]$ and matrix

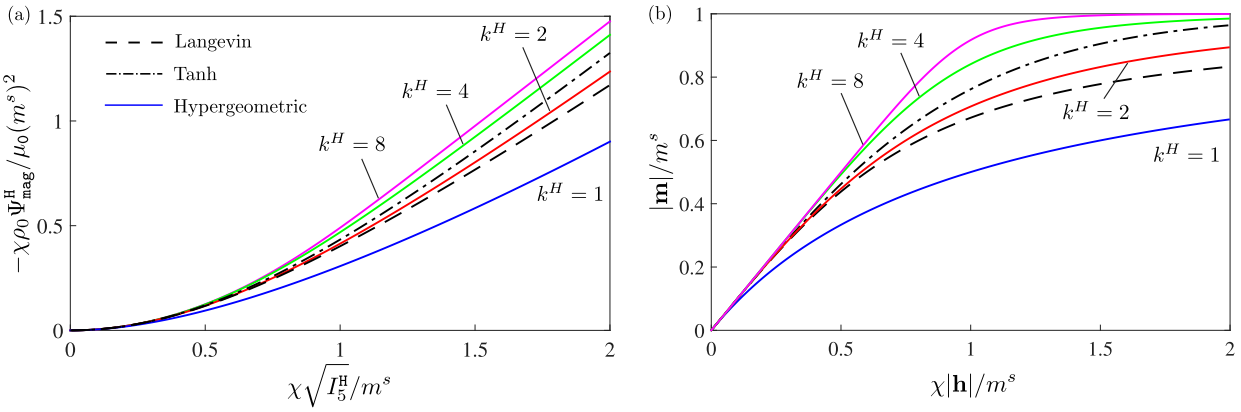

Figure 4: Comparison of (a) the magnetic energy functions and of (b) their derivatives obtained from and hypergeometric $\Psi^{\mathtt{H}}_{\mathtt{mag}}$ saturation function given in equation (82) for various exponents $k^{\mathtt{H}}$, the Langevin function and the hyperbolic tangent function (see (85). (Taken from Mukherjee et al. (2020)).

shear moduli analyzed in the present study. Of course, given any alternative experimental data, a different value for $k^{\mathtt{H}}$ may be used. For illustration purposes, we show in Fig. 4 representative curves of the hypergeometric function and its derivative, which gives the $\mathbf{m}-\mathbf{h}$ response as evaluated from equation (82). For comparison, we also show magnetization curves obtained by the Langevin-type and hyberbolic tangent functions (Danas, 2017) defined by

$$\text{Langevin}: \quad \rho_0\Psi^{\mathtt{H}}_{\mathtt{mag}}(\mathbf{F},\mathbf{H}) = -\frac{\mu_0(m^s)^2}{3\chi}\left\{\ln\left[\sinh\left(\frac{3\chi}{m^s}\sqrt{I^{\mathtt{H}}_5}\right)\right] - \ln\left[\frac{3\chi}{m^s}\sqrt{I^{\mathtt{H}}_5}\right]\right\} \tag{84}$$

$$\text{Tanh}: \quad \rho_0\Psi^{\mathtt{H}}_{\mathtt{mag}}(\mathbf{F},\mathbf{H}) = -\frac{\mu_0(m^s)^2}{\chi}\ln\left[\cosh\left(\frac{\chi}{m^s}\sqrt{I^{\mathtt{H}}_5}\right)\right] \tag{85}$$

such that

$$\text{Langevin}: \quad \mathbf{m} = m^s\mathcal{L}\left(\frac{3\chi|\mathbf{h}|}{m^s}\right)\frac{\mathbf{h}}{|\mathbf{h}|} \tag{86}$$

$$\text{Tanh}: \quad \mathbf{m} = m^s\tanh\left(\frac{\chi|\mathbf{h}|}{m^s}\right)\frac{\mathbf{h}}{|\mathbf{h}|}. \tag{87}$$

Here, $\mathcal{L}$ denotes the Langevin function

$$\mathcal{L}(x) = \coth x - x^{-1}, \qquad x \in \mathbb{R}, \tag{88}$$

Remark 10. The use of a hypergeometric function is done in order to allow for flexibility in the calibration process since the homogenized response of an MRE comprising magnetic particles with Langevin-type magnetization saturation response does not lead to an effective magnetization response of a Langevin-type. Before proceeding to the coupled energy part, we note further that the decoupled mechanical and magnetic energies are expressed in terms of the homogenized material parameters, which can be evaluated directly in terms of the constituents' properties and the particle volume fraction c.

Coupled energy.. Subsequently, and similar to the h-MRE models, we express the coupled magneto-mechanical energy as a function of the two invariants $I_4^{\mathtt{H}}$ and $I_5^{\mathtt{H}}$, thus taking the form

$$\Psi^{\mathtt{H}}_{\mathtt{couple}}(I_4^{\mathtt{H}}, I_5^{\mathtt{H}}) = \Psi_4^{\mathtt{H}}(I_4^{\mathtt{H}}) - \Psi_5^{\mathtt{H}}(I_5^{\mathtt{H}}), \tag{89}$$

with

$$\rho_0 \Psi_{\mathtt{i}}^{\mathtt{H}}(I_{\mathtt{i}}^{\mathtt{H}}) = \beta_1^{\mathtt{H}} \frac{\mu_0 (m^s)^2}{2\chi} \ln\left[1 + \sum_{q=1}^{4} \frac{1}{c}\left(\frac{4}{5}\chi\right)^{q+1} \left(\frac{c}{\beta_2^{\mathtt{H}}}\right)^{q} \left(\frac{\sqrt{I_{\mathtt{i}}^{\mathtt{H}}}}{m^s}\right)^{2q}\right], \tag{90}$$

with $\mathtt{i} = 4, 5$. Following the analysis in Mukherjee et al. (2020) and modifying slightly the coefficient $\beta_1^{\mathtt{H}}$ in order to fit better with the corresponding numerical RVE simulations for $c > 0.2$, we write

$$\beta_1^{\mathtt{H}} = \frac{5g(c)\,(1-c)\chi}{16}\beta_2^{\mathtt{H}}, \tag{91}$$

with

$$\begin{aligned} g(c) &= 1 + g_0 \tanh\left[\sum_{q=1}^{5} g_q c^{q+5}\right], \forall c \in [0, 0.5] \\ g_0, g_1, g_2, g_3, g_4, g_5 &= \{2530, -3.4, 38.5, -146, 231, -132\} \end{aligned} \tag{92}$$

and

$$\beta_2^{\mathtt{H}}(G_{\mathtt{m}}^*, c) = \alpha_1^{H}(G_{\mathtt{m}}^*) - \alpha_2^{\mathtt{H}}(G_{\mathtt{m}}^*)\mathcal{L}\big[c\,\alpha_3^{\mathtt{H}}(G_{\mathtt{m}}^*)\big], \tag{93}$$

with

$$\begin{aligned} &G_{\mathtt{m}}^* = G_{\mathtt{m}}/G_{\mathtt{m}}^{\mathtt{Ref}}, \quad G_{\mathtt{m}}^{\mathtt{Ref}} = 1\mathrm{MPa}, \\ &\alpha_1^{\mathtt{H}}(G_{\mathtt{m}}^*) = \exp\big[-0.29\tanh\big\{0.27(\ln G_{\mathtt{m}}^* + 7)\big\} - 1.575\big], \\ &\alpha_2^{\mathtt{H}}(G_{\mathtt{m}}^*) = \exp\big[4.4\mathcal{L}(-0.78\ln G_{\mathtt{m}}^*) - 5.2\big], \\ &\alpha_3^{\mathtt{H}}(G_{\mathtt{m}}^*) = \frac{0.1}{G_{\mathtt{m}}^* + 0.0007} - 5.4G_{\mathtt{m}}^* + 6.75. \end{aligned}$$

Here, $\mathcal{L}(.)$ is the Langevin function given by (88). Specifically, the function $g(c)$ is almost unit for $c \leq 0.2$ and thus results to no changes with respect to the work of Mukherjee et al. (2020). However, in that work, it was shown that the proposed model (which was calibrated by use of the implicit homogenization model of Lefèvre et al. (2017)) tends to underestimate the coupling for $c > 0.2$ by comparison to numerical RVE simulations. The function $g(c)$ (which remains the same for the subsequent $\mathbf{F} - \mathbf{B}$ formulation) serves to improve upon this issue. Also it becomes

equal to zero for $c \approx 0.5$. Beyond that value the coupling is almost negligible since the mechanical response becomes substantially stiff prohibiting any magnetostriction (see corresponding results in two-dimensions Danas (2017)).

In turn, the evolution of $\beta_2^{\mathtt{H}}$ with respect to $G_{\mathtt{m}}^*$ is mainly controlled by the coefficients $\alpha_1^{\mathtt{H}}$ and $\alpha_2^{\mathtt{H}}$. By contrast, the third coefficient $\alpha_3^{\mathtt{H}}$ is used to model the variation of $\beta_2^{\mathtt{H}}$ with respect to c for a given $G_{\mathtt{m}}^*$. Beyond $G_{\mathtt{m}}^* > 1$ a constant $\beta_2^{\mathtt{H}} \approx 0.155$ is sufficient. On the other hand, for very soft, gel-like MREs, i.e., in the range of $0.001 \leq G_{\mathtt{m}}^* \leq 0.01$, the coupling coefficient $\beta_2^{\mathtt{H}}$ becomes highly sensitive to $G_{\mathtt{m}}^*$ and c, resulting in a significant variation of $\beta_2^{\mathtt{H}}$ in this particular range. A more detailed discussion on the calibration process may be found in Mukherjee et al. (2020).

Remark 11. The parameters $\beta_1^{\mathtt{H}}$ and $\beta_2^{\mathtt{H}}$ may be regarded more generally as fitting constants that may be calibrated each time to describe a specific material composition. Then, the functional form of the model is straightforward and very simple to implement since it is explicit and analytical. An important observation in this context is related to the form of the coupled energy (89), and in particular the subtraction term $\Psi_4^{\mathtt{H}}(I_4^{\mathtt{H}}) - \Psi_5^{\mathtt{H}}(I_5^{\mathtt{H}})$. This is done for two reasons. First, the derivation of $\Psi_{\mathtt{couple}}^{\mathtt{H}}$ with respect to $\mathbf{h}$ leaves the magnetization response completely unaffected at small and very large applied magnetic fields, thus allowing the hypergeometric function in equation (79) to completely control the $\mathbf{m} - \mathbf{h}$ response at the initial regime and the saturation regime. The second reason is that only the $I_4^{\mathtt{H}} = \mathbf{F}^T\mathbf{h} \cdot \mathbf{F}^T\,\mathbf{h}$ part of the function contributes to the magnetostriction whenever a Eulerian field $\mathbf{h}$ is applied, while the corresponding $I_5^{\mathtt{H}} = \mathbf{h} \cdot \mathbf{h}$ part induces no magnetostriction. Moreover, we observe that $\Psi_{\mathtt{i}}^{\mathtt{H}}$ is non-convex with respect to $\sqrt{I_i^{\mathtt{H}}}$ since its derivative increases rapidly from zero to a maximum and then gradually decreases to zero (see Fig. 5b). As we will see in the following, such a function allows to obtain a material magnetostriction response that is initially quadratic, subsequently increases in a non-quadratic manner until finally reaching a saturating state.

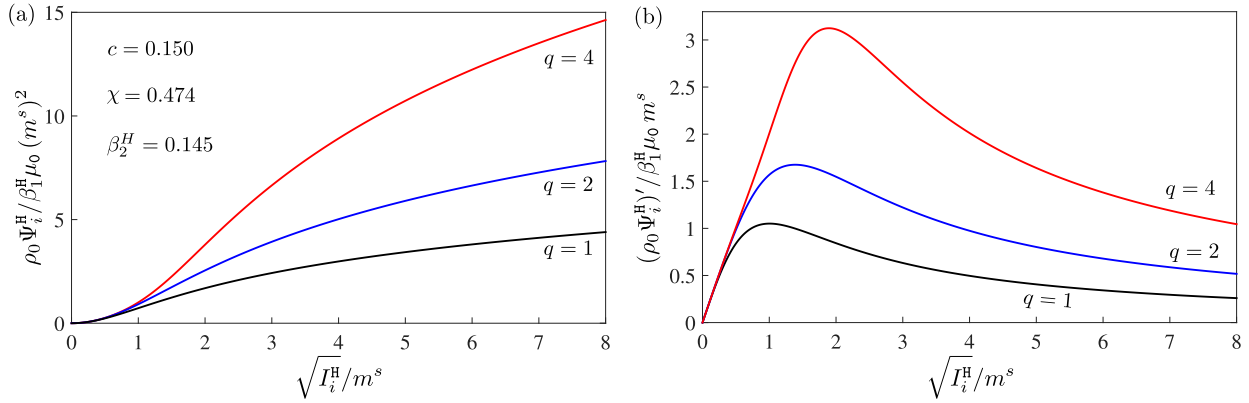

Figure 5: Representative plots of (a) the function $\Psi_i^{\mathtt{H}}$ (with $\mathtt{i} = 4, 5$) and (b) of its derivative with respect to $\sqrt{I_{\mathtt{i}}^{\mathtt{H}}}$ for $q = 1, 2, 4$. (Taken from Mukherjee et al. (2020)).

Quasi-incompressible extension. In spite of the fact that the assumption of an incompressible matrix and rigid particles leads to very efficient analytical modeling of the effective response, quasi-incompressible models for the MREs are employed in most of the computational investigations due to their simplicity to incorporate them in a finite-element solver. Unfortunately, carrying out the homogenization problem for even a quasi-incompressible matrix is extremely difficult

and no rigorous model is available up to date neither for the purely mechanical part nor for the magneto-mechanical part. In this regard, we propose an ad-hoc extension of the incompressible phenomenological model (78) that essentially relaxes slightly the assumption of incompressibility without affecting the aforementioned key features of the model at least in the case of high bulk modulus (i.e. quasi-incompressible materials). The proposed model reads

$$W^{\mathtt{H}}_{\mathtt{comp}}(\mathbf{F},\mathbf{H}) = \rho_0\Psi^{\mathtt{comp}}_{\mathtt{mech}}(\mathcal{I}_1,J) + \rho_0\Psi^{\mathtt{H}}_{\mathtt{mag}}(I^{\mathtt{H}}_5) + \rho_0\Psi^{\mathtt{H}}_{\mathtt{couple}}(I^{\mathtt{H}}_4,I^{\mathtt{H}}_5) - \rho_0\frac{J\,\mu_0}{2}I^{\mathtt{H}}_5, \tag{94}$$

where $\Psi^{\mathtt{comp}}_{\mathtt{mech}}$ has already been defined in (60), while the remaining of the functions remain unchanged.

5.2. F-B expressions for s-MREs

In principle, one may attempt to obtain an equivalent $\mathbf{F}-\mathbf{B}$ model via the partial Legendre-Fenchel transformation (37) of (78) with respect to $\mathbf{H}$. However, due to the strong nonlinearity of the functions associated with the proposed $\mathbf{F}-\mathbf{H}$ model (78), one can not obtain its complementary energy in an explicit form. By contrast, in the context of h-MREs that is possible by the introduction of the internal variable, which carries all the associated nonlinearities, while the dependence of the function on the main variables $\mathbf{H}$ (or $\mathbf{B}$) is fairly simple and thus transformable.

In any case, for completeness, we propose a complementary energy $W^{\mathtt{B}}$, which has the exact same form as that of $W^{\mathtt{H}}$ in (78), such that

$$W^{\mathtt{B}}(\mathbf{F},\mathbf{B}) = \rho_0\Psi_{\mathtt{mech}}(\mathbf{F}) + \rho_0\Psi^{\mathtt{B}}_{\mathtt{mag}}(I^{\mathtt{B}}_5) + \rho_0\Psi^{\mathtt{B}}_{\mathtt{couple}}(I^{\mathtt{B}}_5,I^{\mathtt{B}}_6) + \frac{1}{2\mu_0}I^{\mathtt{B}}_5, \tag{95}$$

where the magneto-mechanical invariants $I^{\mathtt{B}}_5$ and $I^{\mathtt{B}}_6$ have been defined in (53). Evidently, the first term of (95) that represents the purely mechanical component of $W^{\mathtt{B}}$ is identical to that in (78), and is given by (59). Also, the last term of (95) represents the $\mathbf{F}-\mathbf{B}$ version of the magnetostatic energy of free space (Dorfmann and Ogden, 2004).

It remains then to prescribe the two free energies, namely, the magnetic and the coupled free energy. Due to their intrinsic properties, $\Psi^{\mathtt{B}}_{\mathtt{mag}}$ and $\Psi^{\mathtt{B}}_{\mathtt{couple}}$ retain the same functional form as their $\mathbf{F}-\mathbf{H}$ counterparts (79) and (89), respectively. Note that, as shown in Figs. 4 and 5, the hypergeometric ${}_2\mathcal{F}_1$ and the $\Psi^{\mathtt{H}}_{\mathtt{i}}$ functions are rich enough to model a wide variety of constitutive responses.

Magnetic energy. In this regard, the purely magnetic part $\Psi^{\mathtt{B}}_{\mathtt{mag}}$ is chosen as

$$\Psi^{\mathtt{B}}_{\mathtt{mag}}(I^{\mathtt{B}}_5) = -\frac{\chi}{2\mu_0\,(1+\chi)}I^{\mathtt{B}}_5\,{}_2\mathcal{F}_1\left[\frac{1}{k^{\mathtt{B}}},\frac{2}{k^{\mathtt{B}}},1+\frac{2}{k^{\mathtt{B}}},-\left(\frac{\chi\sqrt{I^{\mathtt{B}}_5}}{(1+\chi)\mu_0 m^s}\right)^{k^{\mathtt{B}}}\right]. \tag{96}$$

Similar to the $\mathbf{F}-\mathbf{H}$ version, a single exponent

$$k^{\mathtt{B}} = 6 \tag{97}$$

provides a good fit to the magnetization response for all particle volume fractions and matrix shear moduli considered in this study. Note that the purely magnetic energy (96) in the $\mathbf{F}-\mathbf{B}$ model is *not* an exact Legendre transform of the corresponding magnetic energy (79) of the $\mathbf{F}-\mathbf{H}$ model. Thus, no direct correlation can be drawn between the model parameters $k^{\mathtt{B}}$ and $k^{\mathtt{H}}$ and their calibration values.

Coupled energy. The coupled energy is defined by

$$\Psi^{\mathtt{B}}_{\mathtt{couple}}(I^{\mathtt{B}}_5, I^{\mathtt{B}}_6) = \Psi^{\mathtt{B}}_6(I^{\mathtt{B}}_6) - \Psi^{\mathtt{B}}_5(I^{\mathtt{B}}_5), \tag{98}$$

with

$$\Psi^{\mathtt{B}}_{\mathtt{i}}(I^{\mathtt{B}}_i) = \beta^{\mathtt{B}}_1 \frac{(1+\chi)\mu_0(m^s)^2}{2\chi} \ln\left[1 + \sum_{q=1}^{4} \frac{1}{c}\left(\frac{5}{4}\frac{\chi}{1+\chi}\right)^{q+1}\left(\frac{c}{\beta^{\mathtt{B}}_2}\right)^{q}\left(\frac{\sqrt{I^{\mathtt{B}}_{\mathtt{i}}}}{\mu_0 m^s}\right)^{2q}\right], \tag{99}$$

where $\mathtt{i} = 5, 6$ and again $m^s = c\, m^s_{\mathtt{p}}$.

As in the $\mathbf{F} - \mathbf{H}$ version, and following Mukherjee et al. (2020), we have

$$\beta^{\mathtt{B}}_1 = \frac{16}{5}\frac{\chi(\chi+1)(1-c)}{\left([5(\chi+1) - 2(1-c)\chi^2\right]\left[(1-c)\chi^2 + 5(\chi+1)\right]} g(c)\beta^{\mathtt{B}}_2. \tag{100}$$

The function $g(c)$ is the same with that used in (92). In turn, for $\beta^{\mathtt{B}}_2$, we use two piecewise continuous functions of $G^*_{\mathtt{m}}$ and c to model the variation of $\beta^{\mathtt{B}}_2$ in the $G^*_{\mathtt{m}} - c$ space, which reads

$$\beta^{\mathtt{B}}_2(G^*_{\mathtt{m}}, c) = \begin{cases} \alpha^{\mathtt{B}}_1(G^*_{\mathtt{m}}) - \alpha^{\mathtt{B}}_2(G^*_{\mathtt{m}})\mathcal{L}\left[c\,\alpha^{\mathtt{B}}_3(G^*_{\mathtt{m}})\right], & \text{if} \quad G^*_{\mathtt{m}} \leq 0.1 \\ 0.4055 - 0.5\,c\left[1 - 0.67\mathcal{L}(15G^*_{\mathtt{m}})\right] & \text{otherwise} \end{cases} \tag{101}$$

with

$$\begin{aligned} \alpha^{\mathtt{B}}_1(G^*_{\mathtt{m}}) &= \exp\left[-0.029\ln G^*_{\mathtt{m}} - 0.982\right], \\ \alpha^{\mathtt{B}}_2(G^*_{\mathtt{m}}) &= \exp\left[1.78\mathcal{L}(-0.32\ln G^*_{\mathtt{m}}) - 1.78\right], \\ \alpha^{\mathtt{B}}_3(G^*_{\mathtt{m}}) &= \exp\left[0.14 - 0.54\ln G^*_{\mathtt{m}}\right]. \end{aligned}$$

Here, $\mathcal{L}(.)$ is again the Langevin function defined in (88). The first function is similar to $\beta^{\mathtt{H}}_2$ with three coefficients $\alpha^{\mathtt{B}}_1$, $\alpha^{\mathtt{B}}_2$ and $\alpha^{\mathtt{B}}_3$, which are functions of $G^*_{\mathtt{m}}$, whereas, the second function, which models $\beta^{\mathtt{B}}_2$ for all $G^*_{\mathtt{m}} > 0.1$, is rather a simple function of $G^*_{\mathtt{m}}$ and c. We note that the two fitting functions for β^B_2 have approximately the same magnitude near $G^*_{\mathtt{m}} = 0.1$. Thus, the particular choice of piecewise continuous β^B_2 ensures a constant transition from the Langevin decay to the linear decrease regime.

Remark 12. As stated earlier, (98) retains an identical functional form as its $\mathbf{F} - \mathbf{H}$ counterpart in (89) except that the magneto-mechanical coupling is now modeled in terms of the invariant $I^{\mathtt{B}}_6$. This choice of the coupling invariant is not arbitrary, rather, is directly equivalent to the $\mathbf{F} - \mathbf{H}$ model. The invariant $I^{\mathtt{H}}_4$ can be expressed in terms of the Eulerian $\mathbf{h}$ as $I^{\mathtt{H}}_4 = \mathbf{F}^T\mathbf{h} \cdot \mathbf{F}^T\mathbf{h}$. The Legendre-Fenchel transform of that invariant leads to the invariant $I^{\mathtt{B}}_6 = \mathbf{F}^T\mathbf{b} \cdot \mathbf{F}^T\mathbf{b}$.

Quasi-incompressible extension. A quasi-incompressible version of (95) is given by

$$\begin{aligned} W^{\mathtt{B}}_{\mathtt{comp}}(\mathbf{F}, \mathbf{B}) &= \rho_0 \Psi^{\mathtt{comp}}_{\mathtt{mech}}(\mathcal{I}_1, J) + \rho_0 \Psi^{\mathtt{B}}_{\mathtt{mag}}(I^{\mathtt{B}}_5) \\ &\quad + \rho_0 \Psi^{\mathtt{B}}_{\mathtt{couple}}(I^{\mathtt{B}}_5, I^{\mathtt{B}}_6) + \frac{1}{2\mu_0 J} I^{\mathtt{B}}_5, \end{aligned} \tag{102}$$

where $\rho_0 \Psi^{\mathtt{comp}}_{\mathtt{mech}}$ is given by (60).

5.3. Total Cauchy stress in s-MREs

Similar to the h-MRE analysis, the expression for the total Cauchy stress in terms of the current magnetic and mechanical variables are often sought after to gain more insight to the different stress contributions. Thus, the expressions for $\boldsymbol{\sigma}$ in terms of $\mathbb{B}$, $\mathbf{h}$ and $\mathbf{b}$, where $\mathbb{B} = \mathbf{F}\mathbf{F}^T$ is the left Cauchy-Green tensor, in the $\mathbf{F}-\mathbf{H}$ and $\mathbf{F}-\mathbf{B}$ settings are provided in the following. The expressions obtained in the context of s-MREs may be retrieved readily from those for the h-MREs in equations (75) and (77) by simply setting the remanent part equal to zero.

5.3.1. Cauchy stress in the F-H model

We first express $W^{\mathtt{H}}$ in terms of $\mathbf{F}$, $\mathbf{H}$ and subsequently express it to be $W^{\mathtt{H}}(\mathbf{F},\mathbf{H}) \equiv \mathrm{w}^{\mathtt{h}}(\mathbb{B},\mathbf{h}) = \rho_o\psi^{\mathtt{h}}(\mathbb{B},\mathbf{h}) - (\mu_0/2)J\mathbf{h}\cdot\mathbf{h}$, where $\psi^{\mathtt{h}}$ is the Helmholtz free energy density associated with the s-MRE. Moreover, we treat the Eulerian fields to be functions of $\mathbf{F}$ and their referential counterparts, such that $\mathbf{h} = \mathbf{h}(\mathbf{F},\mathbf{H})$. This leads to

$$\boldsymbol{\sigma} = \underbrace{\frac{2\rho_0}{J}\left[\frac{\partial\psi^{\mathtt{h}}}{\partial\mathbb{B}}\right]_{\mathbf{h}}\mathbb{B}}_{\boldsymbol{\sigma}^{\mathtt{e}}\equiv\boldsymbol{\sigma}^{\mathtt{mech}}} + \underbrace{\left[\mathbf{h}\otimes\mathbf{b} - \frac{\mu_0}{2}|\mathbf{h}|^2\mathbf{I}\right]}_{\boldsymbol{\sigma}^{\mathtt{maxw}}}, \tag{103}$$

where two distinct components of the total $\boldsymbol{\sigma}$, namely the elastic or mechanical $\boldsymbol{\sigma}^{\mathtt{mech}}$ and Maxwell $\boldsymbol{\sigma}^{\mathtt{maxw}}$ stress parts are obtained. By its very definition from $(25)_1$, where $\mathbf{S}$ is given by $(31)_2$, the total $\boldsymbol{\sigma}$ is symmetric. However, its components $\boldsymbol{\sigma}^{\mathtt{mech}}$ and $\boldsymbol{\sigma}^{\mathtt{maxw}}$ are not, in general, symmetric.

5.3.2. Cauchy stress in the F-B model

Similarly, the expression for total $\boldsymbol{\sigma}$ in the $\mathbf{F}-\mathbf{B}$ model can be obtained by first expressing $W^{\mathtt{B}}(\mathbf{F},\mathbf{B}) \equiv \mathrm{w}^{\mathtt{b}}(\mathbb{B},\mathbf{b}) = \psi^{\mathtt{b}}(\mathbb{B},\mathbf{b}) - (1/2\mu_0)J\mathbf{b}\cdot\mathbf{b}$ with the Helmholtz free energy density now expressed in terms of $\mathbb{B}$ and $\mathbf{b} = \mathbf{b}(\mathbf{F},\mathbf{B})$. The expression for $\boldsymbol{\sigma}$ from the variational statement (38) and (25) becomes

$$\boldsymbol{\sigma} = \underbrace{\frac{2\rho_0}{J}\left[\frac{\partial\psi^{\mathtt{b}}}{\partial\mathbb{B}}\right]_{\mathbf{b}}\mathbb{B}}_{\boldsymbol{\sigma}^{\mathtt{e}}\equiv\boldsymbol{\sigma}^{\mathtt{mech}}} + \underbrace{\left[\mathbf{h}\otimes\mathbf{b} - \frac{\mu_0}{2}\Big(|\mathbf{h}|^2 - |\mathbf{m}|^2\Big)\mathbf{I}\right]}_{\boldsymbol{\sigma}^{\mathtt{maxw}}}. \tag{104}$$

Thus, the expressions for the elastic or mechanical and remanent Cauchy stresses remain the same in the $\mathbf{F}-\mathbf{H}$ and $\mathbf{F}-\mathbf{B}$ models, of course, the latter has a free energy density $\psi^{\mathtt{b}}$, while the former has $\psi^{\mathtt{h}}$ in their constitutive relations. Moreover, the hydrostatic part of the Maxwell stress gets modified in the case of the $\mathbf{F}-\mathbf{B}$ model, which is in agreement with the existing s-MRE constitutive models (Kankanala and Triantafyllidis, 2004; Dorfmann and Ogden, 2004; Danas, 2017).

Again, the Maxwell stress $\boldsymbol{\sigma}^{\mathtt{maxw}}$ remains independent of the material properties, while only depending on the local $\mathbf{h}$ and $\mathbf{b}$ fields at any point in the continuum. The mechanical and Maxwell parts of the first Piola-Kirchhoff stress can then be obtained directly via $\mathbf{S}^{\mathtt{mech}} = J\boldsymbol{\sigma}^{\mathtt{mech}}\mathbf{F}^{-T}$ and $\mathbf{S}^{\mathtt{maxw}} = J\boldsymbol{\sigma}^{\mathtt{maxw}}\mathbf{F}^{-T}$, such that $\mathbf{S} = \mathbf{S}^{\mathtt{mech}} + \mathbf{S}^{\mathtt{maxw}}$.

6. Numerical implementations for MREs

The rate-type variational principles for the $\mathbf{F}-\mathbf{H}$ and $\mathbf{F}-\mathbf{B}$ models in Section 3 are now expressed in a time discrete form to analyze periodic unit-cells or any practical boundary value problem (BVP) involving MREs. First, the scalar potential-based $\mathbf{F}-\mathbf{H}$ model is presented in a time discrete form. This will be followed by the specification of the corresponding vector potential-based $\mathbf{F}-\mathbf{B}$ model. We discuss the general case of h-MREs, whereby that of the s-MREs may be obtained by omitting the terms related to magnetic dissipation.

6.1. Time discrete variational principle for F-H formulation

The scalar potential-based $\mathbf{F}-\mathbf{H}$ model needs to be solved for the displacement $\mathbf{u}$ and potential φ, such that $\mathbf{F}=\mathbf{I}+\mathrm{Grad}\mathbf{u}$ and $\mathbf{H}=-\mathrm{Grad}\varphi$ both satisfy the relevant Dirichlet boundary conditions. Specifically in the incremental setting of a numerical solution, we consider the state of the continuum to be known at a time t, from which we solve for the minimizing fields $\mathbf{u}$ and φ for the next time step $\tau=t+\Delta t$. We henceforth indicate all the variables with the subscripts "t" or "τ" to indicate that the variables are computed at a given discrete time.

First, the variational principle (28) upon substitution of $D(\dot{\boldsymbol{\mathcal{H}}}^r)$ from (72) reads

$$\begin{aligned}\dot{\Pi}^{\mathtt{H}} \;=\; \inf_{\dot{\mathbf{u}}\in\widetilde{\mathcal{U}}}\;\sup_{\dot{\varphi}\in\widetilde{\mathcal{G}}}\;\inf_{\dot{\boldsymbol{\mathcal{H}}}^r\in\mathbb{R}^3}\;\Bigg[\int_{\mathbb{R}^3}\dot{W}^{\mathtt{H}}(\mathbb{C},\mathbf{H},\boldsymbol{\mathcal{H}}^r)\;\mathrm{d}\mathcal{V}_0-\int_{\partial\mathcal{V}_0}\mathbf{T}\cdot\dot{\mathbf{u}}\;\mathrm{d}\mathcal{S}_0\\ +\int_{\mathcal{V}_0}\sup_{\boldsymbol{\mathcal{B}}^r}\;\inf_{\dot{\Lambda}\geq 0}\;\Big\{\boldsymbol{\mathcal{B}}^r\cdot\dot{\boldsymbol{\mathcal{H}}}^r-\dot{\Lambda}\Phi(\boldsymbol{\mathcal{B}}^r)\Big\}\;\mathrm{d}\mathcal{V}_0\Bigg].\end{aligned}\tag{105}$$

Expressing all the rates in time discrete form like $\dot{\mathbf{u}}=(\mathbf{u}_\tau-\mathbf{u}_t)/\Delta t$ and taking note on the fact that the state at time t is already converged, one can express the rate-type variational principle (105) in a time-discrete form so that

$$\begin{aligned}\Pi^{\mathtt{H}}_\tau \;=\; \inf_{\mathbf{u}_\tau\in\mathcal{U}}\;\sup_{\varphi_\tau\in\mathcal{G}}\;\Bigg[\int_{\mathcal{V}_0}\mathcal{W}^{\mathtt{H}}_\tau(\mathbb{C},\mathbf{H})\;\mathrm{d}\mathcal{V}_0+\int_{\mathbb{R}^3\setminus\mathcal{V}_0}W^{\mathtt{H}}_{c=0,\tau}(\mathbb{C},\mathbf{H})\;\mathrm{d}\mathcal{V}_0\\ -\int_{\partial\mathcal{V}_0}\mathbf{T}\cdot\mathbf{u}_\tau\;\mathrm{d}\mathcal{S}_0\Bigg].\end{aligned}\tag{106}$$

Here the subscript "τ" with $W^{\mathtt{H}}$ and $\mathcal{W}^{\mathtt{H}}$ both indicate that all their arguments are at a discrete time τ. In (106) we have introduced a *reduced energy density* $\mathcal{W}^{\mathtt{H}}_\tau$, which is, in turn, the variational principle employed for the computation for the internal variable $\boldsymbol{\mathcal{H}}^r_\tau$ locally at each point of the computation domain, such that

$$\mathcal{W}^{\mathtt{H}}_\tau(\mathbb{C},\mathbf{H})=\inf_{\boldsymbol{\mathcal{H}}^r_\tau}\;\sup_{\boldsymbol{\mathcal{B}}^r}\;\inf_{\Delta\Lambda\geq 0}\;\Big\{W^{\mathtt{H}}_\tau(\mathbb{C},\mathbf{H},\boldsymbol{\mathcal{H}}^r)+\boldsymbol{\mathcal{B}}^r\cdot\boldsymbol{\mathcal{H}}^r_\tau-\Delta\Lambda\Phi(\boldsymbol{\mathcal{B}}^r)\Big\}.\tag{107}$$

This last variational statement, in turn, leads to the time-discrete forms of the KKT conditions stated in (73). Finally, the admissible sets for $\mathbf{u}_\tau$ and φ_τ are given by, respectively,

$$\mathcal{U}\equiv\Big\{\mathbf{u}_\tau:\mathbf{F}_\tau=\mathbf{I}+\mathrm{Grad}\mathbf{u}_\tau,\;\forall\;\mathbf{X}\in\mathbb{R}^3,\;\mathbf{u}_\tau=\overline{\mathbf{u}}_\tau\;\forall\;\mathbf{X}\in\partial\mathcal{V}^{\mathbf{u}}_0\Big\},\tag{108}$$

$$\mathcal{G}\equiv\Big\{\varphi_\tau:\mathbf{H}_\tau=-\mathrm{Grad}\varphi_\tau,\;\forall\;\mathbf{X}\in\mathbb{R}^3,\;\varphi_\tau=\overline{\varphi}_\tau\;\forall\;\mathbf{X}\in\partial\mathcal{V}^{\varphi}_\infty\Big\}.\tag{109}$$

Thus, for an initial guess $\mathbf{u}_\tau$ and φ_τ we first update the internal variable $\boldsymbol{\mathcal{H}}^r_\tau$ via extremizing (107). Then the updated $\boldsymbol{\mathcal{H}}^r_\tau$ is used to compute for the corrector for $\mathbf{u}_\tau$ and φ_τ from the global implicit solver. Thus, the introduction of the reduced energy density allows us to update $\boldsymbol{\mathcal{H}}^r_\tau$ locally at each integration point, while computing for $\mathbf{u}_\tau$ and φ_τ from the global variational principle. This computation algorithm provides efficient update procedure for $\mathbf{u}$, φ and $\boldsymbol{\mathcal{H}}^r$ and facilitates the implementation in the commercially-available finite-element solvers like ABAQUS/Standard (Miehe et al., 2011; Rosato and Miehe, 2014; Mukherjee et al., 2021).

We note further here that corresponding expressions can be obtained for s-MREs by simply dropping the time discrete character of the previous equations, setting dissipation equal to zero and using the energy functions presented in Section 5.1.

6.2. Time discrete variational principle for F-B formulation

The time discrete equivalent of the $\mathbf{F}-\mathbf{B}$-based variational principle (38) can be obtained in a similar way to (106) after substituting $D(\dot{\boldsymbol{\mathcal{H}}}^r)$ from (72), finally leading to

$$\Pi^{\mathtt{B}}_\tau = \inf_{\mathbf{u}_\tau\in\mathcal{U}}\ \inf_{\mathbf{A}_\tau\in\mathcal{B}}\Big[\int_{\mathcal{V}_0}\mathcal{W}^{\mathtt{B}}_\tau(\mathbb{C},\mathbf{B})\ \mathrm{d}\mathcal{V}_0+\int_{\mathbb{R}^3\setminus\mathcal{V}_0}W^{\mathtt{B}}_{c=0,\tau}(\mathbb{C},\mathbf{B})\ \mathrm{d}\mathcal{V}_0 - \int_{\partial\mathcal{V}_0}\mathbf{T}\cdot\mathbf{u}_\tau\ \mathrm{d}\mathcal{S}_0\Big], \tag{110}$$

where the reduced energy density $\mathcal{W}^{\mathtt{B}}_\tau(\mathbb{C},\mathbf{B})$ reads

$$\mathcal{W}^{\mathtt{B}}_\tau(\mathbb{C},\mathbf{B}) = \inf_{\boldsymbol{\mathcal{H}}^r_\tau}\ \sup_{\boldsymbol{\mathcal{B}}^r}\ \inf_{\Delta\Lambda\geq 0}\Big\{W^{\mathtt{B}}_\tau(\mathbb{C},\mathbf{B},\boldsymbol{\mathcal{H}}^r)+\boldsymbol{\mathcal{B}}^r\cdot\boldsymbol{\mathcal{H}}^r_\tau-\Delta\Lambda\Phi(\boldsymbol{\mathcal{B}}^r)\Big\}. \tag{111}$$

Again, the extremization of (111) leads to the KKT conditions for the $\mathbf{F}-\mathbf{B}$ model and thus, to the update equations for $\boldsymbol{\mathcal{H}}^r_\tau$. The admissible set $\mathcal{U}$ for the displacement field remains the same as in (108), while the admissible set for the vector potential $\mathbf{A}_\tau$ reads

$$\mathcal{B}\equiv\Big\{\mathbf{A}_\tau:\mathbf{B}_\tau=\mathrm{Curl}\ \mathbf{A}_\tau,\ \mathrm{Div}\ \mathbf{A}_\tau=0,\ \forall\ \mathbf{X}\in\mathbb{R}^3,\ \mathbf{A}_\tau=\overline{\mathbf{A}}_\tau,\ \forall\ \mathbf{X}\in\partial\mathcal{V}^{\mathbf{A}}_0\Big\}, \tag{112}$$

where the condition $\mathrm{Div}\ \mathbf{A}_\tau=0$ is the well-known Coulomb gauge that leads to an uniquely defined vector potential $\mathbf{A}_\tau$ (Biro and Preis, 1989; Stark et al., 2015). The implementation of the Coulomb gauge may be done in various manners. Here, we use a penalty formulation described in Dorn et al. (2021) together with under-integration of the constraint term. Again, for an initial guess of $\mathbf{u}_\tau$ and $\mathbf{A}_\tau$, the internal variable $\boldsymbol{\mathcal{H}}^r_t$ is updated to be $\boldsymbol{\mathcal{H}}^r_\tau$ at the local integration points. The subsequent global increments for the $\mathbf{u}_\tau$ and $\mathbf{A}_\tau$ are carried out via using the *already updated* $\boldsymbol{\mathcal{H}}^r_\tau$. The correction increments for $\mathbf{u}_\tau$ and $\mathbf{A}_\tau$ continues until a global convergence is achieved.

Again, we note that corresponding expressions can be obtained for s-MREs by simply dropping the time discrete character of the previous equations, setting dissipation equal to zero and using the energy functions presented in Section 5.2.

6.3. The periodic numerical homogenization problem

The above general time discrete variational principles can be easily modified to deal with a periodic problem. The main difference between a periodic and a standard boundary value problem (BVP) lies in the domain that we analyze the problem and the corresponding boundary conditions.

While a BVP comprises magnetic or non-magnetic bodies and potentially an air domain that may extend far from the bodies analyzed, the periodic homogenization problem only considers *by definition* a unit-cell comprising the phases that are analyzed. By extension, there is no presence of surrounding air since the surrounding domain is filled by repetition of the principal unit-cell in all three dimensions *ad infinitum*. For that to be true, one needs to apply periodic boundary conditions while maintaining geometric periodicity of the boundary of the unit-cell (Michel et al., 1999) (although the later is not an absolutely necessary condition but mostly a convenient one). In the following, we discuss the homogenization problem in the context of h-MREs, i.e., dissipative systems using the previously presented time discrete variational formulations. Corresponding straightforward expressions can then be obtained for s-MREs by simply dropping the time discrete character of the previous formulations.

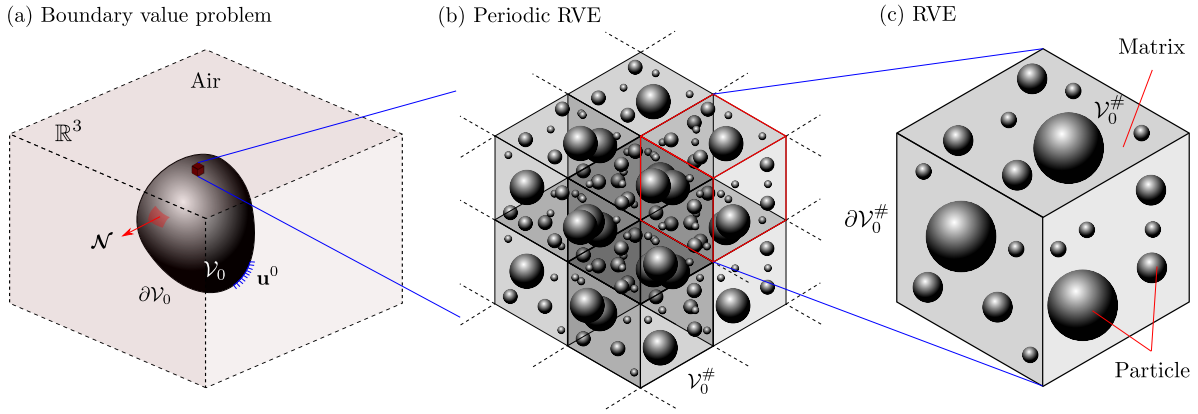

Figure 6: Schematic diagram of (a) macroscopic boundary value problem involving a MRE sample in air having a reference volume $\mathcal{V}_0$ with unit normal $\boldsymbol{\mathcal{N}}$ on the boundary $\partial\mathcal{V}_0$ and a representative boundary with fixed displacement $\mathbf{u}_0$, (b) periodic arrangement of a RVE with polydisperse spherical inclusions and (c) a RVE occupying a reference volume $\mathcal{V}_0^\#$ and boundary $\partial\mathcal{V}_0^\#$.

As shown in Fig. 6, each point of the macro-continuum $\mathcal{V}_0$ (Fig. 6a) is assumed to be described well at the microscale by a representative volume element (RVE) having a reference volume of $\mathcal{V}_0^\#$ and comprising two (or more) phases, denoted as $\mathtt{i} = \mathtt{p}, \mathtt{m}$ representing the particle and matrix phase, respectively (Fig. 6c). This assumption may be considered sufficient for the present h-MRE composites provided that the particle size is sufficiently smaller than the specimen analyzed[6]. Then, for spatially and temporally (quasi-static here) slowly varying mechanical and magnetic fields at the macroscopic scales, the previous microstructural assumptions allow for separation of length scales ($\mathcal{V}_0^\# \ll \mathcal{V}_0$). In addition, following Danas (2017), we consider a slowly varying microstructure, so that the microstructure can be assumed to be (locally) periodic (see Fig. 6b). This interpretation results in periodic boundary conditions applied on a single RVE (see Fig. 6c).

[6]The particle size in typical h-MREs is in the order of $10 - 30\,\mu\text{m}$, while a cubic RVE as we will see contains approximately five particles per direction, i.e., has a side of $\sim 50 - 150\,\mu\text{m}$ at moderate volume fractions. The specimen sizes in actual experiments are usually in the centimeter scale and thus are sufficiently larger than the microstructure. In turn, such models including any type of phenomenological ones should be used with caution in the context of slender structures such as those in Psarra et al. (2017) and Kim et al. (2018), where one or two dimensions of the specimen may be a fraction of a millimeter. In that case, additional calibration may be required.

6.3.1. Local energy density of the constituents

Henceforth, the microscopic field variables along with the energy functions and the corresponding invariants are indicated with a $\breve{(\cdot)}$ symbol in order to distinguish them from their macroscopic counterparts. Since the microstructure is heterogeneous, the referential representations of the local energy density $\breve{W}$ and the local dissipation potential $\breve{D}$ both depend on the microscopic (here) reference coordinate $\mathbf{X}$[7]. Also for brevity in the presentation, we will use the notation introduced in (44) to denote simultaneously whenever possible with a unique symbol $\breve{\mathbf{G}} = \{\breve{\mathbf{H}}, \breve{\mathbf{B}}\}$. Thus, one has

$$\breve{W}(\mathbf{X}, \breve{\mathbf{F}}, \breve{\mathbf{G}}, \breve{\boldsymbol{\mathcal{H}}}^r) = \Theta(\mathbf{X})\breve{W}_{\mathtt{m}}^{\mathtt{G}}(\breve{\mathbf{F}}, \breve{\mathbf{G}}, \breve{\boldsymbol{\mathcal{H}}}^r) + (1 - \Theta(\mathbf{X}))\breve{W}_{\mathtt{p}}^{\mathtt{G}}(\breve{\mathbf{F}}, \breve{\mathbf{G}}, \breve{\boldsymbol{\mathcal{H}}}^r) \tag{113}$$

and

$$\breve{D}(\mathbf{X}, \dot{\breve{\boldsymbol{\mathcal{H}}}}^r) = \Theta(\mathbf{X})\breve{D}_{\mathtt{m}}(\dot{\breve{\boldsymbol{\mathcal{H}}}}^r) + (1 - \Theta(\mathbf{X}))\breve{D}_{\mathtt{p}}(\dot{\breve{\boldsymbol{\mathcal{H}}}}^r), \tag{114}$$

In this last two expressions, $\Theta(\mathbf{X})$ denotes the characteristic function taking the value $\Theta(\mathbf{X}) = 1$ if $\mathbf{X} \in \mathcal{V}_0^{\#\mathtt{m}}$ and $\Theta(\mathbf{X}) = 0$ if $\mathbf{X} \in \mathcal{V}_0^{\#\mathtt{p}}$. The microscopic energy densities $\breve{W}_{\mathtt{p}}^{\mathtt{G}}$ and $\breve{W}_{\mathtt{m}}^{\mathtt{G}}$ are directly identified with the corresponding ones discussed in the previous sections by simply taking the limits $c = 1$ for the particle phase and $c = 0$ for the matrix phase, while all field variables $\breve{\mathbf{F}}$, $\breve{\mathbf{G}}$ and $\breve{\boldsymbol{\mathcal{H}}}^r$ should be simply replaced by the corresponding overscript ones $\breve{(\cdot)}$.

Remark 13. In (114), we may readily set $\breve{D}_{\mathtt{m}} = 0$ since the magnetic dissipation is identically zero in the non-magnetic polymer matrix in the present analysis. Nonetheless, note that other microstructures of more phases or different properties may be readily analyzed by the present approach. For instance, one may have a magnetic polymer together with magnetic particles of different properties or anything else that one may consider useful to analyze. In this sense, the above descriptions serve only as a representative example.

6.3.2. Incremental homogenization framework

This section discusses briefly the incremental periodic homogenization framework for h-MREs based on an incremental micro-potential $\breve{\mathcal{W}}(\mathbf{X}, \breve{\mathbf{F}}_\tau, \breve{\mathbf{G}}_\tau)$, which can be defined by substituting all field quantities with an overscript $\breve{(\cdot)}$. The average deformation gradient $\mathbf{F}$ and Lagrangian h-field $\mathbf{H}$ or magnetic field $\mathbf{B}$ at a discrete time $\tau \equiv t + \Delta t$ are then expressed in terms of the volume averages of the corresponding microscopic quantities, so that

$$\mathbf{F}_\tau = \frac{1}{|\mathcal{V}_0^{\#}|}\int_{\mathcal{V}_0^{\#}} \breve{\mathbf{F}}_\tau(\mathbf{X})\, \mathrm{d}V, \qquad \mathbf{G}_\tau = \frac{1}{|\mathcal{V}_0^{\#}|}\int_{\mathcal{V}_0^{\#}} \breve{\mathbf{G}}_\tau(\mathbf{X})\, \mathrm{d}V, \tag{115}$$

respectively.

The microscopic displacements $\breve{\mathbf{u}}_\tau(\mathbf{X})$, the microscopic scalar potential $\breve{\varphi}_\tau(\mathbf{X})$ and vector potential $\breve{\mathbf{A}}_\tau(\mathbf{X})$ are additively decomposed into linear (macroscopic) and higher order (microscopic

[7] In principle, one may introduce a different notation for the position vector to insist that it corresponds to the reference coordinate in the microscopic scale which is obviously a different measure from the reference coordinate in the macroscopic scale, i.e., $\breve{\mathbf{X}} \equiv \mathbf{X}$. Nonetheless for the sake of simplicity in notation, we drop the superscript from $\mathbf{X}$, since all calculation regarding a unit-cell will always take place in the microscopic scale.

fluctuation) contributions

$$\begin{cases} \breve{\mathbf{u}}_\tau(\mathbf{X}) = (\mathbf{F}_\tau - \mathbf{I}) \cdot \mathbf{X} + \widetilde{\mathbf{u}}_\tau(\mathbf{X}), \\ \breve{\varphi}_\tau(\mathbf{X}) = -\mathbf{H}_\tau \cdot \mathbf{X} + \widetilde{\varphi}_\tau(\mathbf{X}) \qquad\qquad \forall\ \mathbf{X} \in \mathcal{V}_0^{\#} \\ \breve{\mathbf{A}}_\tau(\mathbf{X}) = \dfrac{1}{2}\mathbf{B} \times \mathbf{X} + \widetilde{\mathbf{A}}_\tau(\mathbf{X}), \end{cases} \tag{116}$$

where $\widetilde{\mathbf{u}}_\tau(\mathbf{X})$, $\widetilde{\varphi}_\tau(\mathbf{X})$ and $\widetilde{\mathbf{A}}_\tau(\mathbf{X})$ are the relevant periodic (with periodicity that of the unit-cell) fluctuation fields. Their average over $\mathcal{V}_0^{\#}$ is required to vanish such that (116) is consistent with (115), which is automatically fulfilled for $\mathcal{V}_0^{\#}$-*periodic* fluctuation fields.

In the dissipative problem, one then has to solve first the local minimization problem with respect to the internal variable such that we can define the local energy (following exactly the definition (107) or (111))

$$\breve{\mathcal{W}}_\tau^{\mathtt{G}}(\mathbf{X}, \breve{\mathbf{F}}_\tau, \breve{\mathbf{G}}_\tau) = \inf_{\breve{\boldsymbol{\mathcal{H}}}^r} \sup_{\breve{\boldsymbol{\mathcal{B}}}^r} \inf_{\Delta\breve{\Lambda}\geq 0} \Big\{ \breve{W}_\tau^{\mathtt{G}}(\mathbf{X}, \breve{\mathbf{F}}, \breve{\mathbf{H}}, \breve{\boldsymbol{\mathcal{H}}}^r) + [1ex] \breve{\boldsymbol{\mathcal{B}}}^r \cdot \breve{\boldsymbol{\mathcal{H}}}^r{}_\tau - \Delta\breve{\Lambda}\, \Phi(\mathbf{X}, \breve{\boldsymbol{\mathcal{B}}}^r) \Big\}. \tag{117}$$

As a consequence, the incremental homogenized energy $\mathcal{W}_\tau^{\mathtt{G}}$ reads

$$\mathcal{W}_\tau^{\mathtt{G}}(\mathbf{F}_\tau, \mathbf{G}_\tau) = \inf_{\breve{\mathbf{u}}_\tau \in \mathcal{K}(\mathbf{F}_\tau)} \sup_{\{\breve{\varphi}_\tau | \breve{\mathbf{A}}_\tau\} \in \mathcal{G}(\mathbf{G}_\tau)} \left[\frac{1}{\mathcal{V}_0^{\#}} \int_{\mathcal{V}_0^{\#}} \breve{\mathcal{W}}_\tau^{\mathtt{G}}(\mathbf{X}, \breve{\mathbf{F}}_\tau, \breve{\mathbf{G}}_\tau)\ \mathrm{d}V \right], \tag{118}$$

where $\mathcal{K}$ and $\mathcal{G}$ represents the sets of admissible microscopic displacement and magnetic scalar or vector potential fields, defined, respectively, as

$$\mathcal{K}(\mathbf{F}_\tau) = \left\{ \breve{\mathbf{F}}_\tau = \mathbf{I} + \mathrm{Grad}\ \breve{\mathbf{u}}_\tau, \breve{\mathbf{u}}_\tau = (\mathbf{F}_\tau - \mathbf{I}) \cdot \mathbf{X} + \widetilde{\mathbf{u}}_\tau,\ \widetilde{\mathbf{u}}_\tau \text{ periodic in } \mathcal{V}_0^{\#} \right\} \tag{119}$$

and

$$\begin{cases} \mathrm{F-H\ case:} \\ \mathcal{G}(\mathbf{H}_\tau) = \left\{ \breve{\mathbf{H}}_\tau = -\mathrm{Grad}\ \breve{\varphi}_\tau, \breve{\varphi}_\tau = -\mathbf{H}_\tau \cdot \mathbf{X} + \widetilde{\varphi}_\tau,\ \widetilde{\varphi}_\tau \text{ periodic in } \mathcal{V}_0^{\#} \right\} \\ \mathrm{F-B\ case:} \\ \mathcal{G}(\mathbf{B}_\tau) = \left\{ \breve{\mathbf{B}}_\tau = \mathrm{Curl}\ \breve{\mathbf{A}}_\tau, \breve{\mathbf{A}}_\tau = \dfrac{1}{2}\mathbf{B}_\tau \times \mathbf{X} + \widetilde{\mathbf{A}}_\tau,\ \widetilde{\mathbf{A}}_\tau \text{ periodic in } \mathcal{V}_0^{\#} \right\} \end{cases} \tag{120}$$

Applying then the Hill-Mandel lemma, we obtain the homogenized constitutive relations defined as

$$\mathbf{S}_\tau = \frac{\partial \mathcal{W}_\tau^{\mathtt{G}}}{\partial \mathbf{F}_\tau}(\mathbf{F}_\tau, \mathbf{G}_\tau), \quad \begin{cases} \mathrm{F-H\ case:} \quad \mathbf{B}_\tau = -\dfrac{\partial \mathcal{W}_\tau^{\mathtt{H}}}{\partial \mathbf{H}_\tau}(\mathbf{F}_\tau, \mathbf{H}_\tau), \\ \mathrm{F-B\ case:} \quad \mathbf{H}_\tau = \dfrac{\partial \mathcal{W}_\tau^{\mathtt{B}}}{\partial \mathbf{B}_\tau}(\mathbf{F}_\tau, \mathbf{B}_\tau). \end{cases} \tag{121}$$

At this stage, the definition of the incremental homogenization problem for h-MREs is formally complete and one could proceed to compare the explicit model with the numerical RVE homogenized response (118). Nevertheless, it has been shown in Danas (2017) that such use of (118) does not reveal properly the effective magneto-mechanical response that arises from interactions between the magnetic particles. In fact, it was shown that even for a non-magnetic material, one would obtain magnetostrictive strains if a magnetic field was applied. This discussion is rather less straightforward and the reader is referred to the original article for more details. In view of this observation, further modifications to the incremental variational principle are necessary, as detailed in the following.

6.3.3. Augmented F-H potential energy for RVE simulations

Recent works of Keip and Rambausek (2016), Danas (2017) and Mukherjee et al. (2020) pointed out a key difference between the electro-active and magneto-active boundary value problems. Electro-active elastomers are typically loaded by electrodes that are directly attached to the material. In contrast, the MREs are usually immersed in the magnetic field created by fixed poles of electromagnets that rest at a certain distance away from the MRE sample (Bodelot et al., 2017; Zhao et al., 2019). One of the main differences between those two problems is that in the first the electric fields are zero outside the body, implying a zero Maxwell stress in vacuum, while in the second the magnetic fields and thus the Maxwell stress are not zero. In an effort to appropriately take into account the pure magneto-mechanical coupling in the RVE, free from the effect of those macroscopic boundary conditions, Danas (2017) and Mukherjee et al. (2020) proposed an augmented potential energy that involves three additional loading terms to deal with the surrounding RVE medium, the applied Eulerian magnetic field and the potential control of an average mechanical stress field. This potential energy allows to describe properly the magnetic effects (including the Maxwell stresses) exerted by the surrounding RVEs on the RVE under study and is briefly revisited here for completeness. The reader is referred to (Danas, 2017) for a complete discussion on this highly non-trivial matter.

Specifically, the first additional term serves to describe the application of the *current* macroscopic h-field, $\mathbf{h}^{\mathtt{app}}$, at the level of the RVE, instead of the referential one, $\mathbf{H}$. This may be achieved by the use of a penalty term $\frac{\mu_0}{2\zeta}|\mathbf{F}_\tau^{-T}\mathbf{H}_\tau - \mathbf{h}_\tau^{\mathtt{app}}|^2$ with $\zeta \ll 1$. Next, the macroscopic background energy $-\mu_0 I_5^{\mathtt{H}}/2$ (or $-\mu_0 J I_5^{\mathtt{H}}/2$ in the quasi-incompressible case) is subtracted from (118). This accounts for the presence of the neighboring RVEs (see Fig. 6b) by imposing the continuity of the macroscopic Maxwell stresses between neighboring RVEs, far from the boundaries of the specimen. Finally, to be able to prescribe macroscopic mechanical stress $\mathbf{S}_\tau^{\mathtt{mech}}$ instead of deformation $\mathbf{F}$, one may consider the term $\mathbf{S}_\tau^{\mathtt{mech}} : (\mathbf{F}_\tau - \mathbf{I})$. Assembling these three additional terms together, we obtain the augmented potential energy (Mukherjee et al., 2020)

$$\begin{aligned}\mathscr{P}_\tau^{\mathtt{H}}(\mathbf{F}_\tau, \mathbf{H}_\tau) = \mathcal{W}_\tau^{\mathtt{H}}(\mathbf{F}_\tau, \mathbf{H}_\tau) + \frac{\mu_0}{2}\mathbf{F}_\tau^{-T}\mathbf{H}_\tau \cdot \mathbf{F}_\tau^{-T}\mathbf{H}_\tau \\ + \frac{\mu_0}{2\zeta}|\mathbf{F}_\tau^{-T}\mathbf{H}_\tau - \mathbf{h}_\tau^{\mathtt{app}}|^2 - \mathbf{S}_\tau^{\mathtt{mech}} \cdot (\mathbf{F}_\tau - \mathbf{I}),\end{aligned} \tag{122}$$

with $\mathcal{W}_\tau^{\mathtt{H}}$ defined by (118) by replacing $\mathbf{G} \equiv \mathbf{H}$. The resulting Euler-Lagrange equations of the RVE response under the prescribed magnetic and mechanical loads introduced in (122) are obtained by

setting $\delta\mathscr{P}^{\mathtt{H}}_{\tau}(\mathbf{F}_{\tau},\mathbf{H}_{\tau})=0$, which leads to

$$\mathbf{S}_{\tau}-\mathbf{S}^{\mathtt{maxw}}_{\tau}-\mathbf{S}^{\mathtt{mech}}_{\tau}=\mathbf{0},\ \ \mathbf{B}_{\tau}-\mu_0\mathbb{C}^{-1}\mathbf{H}_{\tau}-\frac{\mu_0}{\zeta}\mathbf{F}^{-1}_{\tau}(\mathbf{F}^{-T}_{\tau}\mathbf{H}_{\tau}-\mathbf{h}^{\mathtt{app}}_{\tau})=\mathbf{0}. \tag{123}$$

Here, $\mathbf{S}^{\mathtt{maxw}}=J\boldsymbol{\sigma}^{\mathtt{maxw}}\mathbf{F}^{-T}$ is the 1st Piola-Kirchhoff expression for the energetic Maxwell stress given in terms of $\mathbf{h}$ and $\mathbf{b}$ as defined by (75). In turn, by writing the second equation in (123) in terms of the Eulerian parts as

$$\mathbf{b}_{\tau}-\mu_0\mathbf{h}_{\tau}-\frac{\mu_0}{\zeta}(\mathbf{h}_{\tau}-\mathbf{h}^{\mathtt{app}}_{\tau})=0, \tag{124}$$

one simply obtains the magnetization constitutive relation (5), with

$$\frac{1}{\zeta}(\mathbf{h}_{\tau}-\mathbf{h}^{\mathtt{app}}_{\tau})=\mathbf{m}. \tag{125}$$

This is achieved since $\mathbf{h}_{\tau}\to\mathbf{h}^{\mathtt{app}}_{\tau}$ as $\zeta\to 0$ making the first term finite and equal to $\mathbf{m}$. Again, the reader is referred to Danas (2017) for more details on this part.

Remark 14. These additional terms to the homogenization variational principle *do not* alter the microscopic constitutive models and thus, the effective incremental energy $\mathcal{W}^{\mathtt{H}}_{\tau}$, but changes the boundary conditions applied across the periodic RVE in terms of the macroscopic fields $\mathbf{S}_{\tau}$ and $\mathbf{H}_{\tau}$. Such a modification allows us to obtain the magneto-mechanical coupling effects arising from the local particle interactions subject to background average Eulerian magnetic fields.

6.3.4. Augmented F-B potential energy for RVE simulations

In an exactly similar fashion, one may obtain an augmented potential energy in the $\mathbf{F}-\mathbf{B}$ space. Specifically, the first additional term serves to describe the application of the *current* macroscopic b-field, $\mathbf{b}^{\mathtt{app}}$, at the level of the RVE, instead of the referential one, $\mathbf{B}$. This may be achieved by the use of a penalty term $\dfrac{J}{2\zeta\,\mu_0}|J^{-1}\mathbf{F}_{\tau}\mathbf{H}_{\tau}-\mathbf{b}^{\mathtt{app}}_{\tau}|^2$ with $\zeta\ll 1$. Next, the macroscopic background energy $I^{\mathtt{B}}_5/2\mu_0$ (or $JI^{\mathtt{B}}_5/2\mu_0$ in the quasi-incompressible case) is subtracted from (118). This accounts for the presence of the neighboring RVEs (see Fig. 6b) by imposing the continuity of the macroscopic Maxwell stresses between neighboring RVEs, far from the boundaries of the specimen. Finally, to be able to prescribe macroscopic mechanical stress $\mathbf{S}^{\mathtt{mech}}_{\tau}$ instead of deformation $\mathbf{F}$, one may consider the term $\mathbf{S}^{\mathtt{mech}}_{\tau}:(\mathbf{F}_{\tau}-\mathbf{I})$. Assembling these three additional terms together, we obtain the augmented potential energy (Danas, 2017)

$$\begin{aligned}\mathscr{P}^{\mathtt{B}}_{\tau}(\mathbf{F}_{\tau},\mathbf{B}_{\tau})=\mathcal{W}^{\mathtt{B}}_{\tau}(\mathbf{F}_{\tau},\mathbf{B}_{\tau})-\frac{1}{2\mu_0 J}\mathbf{F}_{\tau}\mathbf{B}_{\tau}\cdot\mathbf{F}_{\tau}\mathbf{B}_{\tau}\\ +\frac{J}{2\zeta\mu_0}|J^{-1}\mathbf{F}_{\tau}\mathbf{B}_{\tau}-\mathbf{b}^{\mathtt{app}}_{\tau}|^2-\mathbf{S}^{\mathtt{mech}}_{\tau}\cdot(\mathbf{F}_{\tau}-\mathbf{I}),\end{aligned} \tag{126}$$

with $\mathcal{W}^{\mathtt{B}}_{\tau}$ defined by (118) by replacing $\mathbf{G}\equiv\mathbf{B}$. The resulting Euler-Lagrange equations of the RVE response under the prescribed magnetic and mechanical loads introduced in (126) are obtained by setting $\delta\mathscr{P}^{\mathtt{B}}_{\tau}(\mathbf{F}_{\tau},\mathbf{B}_{\tau})=0$, which leads to

$$\mathbf{S}_{\tau}-\mathbf{S}^{\mathtt{maxw}}_{\tau}-\mathbf{S}^{\mathtt{mech}}_{\tau}=\mathbf{0},\ \ \mathbf{H}_{\tau}-\frac{1}{\mu_0 J}\mathbb{C}\mathbf{B}_{\tau}+\frac{1}{\zeta\mu_0}\mathbf{F}^{T}_{\tau}(J^{-1}\mathbf{F}_{\tau}\mathbf{B}_{\tau}-\mathbf{b}^{\mathtt{app}}_{\tau})=\mathbf{0}. \tag{127}$$

Here, $\mathbf{S}^{\mathtt{maxw}} = J\boldsymbol{\sigma}^{\mathtt{maxw}}\mathbf{F}^{-T}$ is the 1st Piola-Kirchhoff expression for the energetic Maxwell stress given in terms of $\mathbf{h}$ and $\mathbf{b}$ as defined by (77). In turn, by writing the second equation in (127) in terms of the Eulerian parts as

$$\mathbf{h}_\tau - \frac{1}{\mu_0}\mathbf{b}_\tau + \frac{1}{\zeta\mu_0}(\mathbf{b}_\tau - \mathbf{b}_\tau^{\mathtt{app}}) = 0, \tag{128}$$

one simply obtains the magnetization constitutive relation (5), with

$$\frac{1}{\zeta\mu_0}(\mathbf{b}_\tau - \mathbf{b}_\tau^{\mathtt{app}}) = \mathbf{m}. \tag{129}$$

Again, the reader is referred to Danas (2017) for more details on this part.

7. Results: Periodic RVE simulations and model assessment

This section discusses the model assessment via comparisons with the corresponding numerical RVE results under coupled magneto-mechanical loading conditions. In all subsequent results, we use a standard incompressible Neo-Hookean energy for the polymer matrix phase, i.e.,

$$\rho_0\Psi_{\mathtt{m}}^{\mathtt{mech}}(I_1) = \frac{G_{\mathtt{m}}}{2}(I_1 - 3). \tag{130}$$

This functional form is used in (59) to obtain the effective mechanical energy for the analytical model. We recall that in the analytical model the mechanical response of the particles is considered rigid. In turn, the magnetic properties of the particle are reported in Table 2 and correspond to a commercially available NdFeB material. In particular, these parameters are obtained by fitting the purely magnetic model with the experimentally measured hysteresis loops of magnetically isotropic NdFeB particles reported in Deng et al. (2015). Evidently, the model is general enough to be able to deal with any other type of hard magnetic particles.

Table 2: Magnetic properties of the NdFeB particles

$\chi_{\mathtt{p}}^e$	$\chi_{\mathtt{p}}^r$	$\mu_0 m_{\mathtt{p}}^s$ (T)	$b_{\mathtt{p}}^c$ (T)	μ_0 ($\mu\mathrm{N}\cdot\mathrm{A}^2$)
0.105	8.0	0.842	1.062	$4\pi 10^{-1}$

The numerical simulations use the same functions and parameters as the analytical model with only two differences that do not affect, however, the validity of the comparison. The first difference is the use of a quasi-incompressible energy for both the matrix and the particle phase, which is simply obtained by adding compressible terms in (59), such that it becomes

$$\rho_0\Psi_{\mathtt{comp,i}}^{\mathtt{mech}}(I_1, J) = \frac{G_{\mathtt{i}}}{2}(I_1 - 3 - 2\ln J) + \frac{G'_{\mathtt{i}}}{2}(J-1)^2, \qquad \mathtt{i} = \mathtt{m}, \mathtt{p}. \tag{131}$$

The quasi-incompressible character of the matrix is ensured by setting $G'_{\mathtt{m}} = 500G_{\mathtt{m}}$. Use of higher values has shown practically no difference in the simulated effective results. The second difference is the use of finite but large Lamé moduli for the particle, i.e., $G_{\mathtt{p}} = 500G_{\mathtt{m}}$ and $G'_{\mathtt{p}} = 500G_{\mathtt{p}}$. The phase contrast ratio of $G_{\mathtt{p}}/G_{\mathtt{m}} = 500$ has been shown in several earlier studies (see for instance Idiart et al. (2006a); Lopez-Pamies et al. (2013); Papadioti et al. (2016)) to be sufficiently large and thus render a nearly rigid mechanical response for the particle.

The RVE geometries are constructed by use of the RSA (random sequential adsorption) method. This allows to add sequentially inclusions of spherical (Lopez-Pamies et al., 2013) or ellipsoidal (Anoukou et al., 2018) shape in a cubic periodic unit cell. We perform the calculation by ranging the number of particles from 60-300. Three or more realizations are used to obtain an average and scatter response of those RVEs.

The results in the following sections consider the variation of two parameters, namely, the particle volume fraction c and the matrix shear modulus $G_{\mathtt{m}}$, which are, in fact, the two critical parameters that can be varied during the fabrication of h-MREs. Instead, the magnetic properties of the particle phase are kept constant.

7.1. h-MRE models versus FE simulations

7.1.1. Cyclic magnetic loading and calibration of β parameter

In this section, the goal is to calibrate the coupling parameter β introduced in the coupled magneto-mechanical energy (89) and (98) for the analytical models by use of corresponding RVE simulations. For this purpose, we fix the matrix shear modulus to $G_{\mathtt{m}} = 0.5$ MPa and vary the particle volume fraction $c = 0.1$, 0.2 and 0.3. The proposed shear modulus resembles closely that of the moderately-soft, commercially-available Sylgard-184 PDMS elastomer (Park et al., 2018; Wang et al., 2019).

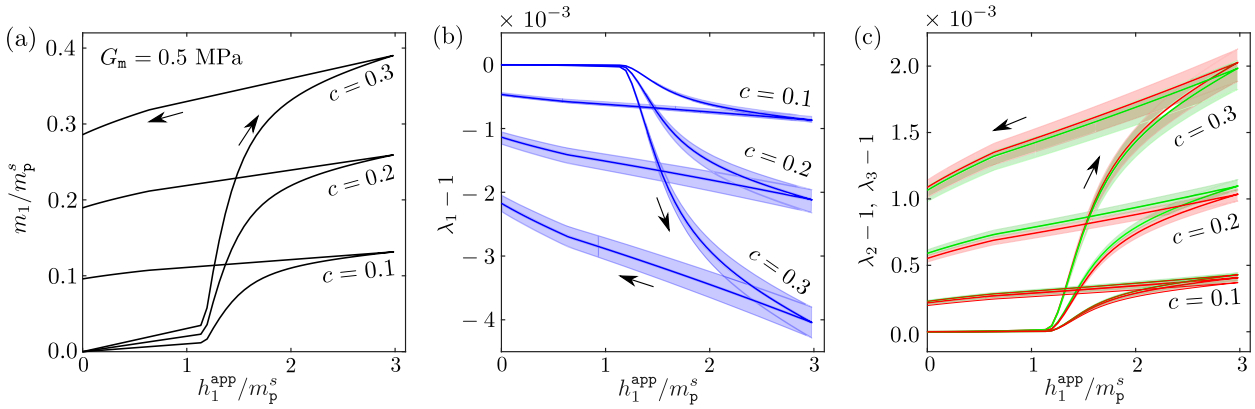

Figure 7: Numerically computed effective (a) magnetization, (b) parallel and (c) transverse magnetostrictions the h-MRE RVEs, subjected to uniaxial Eulerian $\mathbf{h}^{\mathtt{app}} = h_1^{\mathtt{app}}\mathbf{e}_1$ loading/unloading. The average effective responses (solid lines) along with the range of their fluctuations (light patches) for different realizations of the respective RVEs are indicated. The RVEs of different volume fractions are comprised of random polydisperse spherical hard-magnetic inclusions, coming from three distinct families. (Taken from Mukherjee et al. (2021)).

We consider symmetric cyclic magnetic loading in terms of $\mathbf{h}^{\mathtt{app}} = h_1^{\mathtt{app}}\mathbf{e}_1$ with a maximum amplitude $h_1^{\mathtt{app}} = 3\, m_{\mathtt{p}}^s$. Note that the loading rate does *not* play any role here, since both the macro and microscopic h-MRE models are rate-independent. As mechanical boundary conditions we employ

$$S_{11}^{\mathtt{mech}} = S_{22}^{\mathtt{mech}} = S_{33}^{\mathtt{mech}} = 0, \qquad F_{ij} = 0, \quad \forall i \neq j. \tag{132}$$

Similar to the numerical RVE results of non-hysteretic s-MREs (Mukherjee et al., 2020), in h-MREs too, the effective magnetostriction response exhibits a certain variance with respect to the RVE realizations, even for sufficiently large number of polydisperse spherical inclusions. For

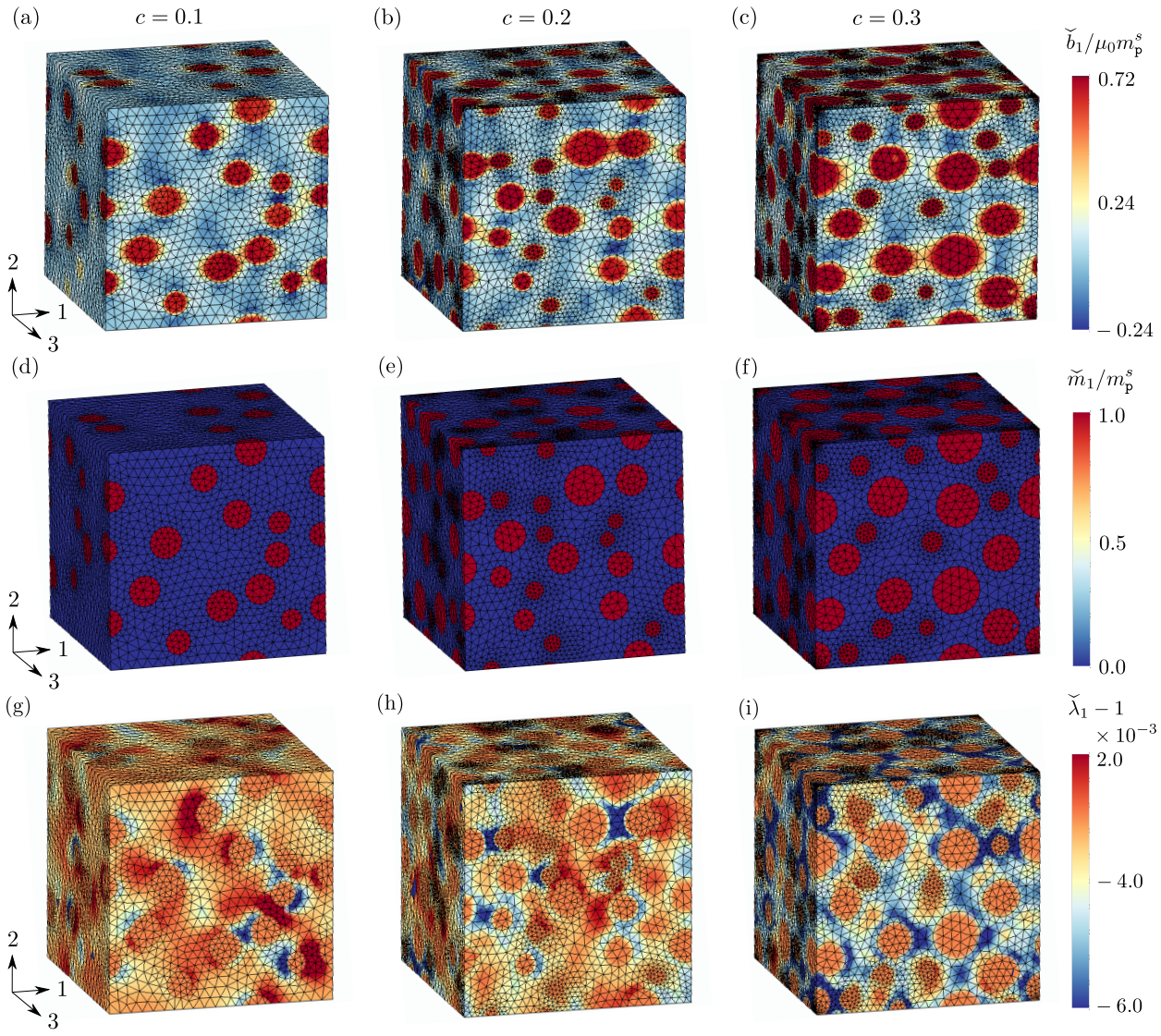

Figure 8: Contours of the numerically computed (a-c) normalized microscopic $\breve{b}_1$, (d-f) normalized local $\breve{m}_1$ and (g-i) nominal mechanical strain $\breve{\lambda}_1 - 1$ in the RVEs *after* the first half cycle of loading along $\mathbf{e}_1$, under which the effective responses are shown in Fig. 7. Three different, RVEs having (a,d,g) $c = 0.1$, (b,e,h) 0.2 and (c,f,i) 0.3 are shown. (Taken from Mukherjee et al. (2021)).

the effective RVE half-cycle responses shown in Fig 7, we employ five different RVE realizations per particle volume fraction $c = 0.1$, 0.2 and 0.3. The corresponding average magnetization, m_1/m_{p}^s and the parallel, $\lambda_1 - 1$ and transverse, $\lambda_{2,3} - 1$, magnetostrictions are shown in Fig. 7. The light-colored patches around the respective averages indicate the scatter resulting from the considered realizations.

Specifically, in Fig. 7a, the scatter of the magnetization response is found to be vanishingly small, whereas, those of the parallel (λ_1 in Fig. 7b) and transverse magnetostrictions (λ_2 and λ_3 in Fig. 7c) are gradually increasing with the magnetic load. Notice from Fig. 7 that neither the effective magnetization, nor the magnetostriction saturates at higher h-fields. Rather, they main-

tain a slope with the applied $h_1^{\mathtt{app}}$. Such response can be attributed to the inherent non-saturating magnetization response of the NdFeB particles, as observed in Fig. 3 for $\chi_{\mathtt{p}}^e > 0$. Moreover, we observe that the overall amplitude of the magnetostriction is rather small ($\sim 10^{-3}$) indicating that a matrix with shear modulus $G_{\mathtt{m}} = 0.5\,\text{MPa}$ is rather stiff in relation to the magnetic particle-to-particle forces. Even so, a permanent deformation is obtained upon complete removal of the applied magnetic field. This is obviously a direct consequence of the permanent magnetization of the particles and of their mutual interaction once magnetized permanently.

In Fig. 8a-c, we show the contours of the microscopic $\breve{b}_1/\mu_0 m_{\mathtt{p}}^s$ fields after the end of the initial half-cycle (i.e., final state shown in Fig. 7) in the deformed RVEs for the three particle volume fractions under consideration. Figure 8a-c also shows that the magnetic self-fields under no applied $\mathbf{h}^{\mathtt{app}}$ become considerably stronger with increasing volume fraction. Furthermore, the contours of microscopic $\breve{m}_1/m_{\mathtt{p}}^s$ are shown in Fig. 8d-f, where we observe $\breve{m}_1 \approx m_{\mathtt{p}}^s$ in the particles, while $\breve{m}_1 = 0$ in the non-magnetic matrix phase. In accord with the computed effective magnetostrictions in Fig. 7b and c, we observe very small overall deformation of the RVEs, although the local (microscopic) strain fields may be much higher (twice as large) and varying extensively in the matrix phase. For instance, the contours of the local nominal strain $\breve{\lambda}_1 - 1$ fields are shown in Fig. 8g-i.

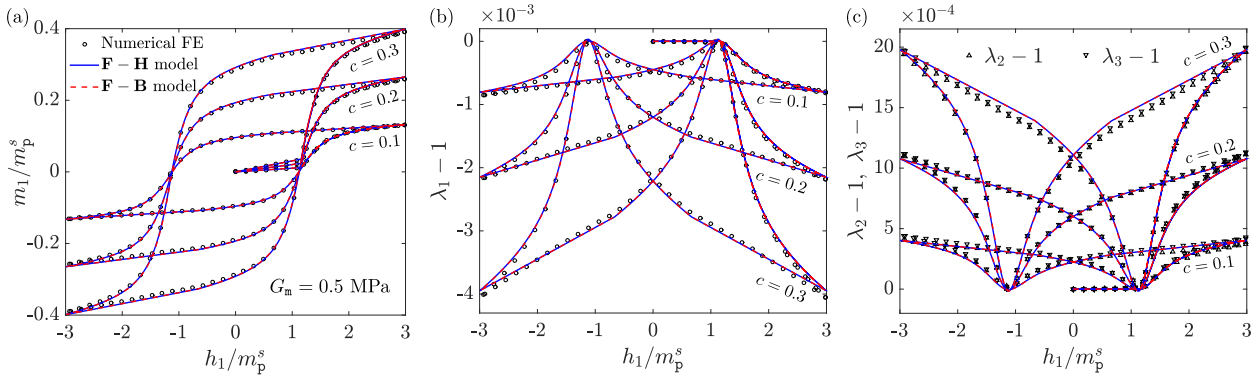

Figure 9: Comparison of the effective (a) magnetization, (b) parallel and (c) transverse magnetostriction responses from the $\mathbf{F}-\mathbf{H}$ and $\mathbf{F}-\mathbf{B}$ models with the numerical homogenization estimates for a matrix shear modulus $G_{\mathtt{m}} = 0.5$ MPa. The h-MRE is subjected to an uniaxial cyclic h-field of magnitude $|h_1| = 3m_{\mathtt{p}}^s$ and the results for three different particle volume fractions of $c = 0.1,\ 0.2$ and 0.3 are shown. The average of the effective responses computed from five realizations of a RVE are shown without the fluctuation patches for the magnetostrictions. (Taken from Mukherjee and Danas (2022)).

The magnetization and magnetostriction response under a fully reversed proportional loading is then computed for $c = 0.1,\ 0.2$ and 0.3 by considering *a single* RVE of each volume fraction. These RVEs are selected to be those, whose effective response is the closest to the corresponding average shown by the firm lines in Fig. 7b and c.

Then, the proposed $\mathbf{F}-\mathbf{H}$ and $\mathbf{F}-\mathbf{B}$ model responses are compared with the full-field numerical homogenization response in Fig. 9 for $c = 0.1,\ 0.2$ and 0.3. Here we consider a representative matrix shear modulus $G_{\mathtt{m}} = 0.5$ MPa, which corresponds to the shear modulus of the PDMS elastomer. Notice in Fig. 9a that the saturation magnetization of the h-MREs increases in an almost linear fashion with c, which resembles closely to the s-MREs responses (Lefèvre et al., 2017; Danas, 2017; Mukherjee et al., 2020). The coercivity b^c of the composite, however, undergoes very little change with the increase in c. Nonetheless, the effective susceptibilities χ^e and χ^r also increase with c,

which can be observed clearly from Fig. 9a. Overall, the model predictions for the magnetization in the h-MRE match perfectly with the numerically computed effective response.

The local magnetostriction responses, on the other hand, exhibit a butterfly-shaped hysteresis loop with the applied cyclic magnetic field (see Fig. 9b and c). This response is essentially controlled by the coupling parameter β, which is calibrated from the numerically computed magnetostriction responses and has been provided in (64). Being the closed form complementary energy density, the $\mathbf{F}-\mathbf{B}$ model does not need any further calibration. Thus, the same β parameter is used for the $\mathbf{F}-\mathbf{B}$ model, yielding excellent match with the numerical homogenization response.

In this regard, we find that the model is capable of reproducing extremely well the effective magnetic response of the h-MRE for several volume fractions. As a result of this excellent agreement, the effective magnetostriction is also well reproduced by only a single calibration constant since β is a constant for a given volume fraction c.

In addition, we note that as the volume fraction of the particles decreases, the magnetization tends to saturate faster. By contrast, the switching point controlled by the magnetic coercivity b^c of the composite seems to be almost insensitive to the particle volume fraction, which justifies the proposition (69). We further note that the calibrated β parameter in (64) is also found to predict the effective magnetostriction responses considerably well for all $G_{\mathtt{m}} \geq 0.2$ MPa. Some representative computations to probe this predicting capability of the model have been carried out. These results are not shown here for brevity.

7.1.2. Effect of $b^c_{\mathtt{p}}$ and $\chi^e_{\mathtt{p}}$

In this section, we explore theoretically the response of an h-MRE material for different values of $b^c_{\mathtt{p}}$ and $\chi^e_{\mathtt{p}}$. We consider a shear modulus for the matrix phase $G_{\mathtt{m}} = 0.3$ MPa along with the magnetic particle parameters shown in Table 3 and the coupling parameter as in (64). Moreover, we use the inverse Langevin saturation function defined in the last row of Table 1. We further control the $\mathbf{b}$ field and we impose overall

$$S^{\mathtt{mech}}_{ij} = 0, \ \forall i,j = 1,2,3, \qquad F_{ij} = 0, \quad \forall i \neq j, \qquad \mathbf{b}^{\mathtt{app}} = b_1 \mathbf{e}_1. \tag{133}$$

The choice of these parameters in the limit of vanishing dissipation, i.e., $b^c_{\mathtt{p}} \to 0$ will allow in the next section to probe the h-MRE model response against the FE results for purely energetic s-MREs with carbonyl iron particle (CIP) inclusions, obtained in Mukherjee et al. (2020).

Table 3: Magnetic properties of the CIP particles in h-MRE formulation in Section 4

$\chi^e_{\mathtt{p}}$	$\chi^r_{\mathtt{p}}$	$\mu_0 m^s_{\mathtt{p}}$ (T)	$b^c_{\mathtt{p}}$ (T)	μ_0 (μN $\cdot$ A^2)
$(0, 0.2, 0.4$	30.0	2.5	$0.05, 0.5, 1$	$4\pi 10^{-1}$

Specifically, Fig. 10 shows the prediction of the h-MRE models (recall that both versions $\mathbf{F}-\mathbf{H}$ and $\mathbf{F}-\mathbf{B}$ are equivalent) for three values of $b^c_{\mathtt{p}} = 0.05, 0.5, 1$T and $\chi^e_{\mathtt{p}} = 0$. It is plain from those graphs, that as $b^c_{\mathtt{p}} \to 0$ dissipation reduces to zero for all variables shown. Perhaps more interestingly, the internal variable $\boldsymbol{\mathcal{H}}^r$ becomes anhysteretic too. In fact, we have that $\boldsymbol{\mathcal{H}}^r = -\mathbf{m}$ when $\chi^e_{\mathtt{p}} = 0$. More importantly, it takes non-zero values in the limit $b^c_{\mathtt{p}} \to 0$.

When $\chi^e_{\mathtt{p}}$ is not zero, as shown in Fig. 11, $\boldsymbol{\mathcal{H}}^r$ is directly linked to $\mathbf{m}$ but is not equal to $-\mathbf{m}$. Moreover, in the same figure, we observe that the parameter $\chi^e_{\mathtt{p}}$ controls the unloading slope of the h-MRE. It was shown in Mukherjee and Danas (2019) that NdFeB powders have

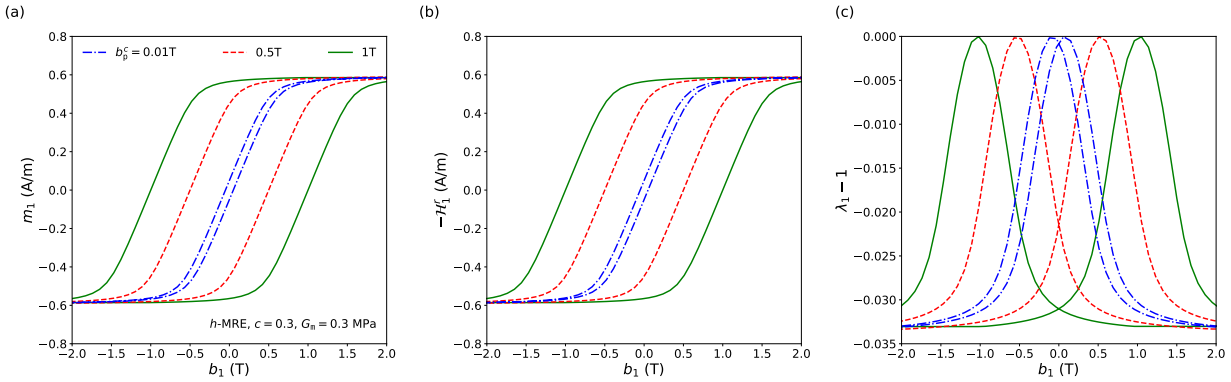

Figure 10: Comparison of the (a) magnetization m_1, (b) (minus) internal variable $-\mathcal{H}_1^r$ and (c) magnetostriction response $\lambda_1 - 1$ as predicted by the h-MRE model for three values of $b_{\mathrm{p}}^c = 0.05, 0.5, 1\mathrm{T}$, $\chi_{\mathrm{p}}^e = 0$, particle volume fraction $c = 0.3$ and matrix shear modulus $G_{\mathrm{m}} = 0.3\mathrm{MPa}$.

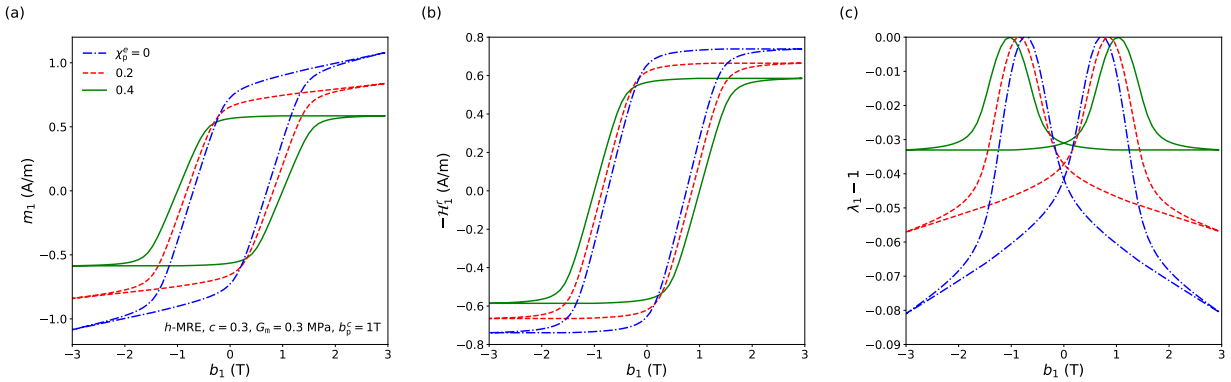

Figure 11: Comparison of the (a) magnetization m_1, (b) (minus) internal variable $-\mathcal{H}_1^r$ and (c) magnetostriction response $\lambda_1 - 1$ as predicted by the h-MRE model for three values of $\chi_{\mathrm{p}}^e = 0., 0.2, 0.4$, coercivity $b_{\mathrm{p}}^c = 1\mathrm{T}$, particle volume fraction $c = 0.3$ and matrix shear modulus $G_{\mathrm{m}} = 0.3\mathrm{MPa}$.

values of χ_{p}^e that range between $0.01 - 0.2$. This of course has important implications on the corresponding magnetization value upon complete removal of the external magnetic field as well as the corresponding magnetostriction which can reach much higher values when χ_{p}^e is large.

Remark 15. It is interesting to remark at this point that in essence, the magnetization variable may be seen as some form of *an internal variable* in the general dissipative model and not an independent one, as it is usually assumed in the literature (Brown, 1966; James and Kinderlehrer, 1993; Kankanala and Triantafyllidis, 2004; Danas et al., 2012). The reason is that $\mathbf{m}$ is directly related to the internal variable $\boldsymbol{\mathcal{H}}^r$ introduced originally in Mukherjee et al. (2021). This interpretation is in fact consistent with the fact that no boundary conditions can be imposed on $\mathbf{m}$ and thus no differential constraints. By contrast, an internal variable serves exactly that purpose, i.e., in addition to describe dissipation in the present context, it may be used to provide a measure of the internal state of the material similar to plastic strain in elasto-plasticity or polarization in electro-elasticity. In fact, the mechanism itself of magnetic domain motion inducing an internal state of magnetization or polarization may be thought in similar terms as the dislocation motion causes an internal state of plasticity. Another example of such a variable is the stress polarization

in Hashin-Shtrikman estimates and again in that setting the stress polarization can exhibit jumps along interfaces or boundaries. This makes these polarization/magnetization variables powerful quantities to establish sometimes analytical approximate results. Nevertheless, they are not able to describe the material state entirely since either $\mathbf{B}$ or $\mathbf{H}$ still needs to be used so that actual boundary conditions can be imposed in a BVP. Finally, when only the energetic response of the material is analyzed the use of magnetization is in the general sense unnecessary.

7.1.3. The limit of zero dissipation

Following the previous analysis, we now set $b_c = 10^{-6}$ and $\chi^e_{\mathtt{p}}$, keeping the remaining parameters presented in Table 3 and assess the h-MRE models by comparison with the FE results of (Mukherjee et al., 2020), which correspond to purely energetic s-MRE simulations. We plot the numerical FE response along with the model magnetization and magnetostriction responses in Fig. 12a and b,c, respectively. Besides the excellent agreement between the numerical homogenization computations

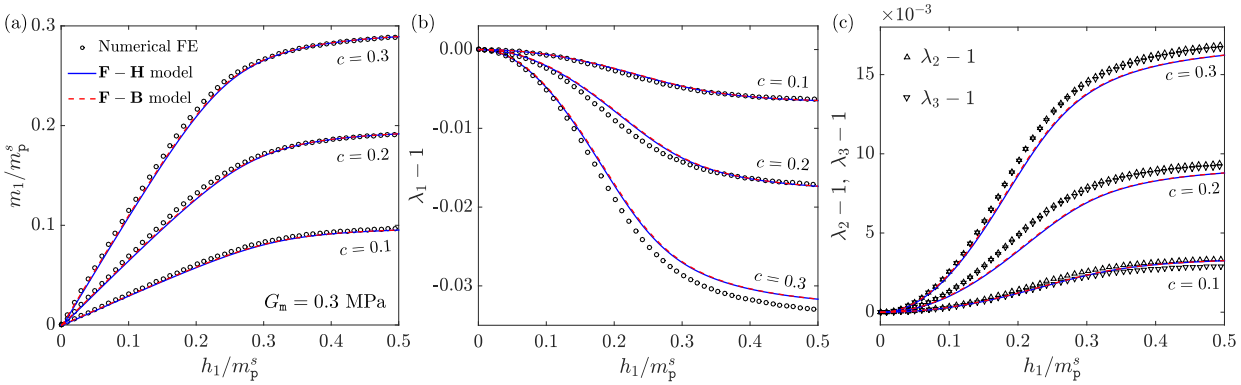

Figure 12: Comparison of the (a) magnetization, (b) parallel and (c) transverse magnetostriction responses from the $\mathbf{F}-\mathbf{H}$ and $\mathbf{F}-\mathbf{B}$ models with the numerical homogenization estimates. The s-MRE is subjected to an uniaxial cyclic h-field of magnitude $|h_1| = 0.5m^s_{\mathtt{p}}$ and the results for three different particle volume fractions of $c = 0.1,\ 0.2$ and 0.3 are shown. (Taken from Mukherjee and Danas (2022)).

and the model predictions, we observe two key differences between the s- and h-MREs by comparing Figs. 9 and 12. Firstly, and the obvious is the absence of hysteresis in the s-MREs. Secondly, s-MREs tend to saturate at a lower applied h_1, while h-MREs saturate very slowly to a constant magnetization. This is in agreement with the corresponding s-MRE experiments of Danas et al. (2012) as well as those presented in Mukherjee and Danas (2019) for hard magnets.

7.2. Magnetization independent of stretching in MREs

7.2.1. Uniaxial tension perpendicular to pre-magnetization

In this section, we apply a purely mechanical uniaxial tension loading along the $\mathbf{e}_2$ direction, which is perpendicular to the direction $\mathbf{e}_1$ of the pre-magnetization of the h-MRE, while the applied magnetic field is kept identically zero, i.e.,

$$S^{\mathtt{mech}}_{22} \neq 0, \quad S^{\mathtt{mech}}_{11} = S^{\mathtt{mech}}_{33} = 0, \quad F_{ij} = 0, \quad \forall i \neq j, \quad \mathbf{h}^{\mathtt{app}} = \mathbf{0}.$$

As shown in the inset of Fig. 13a, we consider half a cycle, described by a linear increase of $S_{22}^{\mathtt{mech}}$ from 0 to $G_{\mathtt{m}}$ and subsequent decrease to 0 (note that the rate of loading is inconsequential since the models under study are rate-independent). Moreover, we show results for three shear moduli, $G_{\mathtt{m}} = 0.3, 0.5, 1.0$.

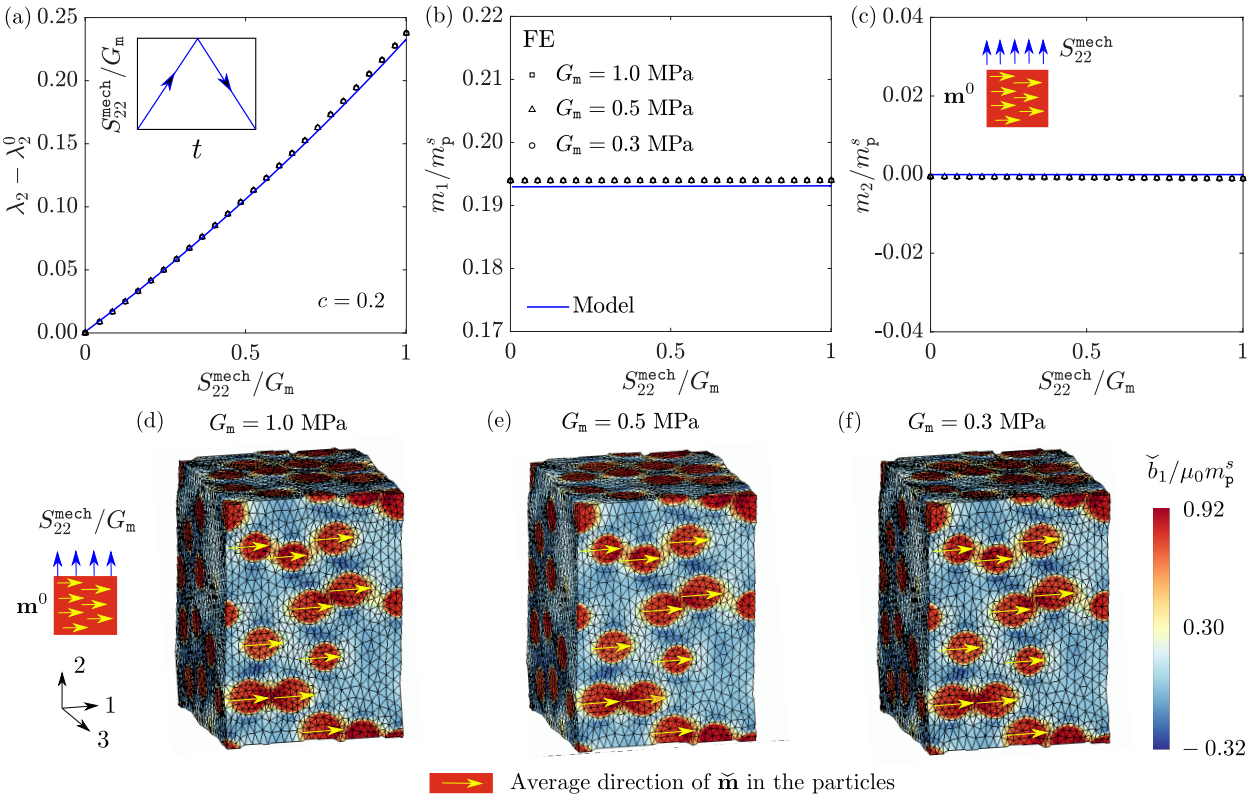

Figure 13: Evolutions of (a) mechanical stretch $\lambda_2 - \lambda_2^0$ (with λ_2^0 denoting the initial remanent stretch due to the pre-magnetization) and magnetizations along (b) $\mathbf{e}_1$ and (c) $\mathbf{e}_2$ under applied uniaxial tensile stress $S_{22}^{\mathtt{mech}}$, whose temporal evolution is shown in the inset of (a). The inset of (c) shows a schematic of the h-MRE with the direction of pre-magnetization $\mathbf{m}^0$ and the applied uniaxial tension. Contours of the $\breve{\mathbf{b}}$ field in the deformed RVE under applied $S_{22}^{\mathtt{mech}}/G_{\mathtt{m}} = 1$ for $G_{\mathtt{m}} =$ (d) 1.0, (e) 0.5 and (f) 0.3 MPa. The arrows on the particles show the average direction of $\breve{\mathbf{m}}$ in them. (Taken from Mukherjee et al. (2021)).

Fig. 13a, b and c show the mechanical stretch λ_2 and the magnetizations along the $\mathbf{e}_1$ and $\mathbf{e}_2$ directions for the numerical RVE and the analytical model. The corresponding deformed RVEs are depicted in Fig. 13d-f. It is noted that the numerically computed effective stretch $\lambda_2 - \lambda_2^0$ (with λ_2^0 denoting the initial remanent stretch due to the pre-magnetization) *does fluctuate* with the different RVE realizations. Nevertheless, as shown in Fig. 7, the magnitude of such realization-dependent scatter in the strain remain less than 5×10^{-4}, which is considerably smaller than the magnitude of the stretch (~ 0.25), shown in Fig. 13a. Thus, the numerical computations with the monodisperse RVEs lead to excellent estimates under purely mechanical loading conditions, while at the same time, they keep the computational expense considerably low. This observation has already been done in the context of s-MREs by Danas (2017), where the mechanical and magnetic response was found to converge for RVEs of considerably lower number of particles, whereas the pure magnetostriction (i.e. for zero overall applied mechanical load) required substantially larger RVE sizes with more particles.

In particular, we observe excellent agreement between the numerical homogenization results and the model estimates in all cases shown in Fig. 13a-c, namely, the principle stretch λ_2 and the effective magnetization responses along $\mathbf{e}_1$ and $\mathbf{e}_2$. The model predictions for the transverse stretches λ_2 and λ_3 also match perfectly the numerically computed responses (not shown explicitly here). It is noted further that all results shown here are independent of the matrix shear modulus upon the normalization $S_{22}^{\mathtt{mech}}/G_{\mathtt{m}}$. This is a particular feature of the Neo-Hookean model used for the mechanical description of the matrix phase and simply implies that the overall response of the h-MRE is also of a Neo-Hookean type at least to a very good approximation (see relevant discussion in Lopez-Pamies et al. (2013)).

Remark 16. Finally, we close the discussion of Fig. 13 with an important observation, that of the *stretch-independence* of the current effective remanent magnetization $\mathbf{m}^0$, observed in Fig. 13b,c, as predicted by the model and confirmed by the RVE simulations. In simple words, we find that the current remanent magnetization remains unaffected by the stressing (or stretching) of the solid. As a result, the mechanical cyclic loading of a pre-magnetized h-MRE does not lead to dissipation. This does not mean that the local magnetization does not change via corresponding particle rearrangement. On the contrary, particles rearrange due to the finite straining. Nonetheless, this does not affect the average current magnetization amplitude of the RVE, which is an important feature that needs to be reproduced both by phenomenological top-down as well as homogenization bottom-up models. The ability of the present model to recover this feature is linked to the definition of the internal variable $\boldsymbol{\mathcal{H}}^r$ in the intermediate stretch-free configuration as discussed in Section 4.1 and the corresponding choice of invariants and coupled energy proposed. In turn, this feature has also been observed in the context of s-MREs experimentally (Danas et al., 2012), numerically (Mukherjee et al., 2020) and theoretically (Lefèvre et al., 2017) via an independence of the current magnetization response to pre-stressing. This feature is linked also to the underlying (quasi-)incompressibility of the materials under study and should be taken into account in the modeling of MREs in general. We also note that the same response is observed if the tension is parallel to the pre-magnetization direction (not shown here).

Remark 17. We further remark that this observation of the stretch independence of magnetization amplitude in incompressible MREs has been very recently confirmed by Yan et al. (2023) (but see also Yan et al. (2021a)) experimentally by pressurizing (and thus pre-stretching) thin plates. These authors have then proposed a modification of the original Zhao et al. (2019) theory. In particular, they have proposed that the current magnetization $\mathbf{m}$ is evaluated in terms of the pre-magnetization (reference) state $\mathbf{m}^0$ as $\mathbf{m} = \mathbf{R}\mathbf{m}^0$, instead of $\mathbf{m} = \mathbf{F}\mathbf{m}^0$. Given the direct connection between $\boldsymbol{\mathcal{H}}^r$ and $\mathbf{m}$ shown in Fig. 10, this is equivalent to the present proposition of $\boldsymbol{\mathcal{H}}^r$ being stretch-independent and defined in the intermediate configuration (see Fig. 2).

To go a step further, it is rather straightforward to consider a thought example, where a saturated pre-magnetized h-MRE along direction 1 (i.e. $m_1^0 = m^s$) is subjected to a stretch along direction 1, i.e., $F_{11} > 1$. By using the original proposition, $\mathbf{m} = \mathbf{F}\mathbf{m}^0$, it would simply imply that the current magnetization $m_1 = F_{11}m_1^0 > m^s$ is (much) larger than the saturation magnetization of the h-MRE, which is practically and theoretically impossible. On the contrary, $\mathbf{m} = \mathbf{R}\mathbf{m}^0$ would simply lead to $m_1 = m_1^0 = m^s$, a result that is theoretically consistent and as was shown numerically and experimentally is the case for incompressible s- and h-MREs.

7.2.2. Simple shear parallel to pre-magnetization

We apply a purely mechanical simple shear stress $S_{12}^{\mathtt{mech}}$ loading. The corresponding traction vector is parallel to the pre-magnetization direction $\mathbf{e}_1$ of the h-MRE, while the applied magnetic field is kept identically zero during this step, i.e.,

$$S_{12}^{\mathtt{mech}} \neq 0, \quad S_{11}^{\mathtt{mech}} = S_{22}^{\mathtt{mech}} = S_{33}^{\mathtt{mech}} = 0, \quad \mathbf{h}^{\mathtt{app}} = \mathbf{0},$$

together with $F_{21} = F_{13} = F_{31} = F_{23} = F_{32} = 0$. Furthermore, the evolution for the applied $S_{12}^{\mathtt{mech}}$ is shown in the inset of Fig. 14a.

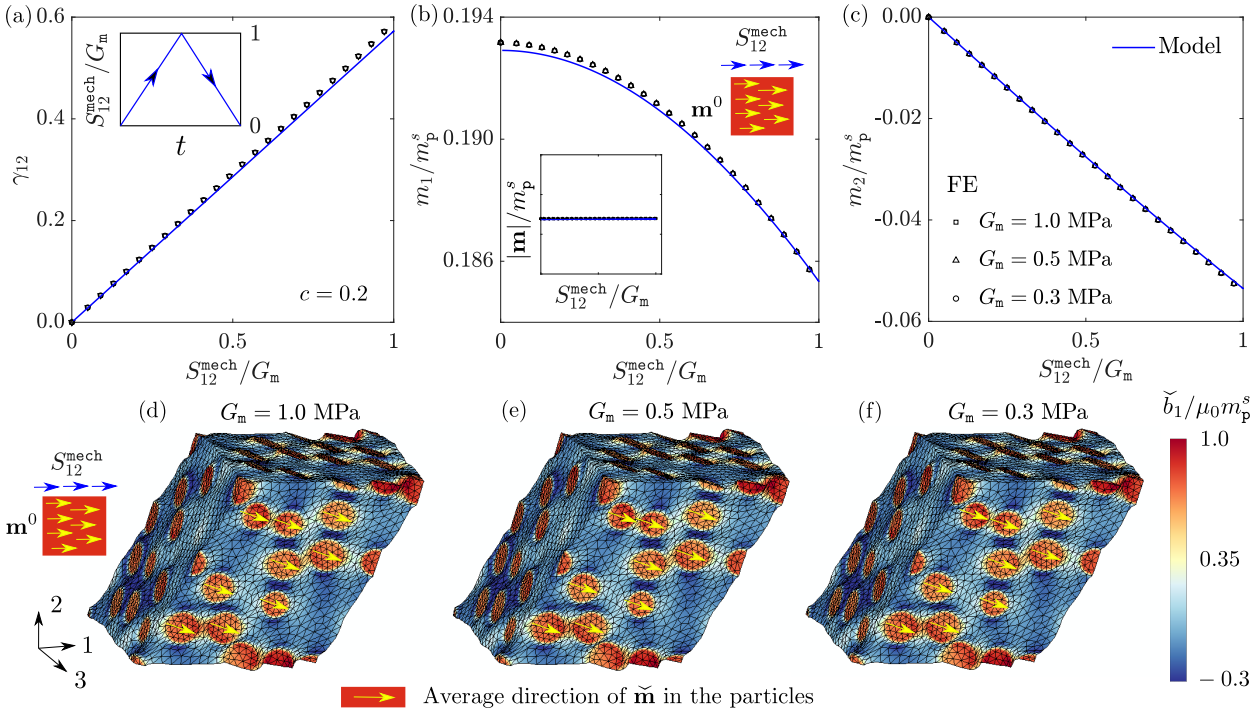

Figure 14: Evolutions of (a) shear strain γ_{12} and magnetizations along (b) $\mathbf{e}_1$ and (c) $\mathbf{e}_2$ under applied simple shear stress $S_{12}^{\mathtt{mech}}$, whose loading path is shown in the inset of (a). A schematic of the h-MRE with the direction of pre-magnetization $\mathbf{m}^0$ and the applied shear stress is shown in the inset of (b). Contours of the $\breve{\mathbf{b}}$ field in the deformed RVE under applied $S_{12}^{\mathtt{mech}}/G_{\mathtt{m}} = 1$ for $G_{\mathtt{m}} =$ (d) 1.0, (e) 0.5 and (f) 0.3 MPa. The arrows on the particles show the average direction of $\breve{\mathbf{m}}$ in them. (Taken from Mukherjee et al. (2021)).

In Fig. 14a-c, we observe an excellent agreement between the model predictions and the numerical homogenization results for the effective shear strain $F_{12} = \gamma_{12}$ as well as for the effective magnetizations along $\mathbf{e}_1$ and $\mathbf{e}_2$, respectively. All results, shown in the context of this figures, are independent of the matrix shear modulus upon the normalization $S_{12}^{\mathtt{mech}}/G_{\mathtt{m}}$.

Again, we observe that despite the significant shearing strains and particle rearrangements, the amplitude of the current effective magnetization $\mathbf{m}$ remains unaffected (see inset of Fig. 14b). Instead, the orientation of the magnetization vector significantly changes with the applied shearing, as revealed by the change of the individual components $m_1/m_{\mathtt{p}}^s$ and $m_2/m_{\mathtt{p}}^s$ in Fig. 14b and c, respectively. Interestingly, this rotation remains (almost) identical to the macroscopic (average) rotation of the RVE induced by the shearing. Therefore, the affine rotation-based model presented in this work (as well as that of Yan et al. (2023)) predicts the evolution of $\mathbf{m}$ in this case accurately.

Figures 14d-f show three deformed RVEs at $S_{12}^{\mathtt{mech}}/G_{\mathtt{m}} = 1$ for the three $G_{\mathtt{m}}$ under consideration. It is noted that the RVE deformations and the local $\breve{b}_1$ fields remain identical for all three $G_{\mathtt{m}}$ under

consideration. The only key feature to note here is the uniform distribution of the particle rotations, which, in turn, rotates the local (microscopic) and therefore the global (effective) magnetization vectors.

7.3. NdFeB-based h-MRE versus CIP-based s-MRE response

In this section, we provide a useful set of results that serve to discuss practical differences between actual h-MREs with NdFeB particles and s-MREs with CIP particles. In the very recent literature, an impressive amount of studies has focused mainly on h-MREs subjected to small magnetic fields at their fully pre-magnetized state. While this state exploits mainly magnetic torques in slender objects, it is only a small fraction of the response of the more general class of MRE materials and potential application (see for instance Moreno-Mateos et al. (2022); Garcia-Gonzalez et al. (2023)). We use for simplicity the same inverse Langevin saturation function defined in the last row of Table 1 for both h- and s-MRE results shown next. This changes only slightly the transition response of h-MREs but not the initial and final saturation response. In order to cover a variety of effects, we will include in the following also pre-stress effects. In the work of Danas et al. (2012) related to CIP-filled s-MREs, it was shown that the magnetization response is almost entirely insensitive to the pre-stress. In contrast, a strong effect of the pre-applied mechanical load was observed for the magnetostriction. In the following, we will consider various combinations of the pre-stresses. The magnetic field is always applied along direction 1, i.e., $\mathbf{b} = b_1\mathbf{e}_1$, and the matrix phase has a shear modulus $G_{\mathtt{m}} = 0.05$MPa.

In this regard, we analyze first in Fig. 15 the effect of uniaxial pre-stressing parallel to the applied magnetic field, such that

$$S_{11}^{\mathtt{mech}} = \{-1, 0, 1\}, \quad S_{22}^{\mathtt{mech}} = S_{33}^{\mathtt{mech}} = 0, \quad F_{ij} = 0, \quad \forall i \neq j, \quad \mathbf{b} = b_1\mathbf{e}_1.$$

We note first that the pre-stress has no effect on the magnetization response in Fig. 15a. This is consistent with the early work of Danas et al. (2012) on s-MREs, while we observe that the same feature is true for the h-MREs too. Moreover, the CIP-based s-MRE has a much higher saturation magnetization and initial permeability than that for the NdFeB. This allows for the s-MRE material to reach much higher magnetostrictive strains and at smaller magnetic fields as clearly shown in Fig. 15b. In turn, the h-MRE exhibits important dissipative effects and much lower magnetostrictive strains. Similarly, as a direct consequence of this feature, the s-MRE is expected to exhibit a stronger "magnetorheological" effect (i.e., increase in the apparent shear or Young's modulus) upon the application of a magnetic field (Diguet et al., 2021). In turn, the h-MRE retains a permanent magnetization in the absence of an applied magnetic field and thus is more relevant for torque-based or permanent magnetic applications. We also observe that tensile pre-stresses increase the resulting amplitude of the magnetostriction (which remains always negative in this homogenization analysis), while compressive ones lead to a decrease of $|\Delta\lambda_1|$. This observation is the same for both MREs considered here.

We close the section by considering in Fig. 16, magnetostriction curves for (a) the CIP-based s-MRE and (b) NdFeB h-MRE for three sets of triaxial pre-stress values

$$(S_{11}^{\mathtt{mech}}, S_{22}^{\mathtt{mech}})/G_{\mathtt{m}} = (0,1)|(1,1)|(1,0), \qquad S_{22}^{\mathtt{mech}}/G_{\mathtt{m}} = S_{33}^{\mathtt{mech}}/G_{\mathtt{m}},$$
$$F_{ij} = 0, \quad \forall i \neq j, \qquad \mathbf{b} = b_1\mathbf{e}_1.$$

Specifically, Fig. 16a,b shows that uniaxial tension pre-stressing along the magnetic field leads to higher amplitude of magnetostrictive strains than tension along the perpendicular direction. A

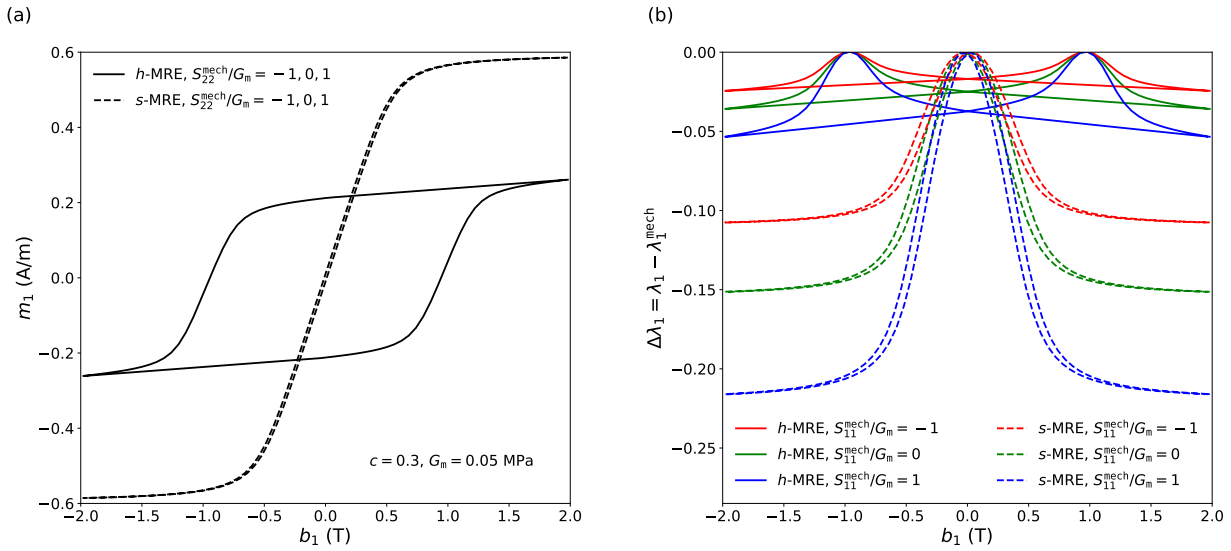

Figure 15: Comparison of the (a) magnetization and (b) magnetostriction response using the material properties defined in Table 2 for the h-MRE with NdFeB particles and Table 3 for the s-MRE with CIP particles. Three uniaxial prestress values $S_{11}^{\mathtt{mech}}/G_{\mathtt{m}} = \{-1,\ 0,\ 1\}$ are considered along the applied magnetic field. We set the particle volume fraction to $c = 0.3$ and matrix shear modulus $G_{\mathtt{m}} = 0.05$MPa. Magnetostriction in this figure is defined as the magnetically induced strain minus the mechanical strain induced by the mechanical prestress, i.e. $\Delta\lambda_1 = \lambda_1 - \lambda_1^{\mathtt{mech}}$.

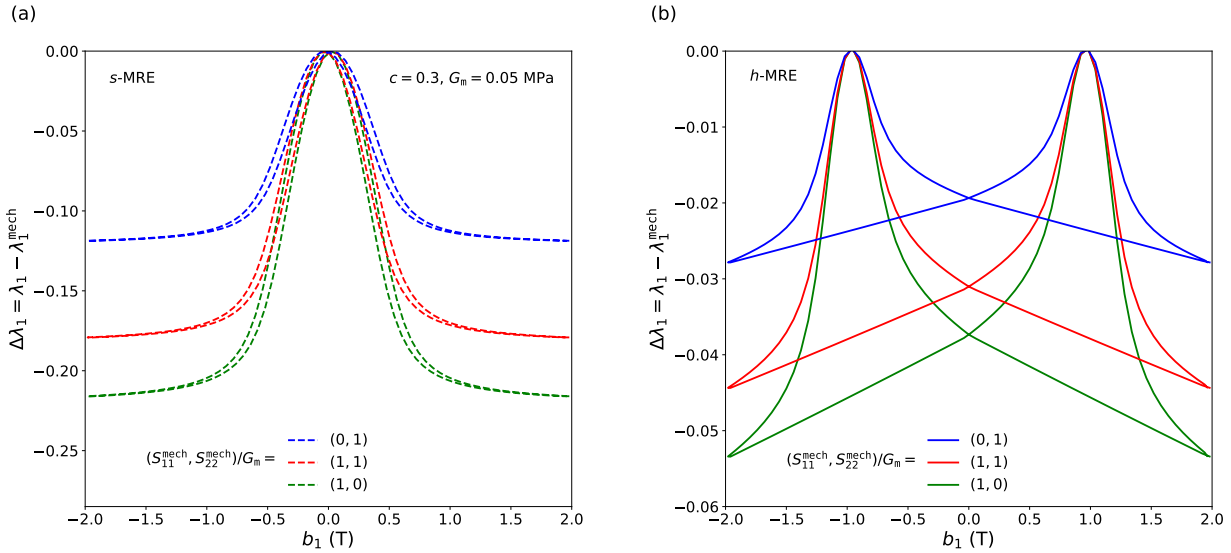

Figure 16: Comparison of the magnetostriction response using the material properties defined (a) in Table 3 for the s-MRE with CIP particles and (b) in Table 2 for the h-MRE with NdFeB particles. Three prestress sets of values $(S_{11}^{\mathtt{mech}}, S_{22}^{\mathtt{mech}})/G_{\mathtt{m}} = (1,0)|(1,1)|(0,1)$ are considered. We set the particle volume fraction to $c = 0.3$ and matrix shear modulus $G_{\mathtt{m}} = 0.05$MPa. Magnetostriction in this figure is defined as the magnetically induced strain minus the mechanical strain induced by the mechanical prestress, i.e. $\Delta\lambda_1 = \lambda_1 - \lambda_1^0$.

hydrostatic tension pre-stress leads to a magnetostriction $\Delta\lambda_1$ that lies in-between the two. This figure reveals clearly the strong effect of pre-stress upon the magnetostriction and by extension to the magnetorheological effect, which would be present if instead of pre-stressing a pre-straining

was applied. Again, the magnetization is not affected in this case by the pre-stresses and is the same with that shown in Fig. 15.

7.4. Energetic s-MRE models versus h-MRE models with zero dissipation

In Section 4, we have provided a unified modeling framework for isotropic, incompressible hard and soft MREs. The latter is obtained by considering the limit of $b_{\mathrm{p}}^{c} \to 0$. However, in practice this limit is rather difficult to consider analytically since in that limit $\boldsymbol{\mathcal{H}}^{r}$ becomes a nonlinear function of $\mathbf{H}$ or $\mathbf{B}$, depending on which formulation one uses.

An alternative purely energetic approach, which however, was introduced earlier than the full dissipative one, has been discussed in Section 5 and originally presented in Mukherjee et al. (2020). This approach is not dual as already discussed in the aforementioned section but, nonetheless, provides both an $\mathbf{F}-\mathbf{H}$ and $\mathbf{F}-\mathbf{B}$ model that are close to each other. In the original work of Mukherjee et al. (2020), those models were calibrated against the analytical, implicit homogenization model of Lefèvre et al. (2017). As it was shown in that work, while the proposed models (all of them by construction) do well for CIP volume fractions of $c \leq 0.2$, they tend to underestimate the magnetostriction (but not the magnetization) response for $c > 0.25$ when compared with corresponding FE periodic results. In the present manuscript, we have introduced the new function (92) to fix this discrepancy.

Table 4: Magnetic properties of the CIP particles in s-MRE formulation in Section 5

χ_{p}	$\mu_0 m_{\mathrm{p}}^{s}$ (T)	μ_0 ($\mu\mathrm{N}\cdot\mathrm{A}^2$)
30.0	2.5	$4\pi 10^{-1}$

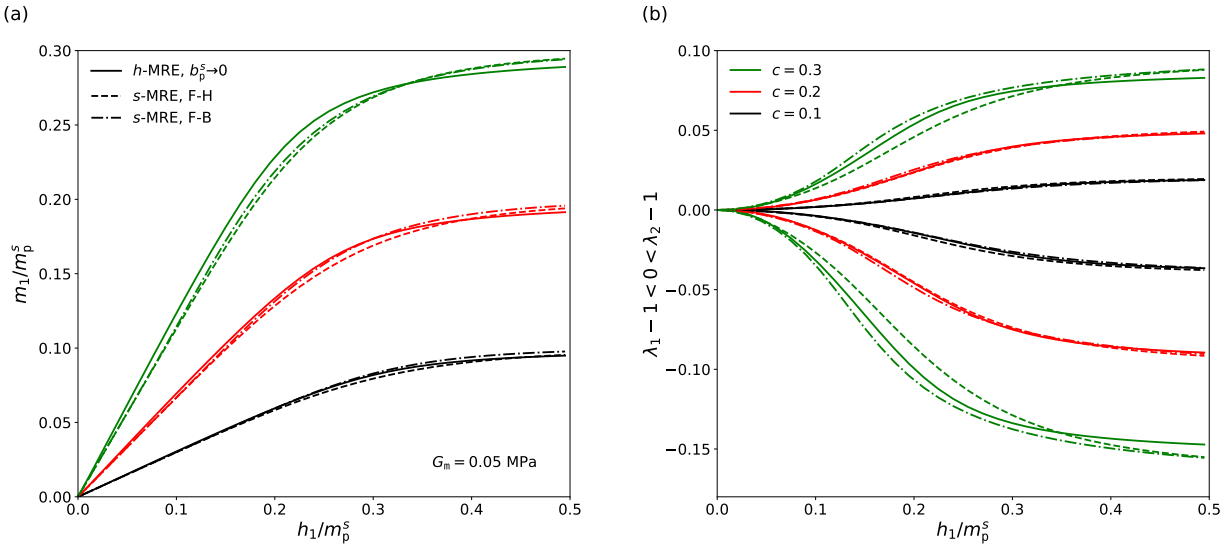

Figure 17: Comparison of the (a) magnetization and (b) magnetostriction response as predicted by the s-MRE models discussed in Section 5 and the reference h-MRE models at the limit of $b_{\mathrm{p}}^{c} \to 0$ for three particle volume fractions $c = 0.1,\ 0.2$ and 0.3 and matrix shear modulus $G_{\mathrm{m}} = 0.05$MPa.

In view of this, we provide in Figs. 17 and 18 a comparison between the results obtained previously in the case of vanishing dissipation by the h-MRE model with $b_{\mathrm{p}}^{c} \to 0$ and the s-MRE models presented in Section 5. For the s-MRE models we use the parameters provided in Table 4.

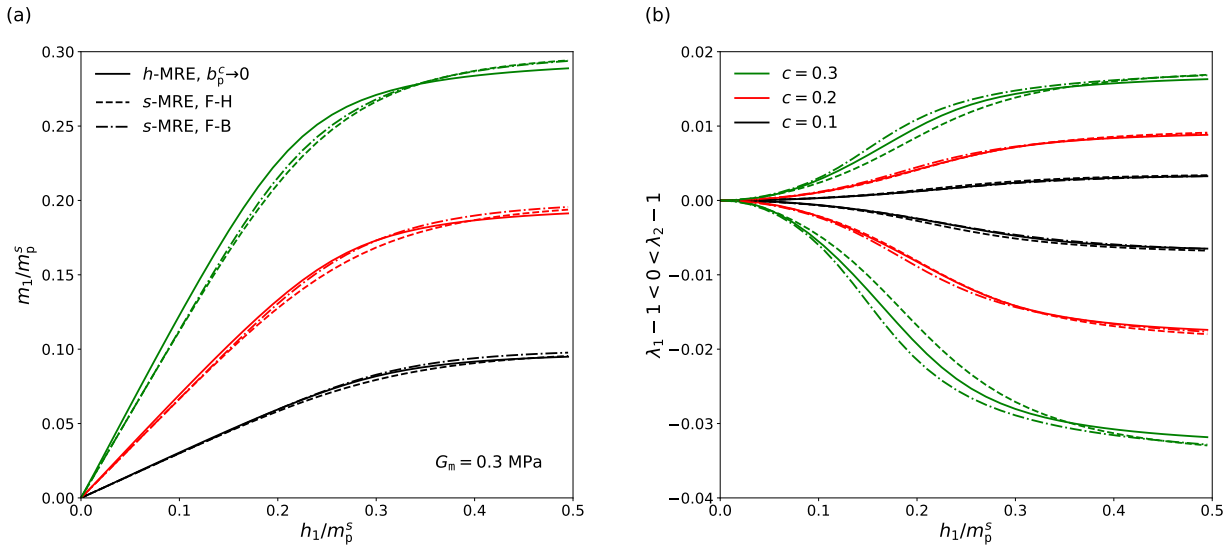

Figure 18: Comparison of the (a) magnetization and (b) magnetostriction response as predicted by the s-MRE models discussed in Section 5 and the reference h-MRE models at the limit of $b_p^c \to 0$ for three particle volume fractions $c = 0.1,\ 0.2$ and 0.3 and matrix shear modulus $G_m = 0.3$MPa.

In particular, we observe that for both matrix moduli $G_m = 0.05,\ 0.3$ MPa considered here as an example, all models lie fairly close to each other. Moreover, we observe no dependence of the magnetization response on the moduli of the matrix phase. The h-MRE model is considered as the reference case given its excellent agreement with the FE simulations discussed in the previous section. In this view then, the $\mathbf{F} - \mathbf{H}$ ($\mathbf{F} - \mathbf{B}$) s-MRE model tends to slightly underestimate (overestimate) the magnetostriction amplitude at large volume fractions (e.g., $c = 0.3$). In turn, the s-MRE models in general underestimate slightly the magnetization response. For volume fractions $c \leq 0.2$, the agreement between all models is excellent. In this regard, we conclude in this study that any of the above models may be used to model s-MREs depending on the problem at hand and convenience. Obviously, the purely energetic s-MRE models are easier to implement since they do not require any definition of internal variables or incremental procedures (as described in the general case in Section 6).

8. Results: Numerical BVP simulations

This section shows numerically computed boundary value problem (BVP) solutions for s-MREs as well as uniformly and non-uniformly pre-magnetized h-MRE beams. The following results make use of the previously discussed models, which are numerically implemented in user-element Abaqus subroutines and consider the soft and hard particle magnetization parameters as in Tables 4 and 2, respectively. The particle volume fraction c and the loading conditions for pre-magnetization and/or actuation steps are discussed under specific subsections depending on the examples analyzed. Moreover, the specific Dirichlet boundary conditions on $\mathbf{u}_\tau$, φ_τ and α_τ, i.e, the case-specific versions of the admissible sets $\mathcal{U}$ in (108), $\mathcal{G}$ in (109) and $\mathcal{B}$ in (112), respectively, are detailed in the following.

8.1. Generic numerical BVP setting

The discretization of the scalar and vector potential-based variational principles were discussed in a fairly general setting so far in Section 6. We now specify a geometry for the numerical BVP of interest. Although the MREs are finding applications in a wide variety of engineering devices, such as in actuators, most of the recent attention is in fabrication and testing of slender structures, which find applications in soft robotic devices (Kim et al., 2018; Ren et al., 2019) as well as in thin membranes or films (Psarra et al., 2017, 2019; Moreno-Mateos et al., 2022). This includes spatially uniformly and non-uniformly pre-magnetized beams, functionally graded beams with a distribution of the particle volume fractions c, as well as films resting substrates.

In particular, we consider a representative (but otherwise generic) two-dimensional, plane-strain analysis of the bending of pre-magnetized slender beams. We emphasize in this context, that the magnetic fields are applied via the fixed electromagnet poles far away from the MRE (not modeled explicitly here), both during the pre-magnetization and actuation. Thus, it is necessary to embed the MREs in a surrounding air. Moreover, since the magnetic fields are applied far away (or at a given distance), the air domain is considered to be substantially larger than the MRE. In particular, let us consider the air domain length $L > \ell$ (e.g. ten times larger) to ensure that the MRE deflection is sufficiently far from the boundary of the air $\partial\mathcal{V}_{\text{Air}}^{\text{Top}} \cup \partial\mathcal{V}_{\text{Air}}^{\text{Right}} \cup \partial\mathcal{V}_{\text{Air}}^{\text{Bottom}} \cup \partial\mathcal{V}_{\text{Air}}^{\text{Left}}$ (see Fig. 19a).

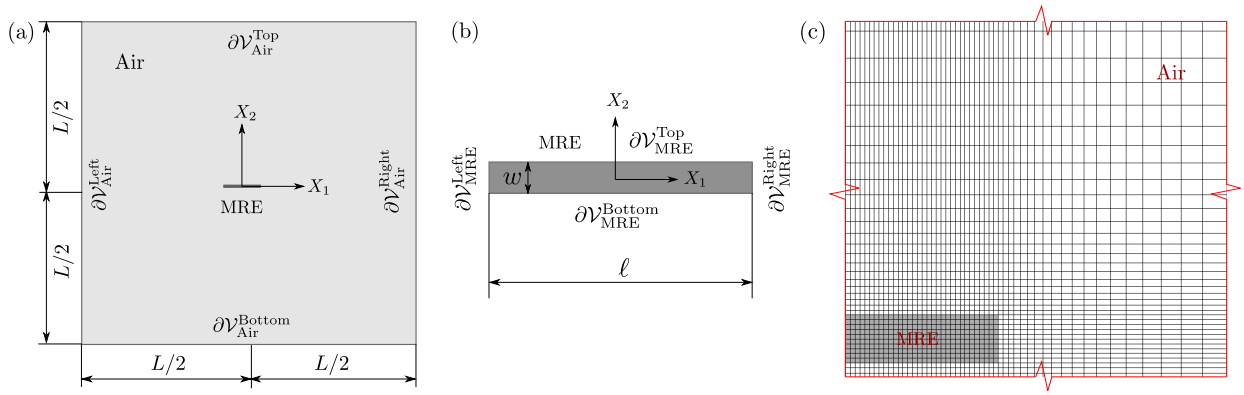

Figure 19: (a) Diagram of the full BVP domain having MRE and the surrounding air. The air domain with an external boundary $\partial\mathcal{V}_{\text{Air}}^{\text{Top}} \cup \partial\mathcal{V}_{\text{Air}}^{\text{Right}} \cup \partial\mathcal{V}_{\text{Air}}^{\text{Bottom}} \cup \partial\mathcal{V}_{\text{Air}}^{\text{Left}}$ is considered to be a square of length L. The reference coordinate system $\mathbf{X}$ is considered to have origin at the center of the air domain. (b) Dimensions of the MRE having the interface $\partial\mathcal{V}_{\text{MRE}}^{\text{Top}} \cup \partial\mathcal{V}_{\text{MRE}}^{\text{Right}} \cup \partial\mathcal{V}_{\text{MRE}}^{\text{Bottom}} \cup \partial\mathcal{V}_{\text{MRE}}^{\text{Left}}$ with the surrounding air. The MRE length ℓ is considered to be $\ell = 0.1L$ and the aspect ratio of the MRE is defined as $r_{\text{asp}} = \ell/w$. (c) A part of the structured mesh considered in the calculations. Standard linear 4-node quadratic isoparametric elements are employed. (Taken from Mukherjee and Danas (2022)).

As shown in Fig. 19b, the slender MRE beam of length ℓ and width w has a common interface $\partial\mathcal{V}_{\text{MRE}}^{\text{Top}} \cup \partial\mathcal{V}_{\text{MRE}}^{\text{Right}} \cup \partial\mathcal{V}_{\text{MRE}}^{\text{Bottom}} \cup \partial\mathcal{V}_{\text{MRE}}^{\text{Left}}$ with the surrounding air. The aspect ratio of the beam is hence defined via $r_{\text{asp}} = \ell/w$. Finally, the structured FE mesh used in the computations is shown in Fig. 19c. Throughout this paper we consider linear four-node quadrilateral isoparametric elements in the FE computations.

8.2. Treatment of air

The air surrounding the MRE has (nearly) zero mechanical stiffness, whereas the magnetic $\mathbf{b}$ and $\mathbf{h}$ fields in it are finite. Specifically, the former is related to the latter via $\mathbf{b} = \mu_0\mathbf{h}$ in the

surrounding air. Dealing with a material of nearly zero mechanical stiffness in the present fully implicit, Lagrangian modeling framework leads to extreme mesh distortions at the corners of the MRE, eventually stopping the numerical simulation from converging.

Till this date, a number of methods have been implemented for dealing with the surrounding air in the magneto-active structures. The most straightforward way to model the air is to consider it a nearly incompressible or compressible hyperelastic solid having shear modulus of ~ 1 Pa (Rambausek and Keip, 2018; Dorn et al., 2021). However, such an assumption may lead to an underestimation of the mechanical deformations of the MREs, specifically when undergoing large deformations or deflections. An alternative approach, namely, the method of constraining the motion of the air nodes surrounding the MRE is found to yield very accurate results of MRE deformations in air (Psarra et al., 2019; Mukherjee et al., 2021). In particular, the latter considers the air shear modulus to be zero but simultaneously applies linear constraints on all nodes in the air domain to make them move according to the deformation/deflection of the MRE boundary. Having said that, we also remark that the application of such linear constraints on the air nodes, where two or more (magnetic or non-magnetic) structures are interacting, may become difficult to implement properly so that numerical convergence is achieved. A quantitative comparison of the performance of different modeling approaches for the surrounding air is drawn in a recent paper (Rambausek et al., 2022). Two additional promising approaches, not discussed here, have been proposed only recently in Rambausek and Schöberl (2023), where a proper treatment of the Maxwell stress at the interface between the magnetoelastic solid and the air allows to eliminate the spurious modes present in such problems and allow for very good convergence. Another potential solution to the problem could be the use of meshfree methods (see for instance Kumar et al. (2019)). Therein, it was shown that very large strains may be reached at soft regions of the domain in a straightforward manner. Nonetheless, those methods are not yet available in more general-use software packages and thus their use is less visited.

In this paper, we consider standalone MRE solids that are subjected to spatially uniform magnetic fields, as shown in Fig. 19a. Thus, we employ the air node constraining method to model the deformation in the domain $\mathcal{V}_{\text{Air}}$. In fact, the linear constraints on the displacement field $\mathbf{u}$ for all $\mathbf{X} \in \mathcal{V}_{\text{Air}}$ can be applied via directly augmenting the incremental variational principles (106) and (110) by a penalty energy

$$W_{\texttt{penalty}}(\mathbf{u}) = \sum_{j=1}^{N_{\text{Air}}} \sum_{i=1}^{2} \frac{G_{\texttt{c}}}{2L_{\texttt{c}}\zeta} \left(\mathcal{C}_i^{(j)}\right)^2, \tag{134}$$

where N_{Air} is the number of air nodes, $L_{\texttt{c}}$ is a reference length parameter usually considered to be equal to w, $G_{\texttt{c}}$ is an arbitrary shear modulus that we consider to be identical to that of the matrix and ζ is the penalty parameter, which is set to 10^{-3}. Nevertheless, any value of ζ in the range $10^{-6} - 10^{-3}$ ensures a proper imposition of the constraint, not affecting the numerical convergence significantly. Given that those constraints are linear one has also the option to directly use the `*Equation` command in Abaqus. Such an approach has also been tested showing no differences with the penalty approach described here in two and three dimensions. Finally, the pointwise constraint $\mathcal{C}_i^{(j)}$ is defined as (Psarra et al., 2019)

$$\mathcal{C}_i^{(j)} \equiv \begin{cases} d_i^{(j)} u_i^{(j)}\Big|_{\partial\mathcal{V}_{\text{MRE}}} - u_i^{(j)}\Big|_{\mathcal{V}_{\text{Air}}} = 0, & \text{if } \; 0 < d_i^{(j)} \leq 1 \\ u_i^{(j)}\Big|_{\mathcal{V}_{\text{Air}}} = 0, & \text{otherwise,} \end{cases} \tag{135}$$

which ties the displacement of any node j in $\mathcal{V}_{\text{Air}}$ with that of its nearest node on the Air/MRE interface $\partial\mathcal{V}_{\text{MRE}}$. In practice, we construct a set of two-node elements comprising one node from $\mathcal{V}_{\text{Air}}$ and one from the set $\partial\mathcal{V}_{\text{MRE}}$ that has the least Euclidean distance from the former. Subsequently, we add the "force" and "stiffness" terms to the global force and stiffness matrices. Those terms emerge by considering first and second variations of the corresponding degrees-of-freedom involved the penalty energy (134).

The constraint "weight" function $d_i^{(j)}$ is defined in terms of the absolute distance difference between the X_i $(i = 1, 2)$ coordinates of the points in $\mathcal{V}_{\text{Air}}$ and on $\partial\mathcal{V}_{\text{MRE}}$, such that

$$d_i^{(j)} = 1 - \frac{\left| X_i^{(j)}\big|_{\mathcal{V}_{\text{Air}}} - X_i^{(j)}\big|_{\partial\mathcal{V}_{\text{MRE}}} \right|}{R_f L/2}, \qquad \text{with} \quad i = 1, 2. \tag{136}$$

Here, $R_f \in (0.5, 1]$ is a fraction coefficient that is user-defined and serves to prescribe the range of the deformable air. The air nodes lying outside that region are simply fixed and are not allowed to displace. The penalty energy (134) may be added directly to the general variational principles (106) or (110) or simply impose the linear constraints (135) via an elimination technique (such as the `*Equation` command in Abaqus).

8.3. Magnetostriction and magnetization response of a spherical s-MRE specimen

In this section, we show qualitative results for the ideal problem of an s-MRE spherical specimen embedded in a large spherical air domain as shown in Fig. 20a. A remotely applied magnetic field induces magnetostrictive strains and magnetization inside the inclusion. This problem has been the focus of various studies starting from the seminal manuscript of Brown (1966), who proposed a solution in the small strain setting. Therein, he has shown that the presence of a magnetically-induced traction, i.e., the magnetic part of the Maxwell stress (see for instance equation (103)) leads to non-uniform mechanical fields in the magneto-elastic inclusion. Here, we recall the analysis carried out in Lefèvre et al. (2017) and Lefèvre et al. (2019) in the context of finite strains. This is only possible numerically.

We follow the approach of Lefèvre et al. (2017) wherein, for computational expediency, numerical solutions in the specimen and surrounding space —assumed to be air — are generated on a spatial domain of sufficiently large but finite extent, and not on $\mathbb{R}^3$ entirely. While full details of this approach can be found in Section 6 in (Lefèvre et al., 2017), it is appropriate to mention here that (i) the finite domain of computation is comprised of the spherical MRE specimen surrounded by an air-filled thick spherical shell subjected on its external surface to the affine boundary conditions $\mathbf{x} = \mathbf{X}$ and $\varphi = -\mathbf{H}_\infty \cdot \mathbf{X}$ (see Fig. 20(a)), (ii) the surrounding air is treated as a highly compressible magnetoelastic material with vanishingly small mechanical stiffness, and (iii) the numerical solutions are generated by means of a conforming axisymmetric 7-node hybrid triangular finite element discretization that leverages the axial symmetry of the problem around the direction, say $\mathbf{e}_3$, of the applied magnetic field $\mathbf{H}_\infty = H_\infty \mathbf{e}_3$.

By providing *pointwise* solutions for the deformation and magnetic fields in the MRE specimen and surrounding air, this approach also allows to extract *global* information about the deformation and magnetization of the specimen as would be done experimentally (Diguet et al., 2010; Diguet, 2010).

Figure 21 presents contour plots in the $\mathbf{e}_1$-$\mathbf{e}_3$ plane of the local component $F_{33}(\mathbf{X})$ of the deformation gradient and of the local component $m_3(\mathbf{x})$ of the magnetization over spherical specimens

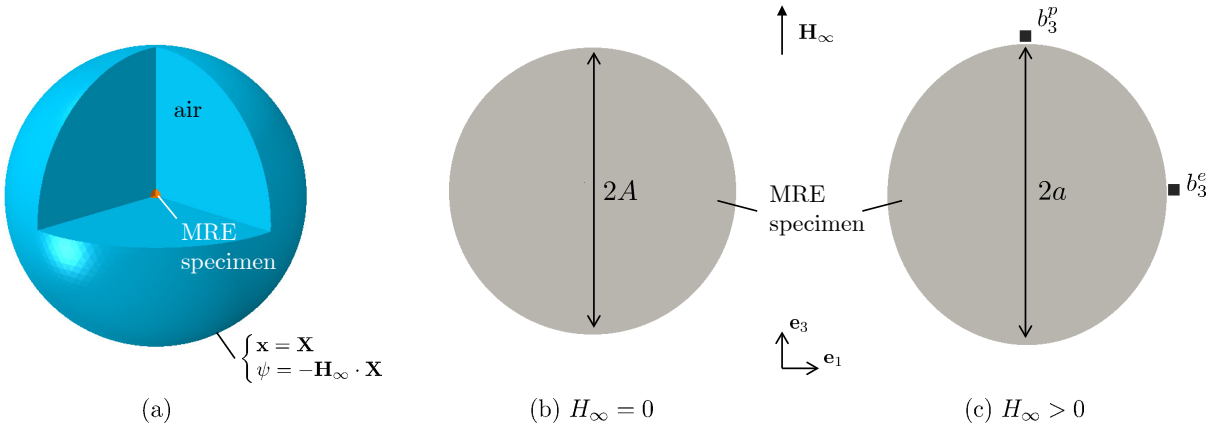

Figure 20: (a) Schematic of the finite domain utilized to generate numerical solutions for the BVP of a s-MRE sphere embedded in air. The air domain is defined by a spherical shell of initial outer radius that is twenty times that of the MRE specimen. Schematics of a spherical MRE specimen of initial radius A in its (b) undeformed and (c) deformed configuration. (Taken from Lefèvre et al. (2019)).

made of s-MREs containing $c = 0.222$ volume fraction of CIP particles. We use the same material properties for the CIP particles introduced in Table 4, while the matrix phase is taken with a shear modulus $G_{\mathtt{m}} = 50$kPA. The contours in Fig. 21a-c are shown over the undeformed configuration of the specimen as implied by the argument $\mathbf{X}$ of $F_{33}(\mathbf{X})$, while the contours in Fig. 21d-e are shown over the deformed configuration of the specimen as implied by the argument $\mathbf{x}$ of $m_3(\mathbf{x})$. Further, the contours correspond to the magnitudes $H_\infty = 0.5,\ 1.0,\ 1.5$ MA/m of the remotely applied magnetic field $\mathbf{H}_\infty$, and the color scale bars in each of them indicate the corresponding variation of the quantity of interest from its minimum to its maximum.

It is also clear from Figs. 21a-c that the local deformation gradient is highly heterogeneous, with regions in tension in the core of the specimen and regions in compression at its poles. In turn, Fig. 21d-e indicate that the local magnetization is practically uniform across the specimen, at least for the range of strains obtained in the current case. This implies that the material magnetization response of the s-MRE can be accurately measured using probes at its boundary (see for instance experimental setup in Bodelot et al. (2017)); the same is *not* true in general for cylindrical specimens (Bodelot et al., 2017; Lefèvre et al., 2017). In that case, all fields are highly heterogeneous. This implies that most experimental results available in the literature should be analyzed with extreme caution by theoreticians who attempt to propose material models, since the experimental measurements involve significant structural effects that sometimes are predominant over the corresponding material response.

8.4. Uniformly pre-magnetized h-MRE cantilever beams

In the following two sections, we consider h-MREs with matrix shear modulus $G_{\mathtt{m}} = 0.187$ MPa, which resembles closely that of the moderately-soft PDMS elastomers (Kim et al., 2018; Zhao et al., 2019). Moreover, the matrix bulk modulus is considered to be $G'_{\mathtt{m}} = 500 G_{\mathtt{m}}$, which ensures a *nearly incompressible* material response.

We start with the simplest case of the uniformly pre-magnetized cantilever beams with the aspect ratios $r_{\text{asp}} = 10$ and 17.5. Specifically, we simulate the experimental observations of Zhao

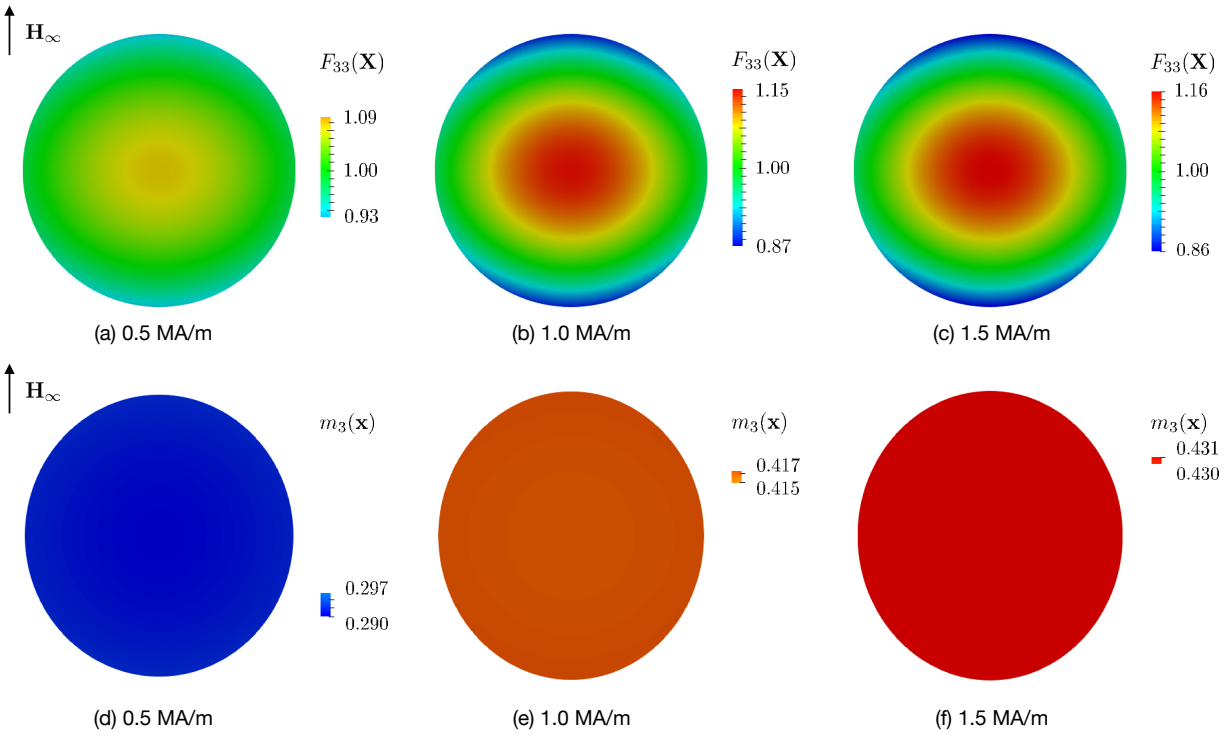

Figure 21: Contour plots of (a)–(c) the component $F_{33}(\mathbf{X})$ of the deformation gradient over the *undeformed* configuration, and (d)-(e) the component $m_3(\mathbf{x})$ of the magnetization over the deformed configuration of a spherical specimen made of a s-MRE containing $c = 0.222$ volume fraction of iron particles. The contours correspond to the remotely applied magnetic field $\mathbf{H}_\infty = H_\infty \mathbf{e}_3$ with H_∞=0.5, 1.0, 1.5 MA/m. (Taken from Lefèvre et al. (2019)).

et al. (2019) for the deflection of pre-magnetized h-MREs under uniform transverse actuation fields. To accomplish that, the loading is divided in two steps, which are detailed in the following.

- `Step-I`: First, we carry out the pre-magnetization along $\widehat{\mathbf{E}}_1$ by considering the air and MRE boundaries to be fixed. Thus, the Dirichlet boundary conditions on $\mathbf{u}$ and φ for the $\mathbf{F}-\mathbf{H}$ model reads

$$\mathbf{u}_\tau = \mathbf{0}, \ \forall \ \mathbf{X} \in \partial\mathcal{V}_{\text{MRE}}, \ \text{and} \ \ \mathbf{u}_\tau = \mathbf{0}, \ \forall \ \mathbf{X} \in \partial\mathcal{V}_{\text{Air}} \tag{137}$$

$$\varphi_\tau = 0, \quad \forall \ \mathbf{X} \in \partial\mathcal{V}_{\text{Air}}^{\text{Left}}, \ \text{and} \ \varphi_\tau = -\frac{b_{1,\tau}^{\mathtt{mag}}}{\mu_0} L, \quad \forall \ \mathbf{X} \in \partial\mathcal{V}_{\text{Air}}^{\text{Left}}, \tag{138}$$

  where $b_{1,\tau}^{\mathtt{mag}}$ is the magnetization field at time τ. In particular, $b_{1,\tau}^{\mathtt{mag}}$ is increased linearly in time up to 2 T followed by its decrease at the same rate to 0T. The rate of $b_{1,\tau}^{\mathtt{mag}}$ (and all the following applied fields) is inconsequential in the simulations since the material model is rate-independent. Similarly, the Dirichlet boundary condition on α for the $\mathbf{F}-\mathbf{B}$ model reads

$$\alpha_\tau = 0, \quad \forall \ \mathbf{X} \in \partial\mathcal{V}_{\text{Air}}^{\text{Bottom}} \quad \text{and} \quad \alpha_\tau = b_{1,\tau}^{\mathtt{mag}} L, \quad \forall \ \mathbf{X} \in \partial\mathcal{V}_{\text{Air}}^{\text{Top}}, \tag{139}$$

  while that on $\mathbf{u}_\tau$ remains identical to (137).

- `Step-II`: Next, we carry out the actuation step, where we apply a uniform field $b_2^{\mathtt{actu}}$ along $\widehat{\mathbf{E}}_2$, i.e., transverse to the centerline of the beam. The magnitude of $b_2^{\mathtt{actu}}$ is increased mono-

tonically from 0 T. The specific Dirichlet boundary conditions on $\mathbf{u}_\tau$ and φ_τ in this step for the $\mathbf{F}-\mathbf{H}$ model reads

$$\mathbf{u}_\tau = \mathbf{0},\ \forall\ \mathbf{X} \in \partial\mathcal{V}_{\text{MRE}}^{\text{Left}},\quad \text{and } \mathbf{u}_\tau = \mathbf{0},\quad \forall\ \mathbf{X} \in \partial\mathcal{V}_{\text{Air}} \tag{140}$$

$$\varphi_\tau = 0,\ \forall\ \mathbf{X} \in \partial\mathcal{V}_{\text{Air}}^{\text{Bottom}},\ \text{and } \varphi_\tau = -\frac{b_{2,\tau}^{\mathtt{actu}}}{\mu_0}L,\quad \forall\ \mathbf{X} \in \partial\mathcal{V}_{\text{Air}}^{\text{Top}}. \tag{141}$$

In turn, the boundary condition on α in this step for the $\mathbf{F}-\mathbf{B}$ model computations reads

$$\alpha_\tau = 0,\ \forall\ \mathbf{X} \in \partial\mathcal{V}_{\text{Air}}^{\text{Left}},\ \text{and } \alpha_\tau = -b_{2,\tau}^{\mathtt{actu}}L,\ \forall\ \mathbf{X} \in \partial\mathcal{V}_{\text{Air}}^{\text{Right}}. \tag{142}$$

In addition, we choose to work with a particle volume fraction of $c = 0.177$, which is identical to that of the fabricated h-MREs by Zhao et al. (2019). Moreover, we consider $G_{\mathtt{m}} = 0.187$ MPa, which leads to an effective shear modulus $G = 0.303$ MPa for the composite. In fact, the latter is experimentally measured by Zhao et al. (2019) for the h-MREs with $c = 0.177$.

In agreement to the experimental observations, the computations show the pre-magnetized h-MREs to deflect immediately under the applied $b_2^{\mathtt{actu}}$. The end-tip deflections of the pre-magnetized cantilevers with an increasing $b_2^{\mathtt{actu}}$ is plotted in Fig. 22a for $r_{\text{asp}} = 10$ and 17.5. Therein, we

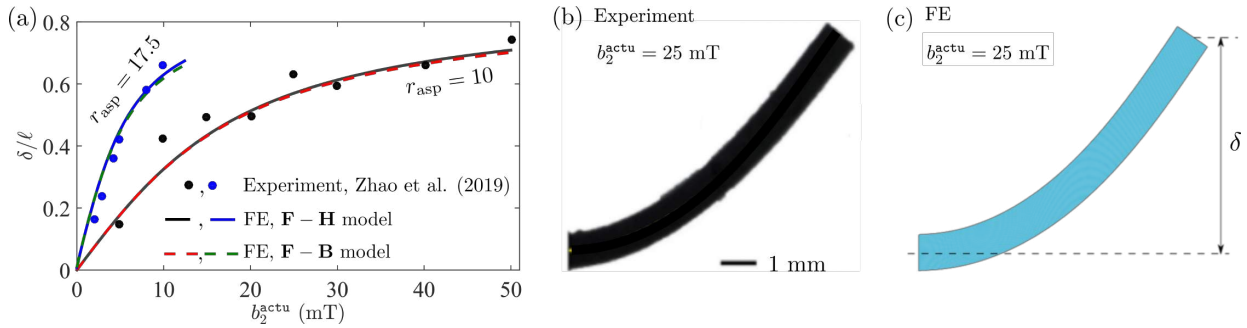

Figure 22: (a) Comparison of the experimentally measured and the model (both $\mathbf{F}-\mathbf{H}$ and $\mathbf{F}-\mathbf{B}$) predicted end-tip deflections of the pre-magnetized cantilever beams of $r_{\text{asp}} = 10$ and 17.5 under the applied actuation field along $\mathbf{e}_2$. Comparison of the FE predicted deflected beam shape with the respective experimental measurements of Zhao et al. (2019) under $b_2^{\mathtt{actu}} = 25$ mT for (b) $r_{\text{asp}} = 10$ and (c) 17.5. (Taken from Mukherjee and Danas (2022)).

observe that the $\mathbf{F}-\mathbf{H}$ and $\mathbf{F}-\mathbf{B}$-based numerical simulations yield identical responses, which also agree with the experimentally measured end-tip deflection values for the two aforementioned aspect ratios. Moreover, the experimentally captured deflected shape in Fig. 22b, which is of the cantilever beam having $r_{\text{asp}} = 10$ under $b_2^{\mathtt{actu}} = 25$ mT agrees excellently with its numerically computed counterpart in Fig. 22c. The FE solutions are carried out via writing an user-defined element (UEL) and coupling it with the ABAQUS/Standard solver.

The contours of the magnetic $\mathbf{b}$, $\mathbf{h}$ and $\mathbf{m}$ field magnitudes along with the arrows showing their directions in and around the pre-magnetized h-MRE cantilever of $r_{\text{asp}} = 17.5$ are shown in Fig. 23. Specifically, we show the contours under $b_2^{\mathtt{actu}} = 0$ mT and $b_2^{\mathtt{actu}} = 12.5$ mT in Figures 23a-c and d-f, respectively. Notice from Fig. 23b that the $\mathbf{h}$ field in the pre-magnetized cantilever is considerably smaller than the $\mathbf{b}$ and $\mathbf{m}$ fields in it. Thus, one can approximate the remanent b-field,i.e., the b-field in the h-MRE after pre magnetization as shown in Fig. 23a, to be $\mathbf{b}^r \approx \mu_0\mathbf{m}$. This is, in fact, the key feature upon which the magnetic torque-based models (Kim et al., 2018; Zhao et al., 2019) for the pre-magnetized h-MREs are based. Such simple approximations, however, do not

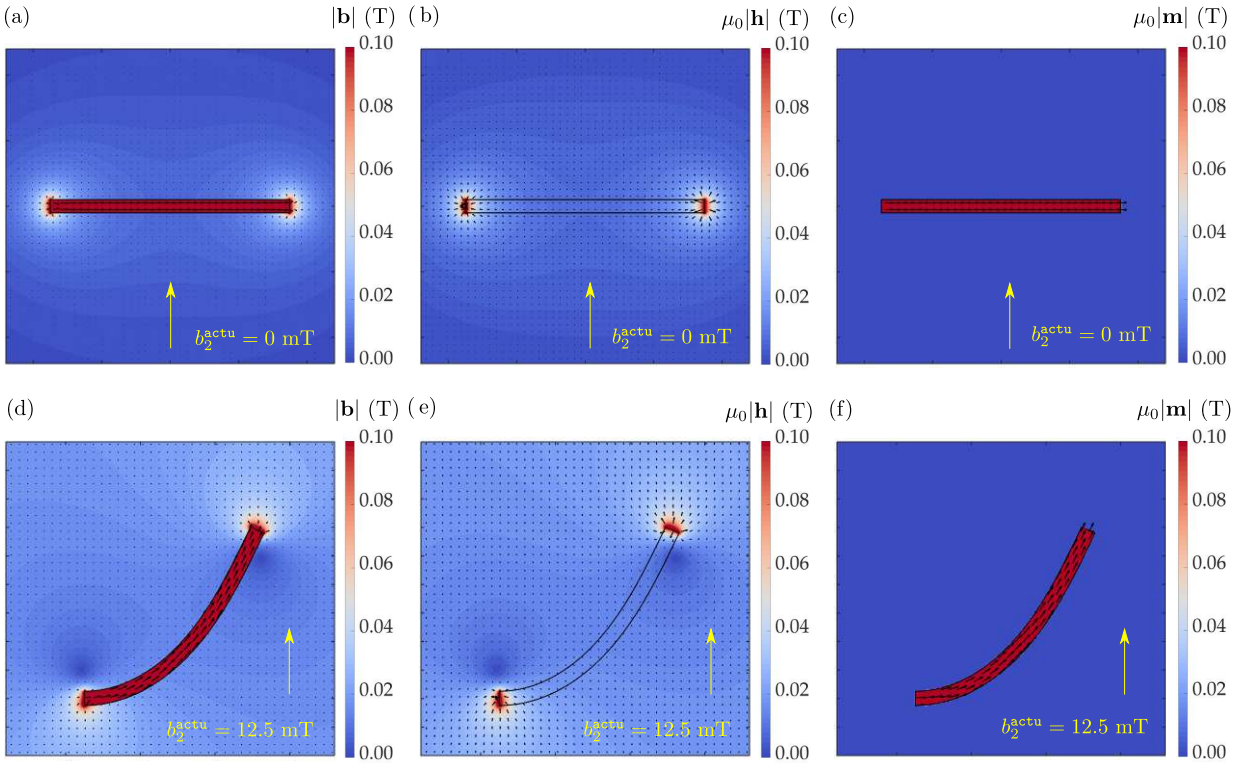

Figure 23: Contours of the (a,d) $|\mathbf{b}|$, (b,e) $|\mathbf{h}|$ and (c,f) $|\mathbf{m}|$ fields in and around a pre-magnetized h-MRE cantilever of $r_{\text{asp}} = 17.5$, (a-c) before and (d-f) after the application of an actuation field $b_2^{\texttt{actu}} = 12.5$ mT along $\widehat{\mathbf{E}}_2$. The black colored arrows are used to indicate the direction of the respective vector fields. The length of the arrows are scaled according to the magnitude of the respective vectors. (Taken from Mukherjee and Danas (2022)).

hold in general for the cases of non-uniform pre-magnetization or the hybrid h-/s-MRE beams. Specific examples of the hybrid hybrid h-/s-MRE beams and non-uniform pre-magnetization will be discussed later in this section.

The contours in and around the deflected h-MRE under $b_2^{\texttt{actu}} = 12.5$ mT in Figures 23d-f show that the magnetic self fields (both, $\mathbf{b}$ and $\mathbf{h}$ but not $\mathbf{m}$, which is 0 in the air) around it get perturbed by the external field application and the mechanical deformation of the beam. The remanent $\mathbf{b}$ and $\mathbf{m}$ fields in the h-MRE, however, only undergo rotation with a negligible change in their magnitudes. Clearly, the applied field $b_2^{\texttt{actu}} = 12.5$ mT, which results in such a rapid deflection of the cantilever, is too weak to alter the remanent magnetization direction. Thus, in spite of being a dissipative material in general, such very low field deflections of the pre-magnetized beams leads to a highly reversible structural response, hence, making them an ideal candidate for the remotely-actuated soft robots (Ren et al., 2019; Alapan et al., 2020; Lucarini et al., 2022a).

8.5. Non-uniformly pre-magnetized, functionally-graded h-MRE cantilever beams

The increasing trend in the development of remotely-actuated locomotion of mili-robotic structures necessitates the employment of non-uniformly pre-magnetized h-MREs, exhibiting preferential deflections patterns depending on the actuation field directions (Ren et al., 2019; Alapan et al., 2020). Motivated from these recent applications, we employ the proposed incremental variational

framework in the investigation of non-uniformly pre-magnetized h-MREs, specifically towards their pre-magnetization patterns and actuation performances.

In particular, we consider a slender h-MRE beam with $r_{\text{asp}} = 20$, $G_{\text{m}} = 0.187$ MPa and profile it according to the configurations shown in Fig. 24a and b before applying the pre-magnetization field along $\widehat{\mathbf{E}}_2$. Depending on this pre-magnetization profiling, the h-MREs are categorized into two, namely, $\mathcal{S}_1$ and $\mathcal{S}_2$, as indicated on Fig. 24a and b. Moreover, we consider two more types of

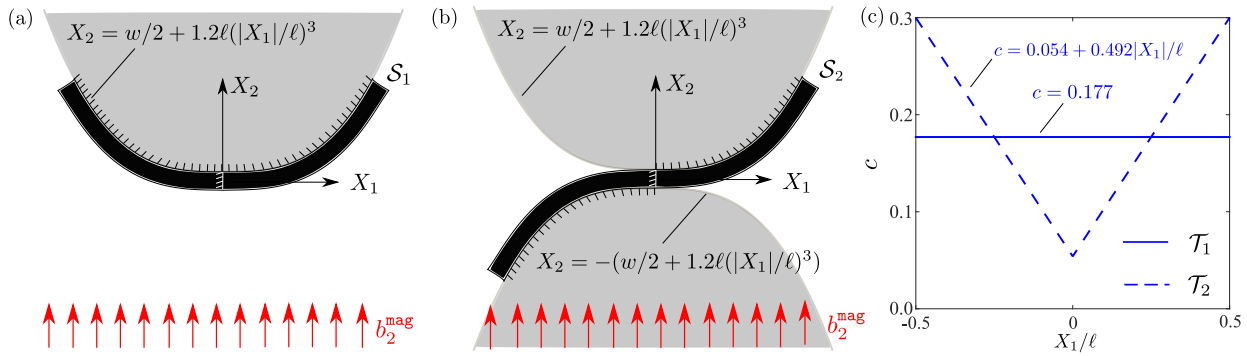

Figure 24: (a,b) Pre-magnetization profiles along the magnetizing field b_2^{mag} direction for the h-MRE beams of $r_{\text{asp}} = 20$. The profile $\mathcal{S}_1$ in (a) is considered to be the mirror image with respect to X_2 axis, whereas, $\mathcal{S}_2$ in (b) is considered to be the mirror image with respect to both, X_1 and X_2. (c) Volume fraction distribution profiles, namely, $\mathcal{T}_1$ and $\mathcal{T}_2$, along the length of the beam. (Taken from Mukherjee and Danas (2022)).

h-MREs, namely, $\mathcal{T}_1$ and $\mathcal{T}_2$, depending on the spatial distribution of the particle volume fraction. In particular, we consider a constant $c = 0.177$ for type $\mathcal{T}_1$, while a linearly varying c along the reference coordinate X_1 so that $c = 0.054 + 0.492|X_1|/\ell$ for the type $\mathcal{T}_2$ (see Fig. 24c). Notice that the *cumulative volume* of the hard-magnetic particles are considered to be identical in $\mathcal{T}_1$ and $\mathcal{T}_2$, so that the areas under both the curves in Fig. 24c remain identical. Hence, we investigate the transverse actuation response of four distinct pre-magnetized h-MREs, namely, $\mathcal{S}_i\mathcal{T}_j$, where $i, j \equiv 1, 2$.

Evidently, the initial profiling of the h-MRE beams and their release after the pre-magnetization necessitates a couple of additional steps of mechanical loading compared to the examples presented in Sections 8.4. These steps read

- `Step-I`: First, the profiling of the undeformed to the pre-magnetization shapes are performed by applying a prescribed displacement $\mathbf{u}_\tau = \mathbf{u}_\tau^{\text{Top}}$ for all $\mathbf{X} \in \partial\mathcal{V}_{\text{MRE}}^{\text{Top}}$ for $\mathcal{S}_1$ and $\mathbf{u}_\tau = \mathbf{u}_\tau^{\text{Top}}$ for all $\mathbf{X} \in \partial\mathcal{V}_{\text{MRE}}^{\text{Top}}$, $X_1 > 0$ and $\mathbf{u}_\tau = \mathbf{u}_\tau^{\text{Bottom}}$ for all $\mathbf{X} \in \partial\mathcal{V}_{\text{MRE}}^{\text{Bottom}}$, $X_1 < 0$ for $\mathcal{S}_2$ [8]. In addition, we set $\mathbf{u}_\tau = \mathbf{0}$ for all $\mathbf{X} \in \partial\mathcal{V}_{\text{Air}}$ and for all $\mathbf{X} \in \mathcal{V}_{\text{MRE}}$ if $X_1 = 0$, i.e., the displacements of the central vertical section of the beam are also blocked.

- `Step-II`: Next, the pre-magnetization is carried out along $\widehat{\mathbf{E}}_2$ in terms of applying a suitable Dirichlet boundary condition on φ_τ similar to Section 8.4. Moreover, the temporal profile and amplitude of $(b_2^{\text{mag}})_\tau$ remains identical to that of $(b_1^{\text{mag}})_\tau$ in Section 8.4.

[8] In practice, we employ the "DISP" subroutine of ABAQUS, which apply an user-defined displacement in terms of the *current coordinates*. We thus define the displacements $u_1^{\text{Top}} = -0.6\ell(x_1/\ell)^3$ and $u_2^{\text{Top}} = 1.2\ell(|x_1|/\ell)^3$ for $\mathcal{S}_1$ and additionally, $u_1^{\text{Bottom}} = -0.6\ell(x_1/\ell)^3$ and $u_2^{\text{Bottom}} = -1.2\ell(x_1/\ell)^3$ to achieve the deformation profile $\mathcal{S}_2$. These displacements are applied incrementally, held to the prescribed constant values and then released incrementally during the appropriate steps.

- `Step-III`: This step gradually releases the constraints on $\mathbf{u}_\tau$ for all $\mathbf{X} \in \partial\mathcal{V}_{\text{MRE}}^{\text{Top}}$ and $\mathbf{X} \in \partial\mathcal{V}_{\text{MRE}}^{\text{Bottom}}$, while keeping $\mathbf{u}_\tau = \mathbf{0}$ at $\mathcal{V}_{\text{Air}}$ and the central vertical section of the beam. The beam comes back to its (almost) undeformed shape after this step.

- `Step-IV`: This is essentially the actuation step where the field $(b_2^{\texttt{actu}})_\tau$ is applied along $\widehat{\mathbf{E}}_2$. Hence, the Dirichlet boundary condition on φ_τ is set identical to (141), while that on $\mathbf{u}_\tau$ remain the same as at the end of `Step-III`.

The first key outcome from the aforementioned magneto-mechanical loading exercise is the variation of the remanent magnetization $\mathbf{m}^0$ along the beam's centerline at the end of `Step-III`. Specifically, the variation of the magnitude of $\mathbf{m}^0$ and its angle with $\widehat{\mathbf{E}}_1$ for all four combinations of pre-magnetization and c profiles, namely, $\mathcal{S}_i\mathcal{T}_j$ with $i, j \equiv 1, 2$ are shown in Fig. 25a and b, respectively. In agreement with the experimental observations (Ren et al., 2019; Alapan et al., 2020) , the magnitude of $\mathbf{m}^0$ remains the same in the beams $\mathcal{S}_1\mathcal{T}_1$ and $\mathcal{S}_2\mathcal{T}_1$, which have a spatially uniform c. The beams $\mathcal{S}_1\mathcal{T}_2$ and $\mathcal{S}_2\mathcal{T}_2$, on the other hand, exhibit a variation of $|\mathbf{m}^0|$ along the centerline. In fact this variation is proportional to the c variation in these beams. Thus, $|\mathbf{m}^0|$ in the beam is primarily controlled by c. In contrast, the orientation of $\mathbf{m}^0$ is dictated by its pre-magnetization profile $\mathcal{S}_1$ and $\mathcal{S}_2$ (see Fig. 25b). While the $\mathcal{S}_1$-type beams show opposite $\mathbf{m}^0$ directions along its two flanks, the direction of $\mathbf{m}^0$ in $\mathcal{S}_2$-type beams are identical in both the flanks, hence, showing a *bell curve* like variation in angle with the X_1 axis. Even though $|\mathbf{m}^0|$ in the beam is predictable in terms of c, the functional relationship of the θ^{m} profiles in Fig. 25b with the respective pre-deformed shapes in Fig. 24a and b are not straightforward and cannot be predicted beforehand prior solving the full field BVP.

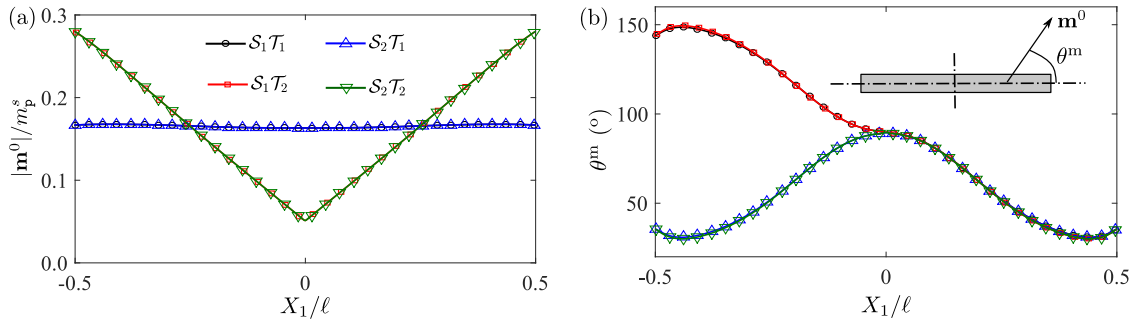

Figure 25: Variation of the remanent magnetization $\mathbf{m}^0$ (a) magnitudes and (b) directions along the length of the pre-magnetized h-MRE beams of type $\mathcal{S}_i\mathcal{T}_i$ $(i = 1, 2)$. (Taken from Mukherjee and Danas (2022)).

To obtain more insight on the complexity of the non-uniform remanent fields, we plot the spatial profiles of $\mathbf{b}^0$, $\mathbf{h}^0$ and $\mathbf{m}^0$ fields, both, in terms of magnitude and directions, in Fig. 26 for all four aforementioned types of beams. The first, and obvious feature observed is the higher magnitude of $\mathbf{b}^0$, $\mathbf{h}^0$ and $\mathbf{m}^0$ in the beams of type $\mathcal{T}_2$, which can directly be attributed to the higher c value in $\mathcal{T}_2$ near the beam flanks (cf. e.g., Figures 26a-c and g-i). Moreover, comparing Fig. 26b,e with h,k we observe that by linearly increasing c along the flanks, the concentration of $\mathbf{h}^0$ field near the center of the beam can be eliminated. Of course, the spatial gradient of c in the $\mathcal{T}_2$-type beams results in a stiffer gradient in the $|\mathbf{b}|^0$ along the beams's centerline (cf. Figures 26a,d and g,j).

In contrast, the directions of $\mathbf{b}^0$, $\mathbf{h}^0$ and $\mathbf{m}^0$ fields in the h-MRE along with the stray fields around the MRE domain depend strongly on their pre-magnetization profiles. Thus, we observe *qualitatively similar* stray $\mathbf{b}$ and $\mathbf{h}$ field distributions around the in all the $\mathcal{S}_1$ or $\mathcal{S}_2$-type beams,

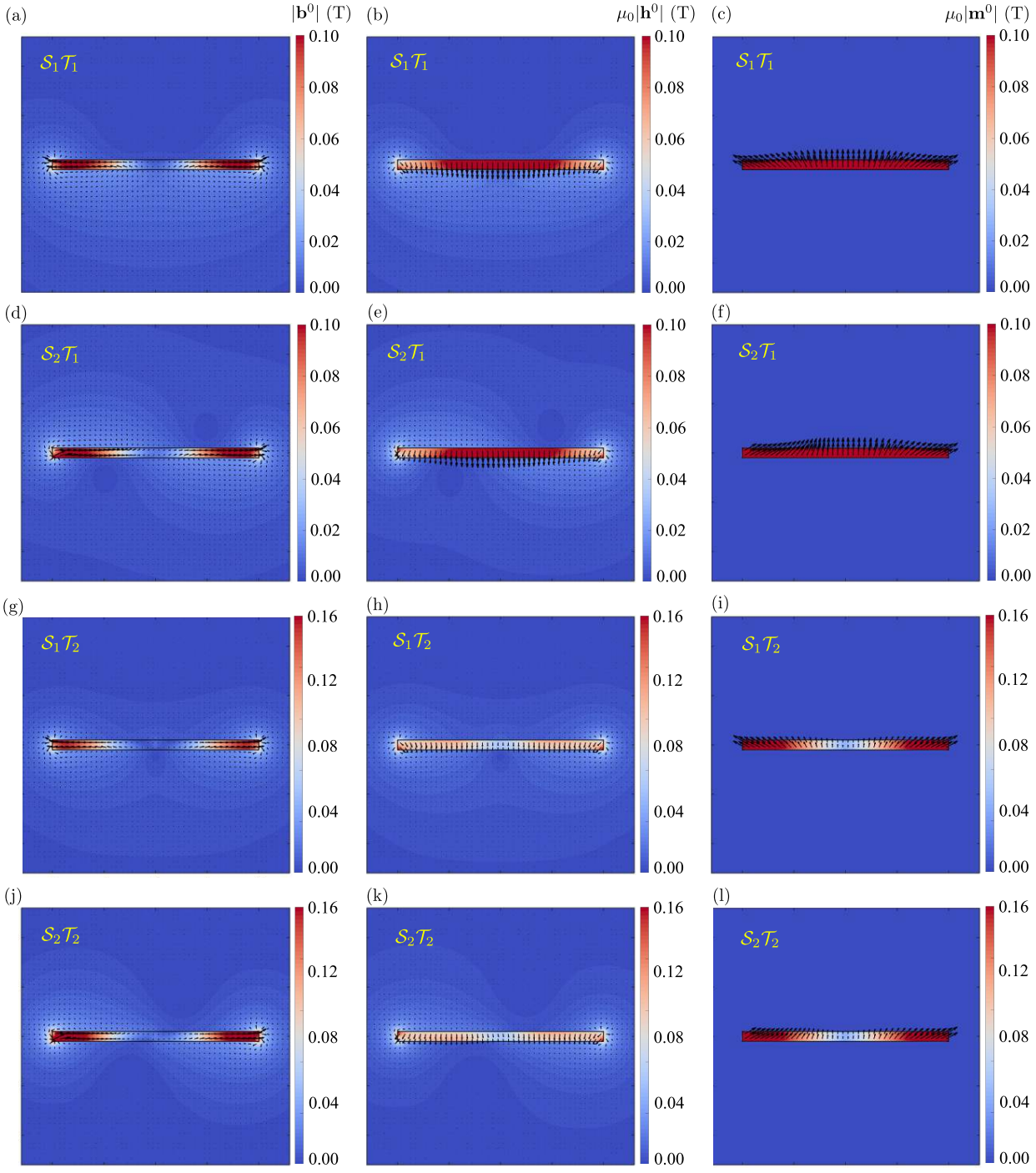

Figure 26: Magnitude contours along with the directions of the remanent $\mathbf{b}^0$, $\mathbf{h}^0$ and $\mathbf{m}^0$ fields *after* the pre-magnetization step (Step-3) for the h-MRE types (depending on the pre-deformation profile and particle distribution) (a-c) $\mathcal{S}_1\mathcal{T}_1$, (d-f) $\mathcal{S}_2\mathcal{T}_1$, (g-i) $\mathcal{S}_1\mathcal{T}_2$ and (j-l) $\mathcal{S}_2\mathcal{T}_2$. (Taken from Mukherjee and Danas (2022)).

irrespective of the c distributions in them. Specifically, we observe from Figures 26a and g that the beams with pre-magnetization profile $\mathcal{S}_1$ exhibit stronger self fields at the vicinity of their bottom

boundary as compared to the top. Such preferential self-field distributions are typically achieved by constructing *Halbach chains* (Halbach, 1980; Hilton and McMurry, 2012; Mansson, 2014), which consists of an array of permanent magnets arranged in a particular fashion in order to concentrate the resulting magnetic self field at one side of the chain. A similar feature is observed here for the $\mathcal{S}_1$-type non-uniformly pre-magnetized hMRE in Figs. 26a and g. Thus, a properly pre-magnetized, *monolithic* h-MRE can mimic the properties of classical, essentially heterogeneous, Halbach chain structures.

In turn, such a concentration of the magnetic self fields are not observed in the beams having the pre-magnetization profile as $\mathcal{S}_2$. Rather, the contours of higher magnetic self fields render an inverted "S"-type shapes in all the $\mathcal{S}_2$-type beams. Thus, proper profiling of the beam before the pre-magnetization may help engineering different self field distributions in the vicinity of a h-MRE. The implications of such self field distributions on the actuation response of the $\mathcal{S}_1$ and $\mathcal{S}_2$-type beams will be discussed next.

Remark 18. The $\mathbf{b}$, $\mathbf{h}$ and $\mathbf{m}$ field magnitude contours and directions in Fig. 26 reveal that the local remanent $\mathbf{b}$ and $\mathbf{m}$ fields in the h-MREs *are not* related by the relation $\mathbf{b} = \mu_0\mathbf{m}$. Hence, unlike the uniformly pre-magnetized h-MREs, it may reveal inaccurate to assume, in general, that the magnetic torque at a point in the h-MRE is simply given by $\mathbf{b}^{\mathtt{actu}} \times \mu_0\mathbf{m}$ during the actuation under remotely applied $\mathbf{b}^{\mathtt{actu}}$ field. Thus, even though the magnetic toque-based, reduced-order models for slender h-MRE beams exhibit sufficiently accurate deflection profiles (Wang et al., 2020; Yan et al., 2021a,b), their employment to the non-uniformly pre-magnetized h-MRE structures must be carried out with caution and certainly use the local non-uniform pre-magnetization profile. Moreover, the pre-magnetization directions along the beam length do not exhibit any straightforward correlation with its pre-deformation geometry. Hence, solving for the full-field BVP with a surrounding air becomes inevitable even for a reduced-order analysis in the later stage.

Finally, we show the transverse magnetic actuation performance of the four types of beams, namely, $\mathcal{S}_i\mathcal{T}_j$ with $i, j \equiv 1, 2$. First, we investigate the uniformly distributed c cases, i.e., the response of $\mathcal{T}_1$-type h-MREs in Fig. 27a-c. Specifically, Figures 27a and b show the deflected beam centerline under an actuation field $b_2^{\mathtt{actu}} = 20$ mT along $\widehat{\mathbf{E}}_2$ and $-\widehat{\mathbf{E}}_2$ directions. Identical deflection of both the beam flanks are observed for the beam $\mathcal{S}_1\mathcal{T}_1$. However, the deflection is substantially higher (~ 2.5 times) when the fields are applied along $-\widehat{\mathbf{E}}_2$. This observation can directly be attributed to the pre-magnetization direction in both the beam flanks, which, eventually leads to a higher deflection when deflecting in the opposite direction of $\mathbf{m}^0$. This preferential deflection phenomena can be termed as the *magneto-mechanical Halbach effect*. In fact, this preferential deflection property is harnessed effectively in locomotion of soft jellyfish-like swimming robot (Ren et al., 2019; Alapan et al., 2020).

Even though equal in their magnitudes, the two flanks of the $\mathcal{S}_2$-type pre-magnetized beams always deflect in the opposite direction. For example, the deflected centerline of the h-MRE beam under $b_2^{\mathtt{actu}} = 20$ mT along $\widehat{\mathbf{E}}_2$ and $-\widehat{\mathbf{E}}_2$ are shown in Fig. 27b. Of course, here the deflection magnitude remains identical to the $\mathcal{S}_1$-type h-MRE, but overall, leading to a rocking-type motion, where the two flanks deflect simultaneously in the opposite directions. In particular, the variation of the vertical displacement of top-right and bottom-left corners of the $\mathcal{S}_1\mathcal{T}_1$ and $\mathcal{S}_2\mathcal{T}_1$-type h-MRE beams under $b_2^{\mathtt{actu}}$ are shown in Fig. 27c. This figure clearly shows that the deflection magnitude under the same $|b_2^{\mathtt{actu}}|$ becomes ~ 2.5 times when the direction of its application is along $-\widehat{\mathbf{E}}_2$.

The $\mathcal{T}_2$-type beams exhibit a qualitatively similar deflection response under $b_2^{\mathtt{actu}}$ *vis-a-vis* the $\mathcal{T}_1$-type. The only and obvious difference between the former and the latter is that the $\mathcal{T}_2$-type

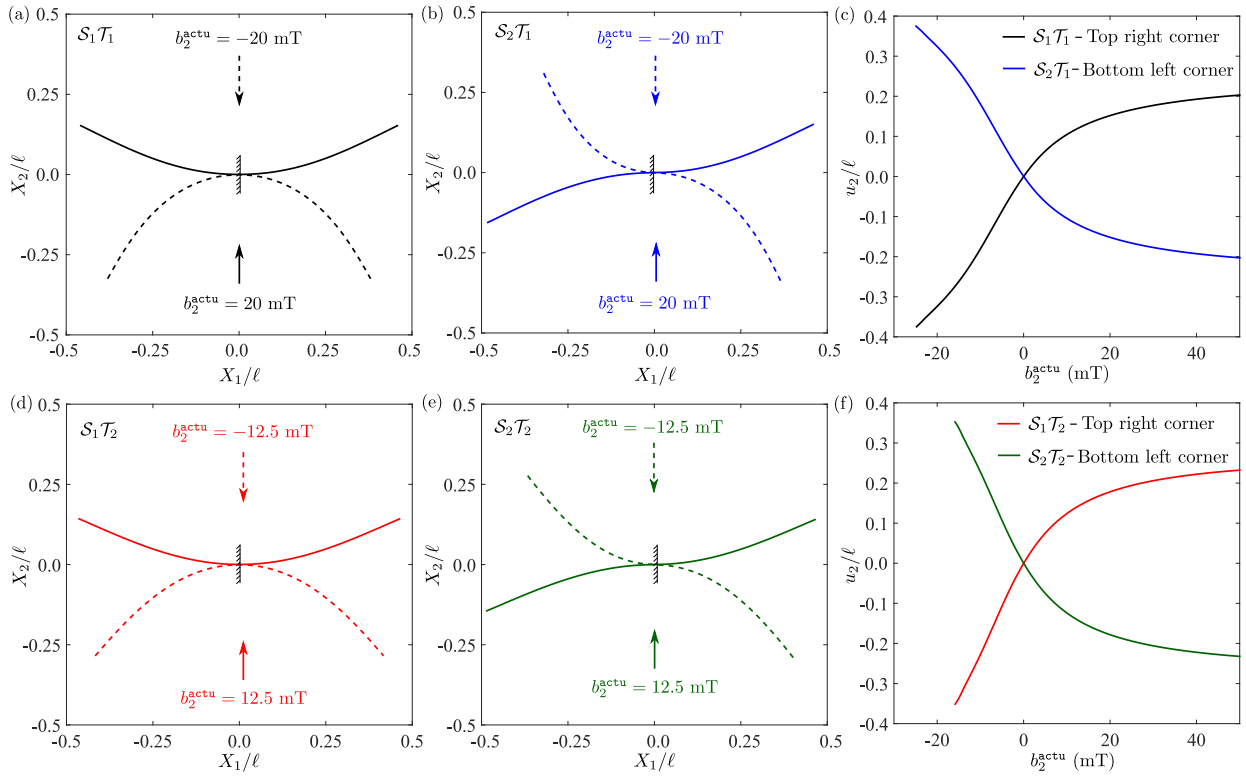

Figure 27: Deflected centerlines of the h-MREs type (a) $\mathcal{S}_1\mathcal{T}_1$ and (b) $\mathcal{S}_2\mathcal{T}_1$ under the actuation fields $b_2^{\mathtt{actu}} = 20$ and -20 mT along $\widehat{\mathbf{E}}_2$. (c) Variation of the top-right corner delfection of $\mathcal{S}_1\mathcal{T}_1$ and bottom left corner delfection $\mathcal{S}_2\mathcal{T}_1$ under $b_2^{\mathtt{actu}}$. Deflected centerlines of the h-MREs type (d) $\mathcal{S}_1\mathcal{T}_2$ and (e) $\mathcal{S}_2\mathcal{T}_2$ under the actuation fields $b_2^{\mathtt{actu}} = 12.5$ and -12.5 mT along $\widehat{\mathbf{E}}_2$. (f) Variation of the top-right corner delfection of $\mathcal{S}_1\mathcal{T}_2$ and bottom left corner delfection $\mathcal{S}_2\mathcal{T}_2$ under $b_2^{\mathtt{actu}}$. (Taken from Mukherjee and Danas (2022)).

beams deflect the same amount at a lower actuation field (~ 0.75 times). The deflected shapes of the $\mathcal{S}_1\mathcal{T}_2$ and $\mathcal{S}_2\mathcal{T}_2$-type beams are shown in Figures 27d and e, respectively, both, under $b_2^{\mathtt{actu}} = 12.5$ and -12.5. Finally, the deflection variation of the top-right and bottom-left corners of, respectively, $\mathcal{S}_1\mathcal{T}_2$ and $\mathcal{S}_2\mathcal{T}_2$-type beams under $b_2^{\mathtt{actu}}$ are shown in Fig. 27f.

In closing, we remark that except lowering of the actuation field magnitude, the functionally-graded h-MREs with a linearly increasing c towards the beam flanks do not exhibit any substantial difference with the actuation performance of its uniform c counterpart. In turn, fabricating the functionally-graded h-MREs adds on to the difficulty level and cost. The pre-magnetization profiling, in contrast, can dramatically change the actuation performance of the h-MRE beams. In this regard, the proposed model serves as an efficient tool to analyze the effect of different pre-magnetization profiles and directions even before the manufacturing of an actual sample is carried out.

Acknowledgments

The author would like to acknowledge support from the European Research Council (ERC) under the European Union's Horizon 2020 and Horizon Europe research and innovation program (grant agreement No. 636903 - MAGNETO and No. 101081821 - MagnetoSense). The com-

putational part of this work was also supported by the ANR, France under contract number ANR-10-EQPX-37. The Abaqus user defined element (UEL) developed for the numerical simulations using the proposed $\mathbf{F}-\mathbf{H}$ model along with a representative example are available at https://www.doi.org/10.5281/zenodo.4588578. The $\mathbf{F}-\mathbf{B}$ model UEL will be made available upon request. The author would like to thank his wonderful students D. Mukherjee, M. Rambausek, and colleagues L. Bodelot, V. Lefèvre, O. Lopez-Pamies and N. Triantafyllidis for their important contributions, feedback and collaboration over the last 15 years that allowed to develop this rather wide class of MRE models.

References

ABAQUS. *CAE/2017*. Simulia, RI, USA, 2017.

M. Abramowitz and I.A. Stegun. *Handbook of Mathematical Functions*. Dover, New York, 1972.

Yunus Alapan, Alp C. Karacakol, Seyda N. Guzelhan, Irem Isik, and Metin Sitti. Reprogrammable shape morphing of magnetic soft machines. *Science Advances*, 6(38):eabc6414, 2020. doi: 10.1126/sciadv.abc6414. URL https://doi.org/10.1126/sciadv.abc6414.

K. Anoukou, R. Brenner, F. Hong, M. Pellerin, and K. Danas. Random distribution of polydisperse ellipsoidal inclusions and homogenization estimates for porous elastic materials. *Comp. Struct.*, 210:87 – 101, 2018. ISSN 0045-7949. doi: https://doi.org/10.1016/j.compstruc.2018.08.006. URL http://www.sciencedirect.com/science/article/pii/S0045794918304565.

Anil K. Bastola and Mokarram Hossain. A review on magneto-mechanical characterizations of magnetorheological elastomers. *Composites Part B: Engineering*, 200:108348, 2020. ISSN 1359-8368. doi: https://doi.org/10.1016/j.compositesb.2020.108348. URL https://www.sciencedirect.com/science/article/pii/S1359836820333977.

K.C. Bennett, R.A. Regueiro, and R.I. Borja. Finite strain elastoplasticity considering the eshelby stress for materials undergoing plastic volume change. *International Journal of Plasticity*, 77:214–245, 2016. doi: 10.1016/j.ijplas.2015.10.007. URL https://doi.org/10.1016/j.ijplas.2015.10.007.

O. Biro and K. Preis. On the use of the magnetic vector potential in the finite-element analysis of three-dimensional eddy currents. *IEEE Transactions on Magnetics*, 25(4):3145–3159, 1989. doi: 10.1109/20.34388. URL https://doi.org/10.1109/20.34388.

L. Bodelot, J.-P. Voropaieff, and T. Pössinger. Experimental investigation of the coupled magneto-mechanical response in magnetorheological elastomers. *Experimental Mechanics*, 58(2):207–221, sep 2017. doi: 10.1007/s11340-017-0334-7. URL https://doi.org/10.1007/s11340-017-0334-7.

William Fuller Brown. *Magnetoelastic interactions*, volume 9. Springer, 1966.

R. Bustamante, A. Dorfmann, and R.W. Ogden. On variational formulations in nonlinear magnetoelastostatics. *Mathematics and Mechanics of Solids*, 13(8):725–745, 2008. doi: 10.1177/1081286507079832. URL https://doi.org/10.1177/1081286507079832.

Yi-Chao Chen and Lewis Wheeler. Derivatives of the stretch and rotation tensors. *Journal of Elasticity*, 32(3):175–182, 1993. doi: 10.1007/bf00131659. URL https://doi.org/10.1007/bf00131659.

K. Danas and N. Triantafyllidis. Instability of a magnetoelastic layer resting on a non-magnetic substrate. *Journal of the Mechanics and Physics of Solids*, 69:67–83, September 2014. doi: 10.1016/j.jmps.2014.04.003. URL https://doi.org/10.1016/j.jmps.2014.04.003.

K. Danas, S.V. Kankanala, and N. Triantafyllidis. Experiments and modeling of iron-particle-filled magnetorheological elastomers. *Journal of the Mechanics and Physics of Solids*, 60(1):120 – 138, 2012. ISSN 0022-5096. doi: 10.1016/j.jmps.2011.09.006. URL http://www.sciencedirect.com/science/article/pii/S0022509611001736.

Kostas Danas. Effective response of classical, auxetic and chiral magnetoelastic materials by use of a new variational principle. *Journal of the Mechanics and Physics of Solids*, 105:25–53, 2017. doi: 10.1016/j.jmps.2017.04.016. URL https://doi.org/10.1016/j.jmps.2017.04.016.

Peter A. Dashner. An objective kinematical formalism for the modeling of elastic-plastic materials subject to large deformation. *International Journal of Solids and Structures*, 30(19):2661–2672, 1993. doi: 10.1016/0020-7683(93)90104-f. URL https://doi.org/10.1016/0020-7683(93)90104-f.

Xiangxing Deng, Zhongwu Liu, Hongya Yu, Zhiyu Xiao, and Guoqing Zhang. Isotropic and anisotropic nanocrystalline NdFeB bulk magnets prepared by binder-free high-velocity compaction technique. *Journal of Magnetism and Magnetic Materials*, 390:26–30, 2015. doi: 10.1016/j.jmmm.2015.04.075. URL https://doi.org/10.1016/j.jmmm.2015.04.075.

Antonio DeSimone and Richard D. James. A constrained theory of magnetoelasticity. *Journal of the Mechanics and Physics of Solids*, 50(2):283–320, February 2002. doi: 10.1016/s0022-5096(01)00050-3. URL https://doi.org/10.1016/s0022-5096(01)00050-3.

G. Diguet. *Huge Magnetostriction of Magneto-Rheological Composite*. PhD thesis, Université de Grenoble, 2010.

G. Diguet, E. Beaugnon, and J.Y. Cavaillé. Shape effect in the magnetostriction of ferromagnetic composite. *J. Magn. Magn. Mater.*, 322(21):3337 – 3341, 2010. ISSN 0304-8853. doi: DOI:10.1016/j.jmmm.2010.06.020. URL http://www.sciencedirect.com/science/article/B6TJJ-5093N8V-2/2/d5878c0abd20adc88cdb94281950f912.

Gildas Diguet, Gaël Sebald, Masami Nakano, Mickaël Lallart, and Jean-Yves Cavaillé. Magnetic behavior of magneto-rheological foam under uniaxial compression strain. *Smart Materials and Structures*, 31(2):025018, dec 2021. doi: 10.1088/1361-665x/ac3fc8. URL https://doi.org/10.1088%2F1361-665x%2Fac3fc8.

A Dorfmann and RW Ogden. Nonlinear magnetoelastic deformations of elastomers. *Acta Mechanica*, 167(1-2):13–28, 2004. doi: 10.1007/s00707-003-0061-2. URL https://doi.org/10.1007/s00707-003-0061-2.

Charles Dorn, Laurence Bodelot, and Kostas Danas. Experiments and numerical implementation of a boundary value problem involving a magnetorheological elastomer layer subjected to a nonuniform magnetic field. *Journal of Applied Mechanics*, 88(7), 2021. doi: 10.1115/1.4050534. URL https://doi.org/10.1115/1.4050534.

A. C. Eringen. *Mechanics of Continua*. John Wiley and Sons, New York, 1967.

A. C. Eringen and G.A. Maugin. *Electrodynamics of Continua I: Foundations and Solid Media*. Springer-Verlag New York, 1990.

Evan Galipeau and Pedro Ponte Castañeda. A finite-strain constitutive model for magnetorheological elastomers: Magnetic torques and fiber rotations. *Journal of the Mechanics and Physics of Solids*, 61(4):1065–1090, 2013. doi: 10.1016/j.jmps.2012.11.007. URL https://doi.org/10.1016/j.jmps.2012.11.007.

Daniel Garcia-Gonzalez, Tigran Ter-Yesayants, Miguel Angel Moreno-Mateos, and Maria Luisa Lopez-Donaire. Hard-magnetic phenomena enable autonomous self-healing elastomers. *Composites Part B: Engineering*, 248: 110357, 2023. ISSN 1359-8368. doi: https://doi.org/10.1016/j.compositesb.2022.110357. URL https://www.sciencedirect.com/science/article/pii/S1359836822007302.

Philipp Gebhart and Thomas Wallmersperger. A constitutive macroscale model for compressible magneto-active polymers based on computational homogenization data: Part i — magnetic linear regime. *International Journal of Solids and Structures*, 236-237:111294, 2022a. ISSN 0020-7683. doi: https://doi.org/10.1016/j.ijsolstr.2021.111294. URL https://www.sciencedirect.com/science/article/pii/S0020768321003747.

Philipp Gebhart and Thomas Wallmersperger. A constitutive macroscale model for compressible magneto-active polymers based on computational homogenization data: Part ii — magnetic nonlinear regime. *International Journal of Solids and Structures*, 258:111984, 2022b. ISSN 0020-7683. doi: https://doi.org/10.1016/j.ijsolstr.2022.111984. URL https://www.sciencedirect.com/science/article/pii/S0020768322004371.

John M Ginder, Mark E Nichols, Larry D Elie, and Janice L Tardiff. Magnetorheological elastomers: properties and applications. In *Smart Structures and Materials 1999: Smart Materials Technologies*, volume 3675, pages 131–139. International Society for Optics and Photonics, 1999. doi: 10.1117/12.352787. URL https://doi.org/10.1117/12.352787.

Morton E Gurtin. *An introduction to continuum mechanics*. Academic press, 1982.

K. Halbach. Design of permanent multipole magnets with oriented rare earth cobalt material. *Nuclear Instruments and Methods*, 169(1):1–10, February 1980. doi: 10.1016/0029-554x(80)90094-4. URL https://doi.org/10.1016/0029-554x(80)90094-4.

Bernard Halphen and Quoc Son Nguyen. Sur les matériaux standard généralisés. *Journal de Mécanique*, 14:39–63, 1975.

Robin KS Hankin. Numerical evaluation of the gauss hypergeometric function with the hypergeo package. *The R Journal*, 7:81–88, 2015.

J.E. Hilton and S.M. McMurry. An adjustable linear halbach array. *Journal of Magnetism and Magnetic Materials*, 324(13):2051–2056, 2012. ISSN 0304-8853. doi: https://doi.org/10.1016/j.jmmm.2012.02.014. URL https://www.sciencedirect.com/science/article/pii/S030488531200100X.

Martín I. Idiart, Kostas Danas, and Pedro Ponte Castañeda. Second-order theory for nonlinear composites and application to isotropic constituents. *Comptes Rendus Mécanique*, 334(10):575–581, 2006a. ISSN 1631-0721. doi: https://doi.org/10.1016/j.crme.2006.06.006. URL https://www.sciencedirect.com/science/article/pii/S1631072106001070.

MI Idiart, Hervé Moulinec, P Ponte Castañeda, and Pierre Suquet. Macroscopic behavior and field fluctuations in viscoplastic composites: second-order estimates versus full-field simulations. *Journal of the Mechanics and Physics of Solids*, 54(5):1029–1063, 2006b. doi: https://doi.org/10.1016/j.jmps.2005.11.004. URL http://www.sciencedirect.com/science/article/pii/S0022509605002188.

R.D. James and D. Kinderlehrer. Theory of magnetostriction with applications to tbxdy1-xfe2. *Phil. Mag. B*, 68: 237–274, 1993. ISSN 0141-8637.

Mark R. Jolly, J. David Carlson, Beth C. Muñoz, and Todd A. Bullions. The magnetoviscoelastic response of elastomer composites consisting of ferrous particles embedded in a polymer matrix. *Journal of Intelligent Material Systems and Structures*, 7(6):613–622, 1996. doi: 10.1177/1045389x9600700601. URL https://doi.org/10.1177/1045389x9600700601.

Karl Alexander Kalina, Jörg Brummund, Philipp Metsch, Markus Kästner, D Yu Borin, Julia Martina Linke, and Stefan Odenbach. Modeling of magnetic hystereses in soft mres filled with ndfeb particles. *Smart Materials and Structures*, 26(10):105019, 2017. doi: 10.1088/1361-665x/aa7f81. URL https://doi.org/10.1088/1361-665x/aa7f81.

SV Kankanala and N Triantafyllidis. On finitely strained magnetorheological elastomers. *Journal of the Mechanics and Physics of Solids*, 52(12):2869–2908, 2004. doi: 10.1016/j.jmps.2004.04.007. URL https://doi.org/10.1016/j.jmps.2004.04.007.

M.-A. Keip and A. Sridhar. A variationally consistent phase-field approach for micro-magnetic domain evolution at finite deformations. *Journal of the Mechanics and Physics of Solids*, nov 2018. doi: 10.1016/j.jmps.2018.11.012. URL https://doi.org/10.1016/j.jmps.2018.11.012.

Marc-Andre Keip and Matthias Rambausek. A multiscale approach to the computational characterization of magnetorheological elastomers. *International Journal for Numerical Methods in Engineering*, 107(4):338–360, 2016. doi: 10.1002/nme.5178. URL https://doi.org/10.1002/nme.5178.

Yoonho Kim, Hyunwoo Yuk, Ruike Zhao, Shawn A. Chester, and Xuanhe Zhao. Printing ferromagnetic domains for untethered fast-transforming soft materials. *Nature*, 558(7709):274–279, 2018. doi: 10.1038/s41586-018-0185-0. URL https://doi.org/10.1038/s41586-018-0185-0.

Aditya Kumar and Oscar Lopez-Pamies. On the two-potential constitutive modeling of rubber viscoelastic materials. *Comptes Rendus Mécanique*, 344(2):102–112, feb 2016. doi: 10.1016/j.crme.2015.11.004. URL https://doi.org/10.1016/j.crme.2015.11.004.

Siddhant Kumar, Kostas Danas, and Dennis M. Kochmann. Enhanced local maximum-entropy approximation for stable meshfree simulations. *Computer Methods in Applied Mechanics and Engineering*, 344:858–886, February 2019. doi: 10.1016/j.cma.2018.10.030. URL https://doi.org/10.1016/j.cma.2018.10.030.

Victor Lefèvre, Kostas Danas, and Oscar Lopez-Pamies. A general result for the magnetoelastic response of isotropic suspensions of iron and ferrofluid particles in rubber, with applications to spherical and cylindrical specimens. *Journal of the Mechanics and Physics of Solids*, 107:343–364, oct 2017. doi: 10.1016/j.jmps.2017.06.017. URL https://doi.org/10.1016/j.jmps.2017.06.017.

Victor Lefèvre, Kostas Danas, and Oscar Lopez-Pamies. Two families of explicit models constructed from a homogenization solution for the magnetoelastic response of mres containing iron and ferrofluid particles. *International Journal of Non-Linear Mechanics*, 2019. ISSN 0020-7462. doi: https://doi.org/10.1016/j.ijnonlinmec.2019.103362. URL http://www.sciencedirect.com/science/article/pii/S0020746219306237.

Oscar Lopez-Pamies, Taha Goudarzi, and Kostas Danas. The nonlinear elastic response of suspensions of rigid inclusions in rubber: II—a simple explicit approximation for finite-concentration suspensions. *Journal of the Mechanics and Physics of Solids*, 61(1):19–37, 2013. doi: 10.1016/j.jmps.2012.08.013. URL https://doi.org/10.1016/j.jmps.2012.08.013.

S. Lucarini, M.A. Moreno-Mateos, K. Danas, and D. Garcia-Gonzalez. Insights into the viscohyperelastic response of soft magnetorheological elastomers: Competition of macrostructural versus microstructural players. *International Journal of Solids and Structures*, 256:111981, 2022a. ISSN 0020-7683. doi: https://doi.org/10.1016/j.ijsolstr.2022.111981. URL https://www.sciencedirect.com/science/article/pii/S0020768322004346.

Sergio Lucarini, Mokarram Hossain, and Daniel Garcia-Gonzalez. Recent advances in hard-magnetic soft composites: Synthesis, characterisation, computational modelling, and applications. *Composite Structures*, 279:114800, January 2022b. doi: 10.1016/j.compstruct.2021.114800. URL https://doi.org/10.1016/j.compstruct.2021.114800.

Daniel Mansson. On the suitability of using halbach arrays as potential energy storage media. *Progress In Electromagnetics Research B*, 58:151–166, 2014. doi: 10.2528/pierb14010704. URL https://doi.org/10.2528/pierb14010704.

Robert M. McMeeking and Chad M. Landis. Electrostatic forces and stored energy for deformable dielectric materials. *Journal of Applied Mechanics*, 72(4):581–590, 2005. doi: 10.1115/1.1940661. URL https://doi.org/10.1115/1.1940661.

Robert M. McMeeking, Chad M. Landis, and Salomon M.A. Jimenez. A principle of virtual work for combined electrostatic and mechanical loading of materials. *International Journal of Non-Linear Mechanics*, 42(6):831–838,

2007. doi: 10.1016/j.ijnonlinmec.2007.03.008. URL https://doi.org/10.1016/j.ijnonlinmec.2007.03.008.

J.-C. Michel, H. Moulinec, and P. Suquet. Effective properties of composite material with periodic microstructure: a computational approach. *Comput. Methods Appl. Mech. Engrg.*, 172:109–143, 1999.

C Miehe, D Rosato, and B Kiefer. Variational principles in dissipative electro-magneto-mechanics: A framework for the macro-modeling of functional materials. *International Journal for Numerical Methods in Engineering*, 86(10): 1225–1276, 2011. doi: 10.1002/nme.3127. URL https://doi.org/10.1002/nme.3127.

Miguel Angel Moreno-Mateos, Jorge Gonzalez-Rico, Emanuel Nunez-Sardinha, Clara Gomez-Cruz, Maria Luisa Lopez-Donaire, Sergio Lucarini, Angel Arias, Arrate Muñoz-Barrutia, Diego Velasco, and Daniel Garcia-Gonzalez. Magneto-mechanical system to reproduce and quantify complex strain patterns in biological materials. *Applied Materials Today*, 27:101437, 2022. ISSN 2352-9407. doi: https://doi.org/10.1016/j.apmt.2022.101437. URL https://www.sciencedirect.com/science/article/pii/S2352940722000762.

D. Mukherjee and K. Danas. An evolving switching surface model for ferromagnetic hysteresis. *Journal of Applied Physics*, 125(3):033902, jan 2019. doi: 10.1063/1.5051483. URL https://doi.org/10.1063/1.5051483.

Dipayan Mukherjee. Theoretical and numerical modeling of magnetorheological elastomers comprising magnetically soft and hard particles. *PhD Thesis*, 2020.

Dipayan Mukherjee and Kostas Danas. A unified dual modeling framework for soft and hard magnetorheological elastomers. *International Journal of Solids and Structures*, 257:111513, 2022. ISSN 0020-7683. doi: https://doi.org/10.1016/j.ijsolstr.2022.111513. URL https://www.sciencedirect.com/science/article/pii/S0020768322000725. Special Issue in the honour Dr Stelios Kyriakides.

Dipayan Mukherjee, Laurence Bodelot, and Kostas Danas. Microstructurally-guided explicit continuum models for isotropic magnetorheological elastomers with iron particles. *International Journal of Non-Linear Mechanics*, page 103380, 2020. doi: 10.1016/j.ijnonlinmec.2019.103380. URL https://doi.org/10.1016/j.ijnonlinmec.2019.103380.

Dipayan Mukherjee, Matthias Rambausek, and Kostas Danas. An explicit dissipative model for isotropic hard magnetorheological elastomers. *Journal of the Mechanics and Physics of Solids*, 151:104361, 2021. doi: 10.1016/j.jmps.2021.104361. URL https://doi.org/10.1016/j.jmps.2021.104361.

Raymond W Ogden. *Non-linear elastic deformations*. Courier Corporation, 1997.

Lars Onsager. Reciprocal relations in irreversible processes. i. *Physical Review*, 37(4):405–426, February 1931a. doi: 10.1103/physrev.37.405.

Lars Onsager. Reciprocal relations in irreversible processes. II. *Physical Review*, 38(12):2265–2279, December 1931b. doi: 10.1103/physrev.38.2265.

I. Papadioti, K. Danas, and N. Aravas. A methodology for the estimation of the effective yield function of isotropic composites. *International Journal of Solids and Structures*, 87:120–138, 2016. ISSN 0020-7683. doi: https://doi.org/10.1016/j.ijsolstr.2016.02.022. URL https://www.sciencedirect.com/science/article/pii/S0020768316000846.

Sungjune Park, Kunal Mondal, Robert M. Treadway, Vikash Kumar, Siyuan Ma, James D. Holbery, and Michael D. Dickey. Silicones for stretchable and durable soft devices: Beyond sylgard-184. *ACS Applied Materials & Interfaces*, 10(13):11261–11268, 2018. doi: 10.1021/acsami.7b18394. URL https://doi.org/10.1021/acsami.7b18394.

Warren F Perger, Atul Bhalla, and Mark Nardin. A numerical evaluator for the generalized hypergeometric series. *Computer physics communications*, 77(2):249–254, 1993.

P. Ponte Castañeda and E. Galipeau. Homogenization-based constitutive models for magnetorheological elastomers at finite strain. *Journal of the Mechanics and Physics of Solids*, 59(2):194–215, 2011. doi: 10.1016/j.jmps.2010.11.004. URL https://doi.org/10.1016/j.jmps.2010.11.004.

E. Psarra, L. Bodelot, and K. Danas. Wrinkling to crinkling transitions and curvature localization in a magnetoelastic film bonded to a non-magnetic substrate. *Journal of the Mechanics and Physics of Solids*, 133:103734, 2019. doi: 10.1016/j.jmps.2019.103734. URL https://doi.org/10.1016/j.jmps.2019.103734.

Erato Psarra, Laurence Bodelot, and Kostas Danas. Two-field surface pattern control via marginally stable magnetorheological elastomers. *Soft Matter*, 13(37):6576–6584, 2017. doi: 10.1039/c7sm00996h. URL https://doi.org/10.1039/c7sm00996h.

M. Rambausek and M.-A. Keip. Analytical estimation of non-local deformation-mediated magneto-electric coupling in soft composites. *Proceedings of the Royal Society A*, 474(2216):20170803, August 2018. ISSN 1364-5021, 1471-2946. doi: 10.1098/rspa.2017.0803. URL http://rspa.royalsocietypublishing.org/content/474/2216/20170803.

M. Rambausek, D. Mukherjee, and K. Danas. A computational framework for magnetically hard and soft viscoelastic magnetorheological elastomers. *Computer Methods in Applied Mechanics and Engineering*, 391:114500, 2022. ISSN 0045-7825. doi: https://doi.org/10.1016/j.cma.2021.114500. URL https://www.sciencedirect.com/science/article/pii/S0045782521007064.

Matthias Rambausek and Joachim Schöberl. Curing spurious magneto-mechanical coupling in soft non-magnetic materials. *International Journal for Numerical Methods in Engineering*, 124(10):2261–2291, 2023. doi: https://doi.org/10.1002/nme.7210. URL https://onlinelibrary.wiley.com/doi/abs/10.1002/nme.7210.

Ziyu Ren, Wenqi Hu, Xiaoguang Dong, and Metin Sitti. Multi-functional soft-bodied jellyfish-like swimming. *Nature Communications*, 10(1), July 2019. doi: 10.1038/s41467-019-10549-7. URL https://doi.org/10.1038/s41467-019-10549-7.

Daniele Rosato and Christian Miehe. Dissipative ferroelectricity at finite strains. variational principles, constitutive assumptions and algorithms. *International Journal of Engineering Science*, 74:162–189, 2014. doi: 10.1016/j.ijengsci.2013.08.007. URL https://doi.org/10.1016/j.ijengsci.2013.08.007.

Basant Lal Sharma and Prashant Saxena. Variational principles of nonlinear magnetoelastostatics and their correspondences. *Mathematics and Mechanics of Solids*, 26(10):1424–1454, dec 2020. doi: 10.1177/1081286520975808. URL https://doi.org/10.1177%2F1081286520975808.

Sebastian Stark, Artem S. Semenov, and Herbert Balke. On the boundary conditions for the vector potential formulation in electrostatics. *International Journal for Numerical Methods in Engineering*, 102(11):1704–1732, January 2015. doi: 10.1002/nme.4859. URL https://doi.org/10.1002/nme.4859.

Liu Wang, Yoonho Kim, Chuan Fei Guo, and Xuanhe Zhao. Hard-magnetic elastica. *Journal of the Mechanics and Physics of Solids*, 142:104045, 2020. doi: 10.1016/j.jmps.2020.104045. URL https://doi.org/10.1016/j.jmps.2020.104045.

Zhengjin Wang, Chunping Xiang, Xi Yao, Paul Le Floch, Julien Mendez, and Zhigang Suo. Stretchable materials of high toughness and low hysteresis. *Proceedings of the National Academy of Sciences*, 116(13):5967–5972, 2019. doi: 10.1073/pnas.1821420116. URL https://doi.org/10.1073/pnas.1821420116.

Dong Yan, Arefeh Abbasi, and Pedro M. Reis. A comprehensive framework for hard-magnetic beams: Reduced-order theory, 3d simulations, and experiments. *International Journal of Solids and Structures*, page 111319, 2021a. ISSN 0020-7683. doi: https://doi.org/10.1016/j.ijsolstr.2021.111319. URL https://www.sciencedirect.com/science/article/pii/S0020768321003978.

Dong Yan, Matteo Pezzulla, Lilian Cruveiller, Arefeh Abbasi, and Pedro M. Reis. Magneto-active elastic shells with tunable buckling strength. 12(1), may 2021b. doi: 10.1038/s41467-021-22776-y. URL https://doi.org/10.1038%2Fs41467-021-22776-y.

Dong Yan, Bastien F.G. Aymon, and Pedro M. Reis. A reduced-order, rotation-based model for thin hard-magnetic plates. *Journal of the Mechanics and Physics of Solids*, 170:105095, 2023. ISSN 0022-5096. doi: https://doi.org/10.1016/j.jmps.2022.105095. URL https://www.sciencedirect.com/science/article/pii/S0022509622002721.

Ruike Zhao, Yoonho Kim, Shawn A. Chester, Pradeep Sharma, and Xuanhe Zhao. Mechanics of hard-magnetic soft materials. *Journal of the Mechanics and Physics of Solids*, 124:244–263, 2019. doi: 10.1016/j.jmps.2018.10.008. URL https://doi.org/10.1016/j.jmps.2018.10.008.